

Dr.-Ing. Maik Rahlves

Hannoversches Zentrum für optische Technologien

Integrated Polymer Photonics

Fabrication, Design,
Characterization and Applications



Optical Technologies.

Integrated Polymer Photonics

- Fabrication, Design, Characterization and Applications -

sowie die darin aufgeführten wissenschaftlichen Arbeiten

[E 1-E 40, E 47, E 50]

Von der Fakultät für Maschinenbau
der Gottfried Wilhelm Leibniz Universität Hannover
zur Erlangung der Lehrbefugnis (venia legendi)

genehmigte Habilitationsschrift

von

Dr.-Ing. Dipl. Phys. Maik Rahlves
geboren am 17.04.1978 in Hannover

2016

Referenten: Prof. Dr.-Ing. Eduard Reithmeier
Institute of Measurement and Automatic Control
Leibniz Universität Hannover

Prof. Dr. Hans Zappe
Gisela and Erwin Sick Chair of Micro-optics
Department of Microsystems Engineering
Albert-Ludwigs-Universität Freiburg

Vorsitz: Prof. Dr.-Ing. Jörg Wallaschek
Institut für Dynamik und Schwingungen
Leibniz Universität Hannover

Acknowledgements

This thesis contains results of research work which was conducted at the Hannover Centre for Optical Technologies (HOT) at Leibniz Universität Hannover (LUH), Germany, as part of my post doctoral research and research group leader of the Applied Optics Group at HOT.

First of all, I would like to thank Prof. Dr.-Ing. Eduard Reithmeier for giving me the opportunity to be part of HOT, for his constant encouragement, and also for being the first referee of my thesis. Secondly, I am grateful to Prof. Dr. Hans Zappe from the Institute of Microsystems Engineering (IMTEK) of Albert-Ludwigs-Universität Freiburg, Germany, for being my second referee and Prof. Dr.-Ing. Jörg Wallaschek for heading the state doctorate committee.

I also acknowledge the support of our scientific director of HOT, Prof. Dr. Bernhard Roth, and the fruitful collaboration with my project partners Dr.-Ing. Jan Jocker and Jesus Diaz Diaz during my time as postdoctoral researcher and the Exist "SmartSens" team, Dr. Kort Bremer, Dr. Johanna Walter and Rima Rifai, for their support. In addition, I would like to thank all the PhD students at HOT who contributed to this work: Christain Kelb, Axel Günther, Maher Rezem, Sebastian Schlangen, Jenny Striezel, Arthur Varkentin, Monali Suar and of course all other colleagues at HOT. Finally, I would like to thank my family and Rahel for their constant encouragement and patience.

Maik Rahlves

August, 8th 2017

Abstract

Polymer-based integrated photonics is arising as a cost-efficient alternative to silicon photonics in applications as broad as optical sensing, telecommunication and backplanes for optical computing. Polymers offer various advantages compared to their semiconductor counterparts such as low material and fabrication costs as well as the potential to be manufactured by high-throughput reel-to-reel methods. However, the development of polymer-based photonic elements and especially planar lightwave circuits (PLCs) with suitable mass-market compatible manufacturing techniques is still in progress.

In this work, we focus on the design and fabrication of fully-polymer based integrated photonic components through hot embossing, reactive lamination and maskless lithography which are easily convertible to reel-to-reel processes. An emphasis is placed on methods that are capable of creating fully-polymer based PLCs in thin polymer substrate materials with a thickness down to 50 μm . Furthermore, optical characterization techniques were investigated and improved through numerical simulations and experimental work which allow 2-D and 3-D topography and volumetric as well as refractive index and phase measurements. In addition, we present coupling structures based on micromirrors and diffractive gratings integrated in PLCs as well as corresponding fabrication methods which are also compatible to reel-to-reel process chains. Especially when designing interconnects, a remaining challenge is an efficient compensation of misalignment errors between optical components due to the manufacturing process. To address this challenge, we developed an approach based on self-written waveguides (SWW) to establish self-aligning interconnects. These methods are utilized to create transmission lines containing light sources, coupling structures, waveguides and detectors in a single polymer foil. In addition, we present two sensor concepts to determine displacement, strain and temperature which are compatible to polymer-based PLCs and fabricated using the investigated techniques. In future applications, the investigated photonic elements and corresponding manufacturing technologies will enable low-cost and high-throughput fabrication of photonic integrated circuits (PICs), PLCs and in addition optical sensors. Thus, the results will enable mass market compatible devices including optical interlinks, microprocessors and disposable sensors for biomedical applications among others.

Abstrakt

Integrierte Polymerphotonik entwickelt sich zunehmend zu einer kostengünstigen Alternative zur siliziumbasierten Photonik. Anwendungsfelder für Polymerphotonik sind weitgefächert und erstrecken sich von der optischen Sensorik über die Telekommunikation bis hin zu Backplanes für optische Computer. Polymerbasierte Photonik bietet gegenüber der halbleiterbasierten Photonik insbesondere Vorteile wie beispielsweise niedrige Material- und Herstellungskosten sowie Herstellbarkeit durch durchsatzstarke Rolle-zu-Rolle Prozesse. Die Erforschung und Entwicklung von polymerer Photonik und insbesondere wellenleiterbasierter Planar Lightwave Circuits (PLCs) sowie entsprechender Herstellungsverfahren noch im Fokus der aktuellen Forschung.

Wesentliches Ziel dieser Arbeit war daher die Erforschung von polymerbasierten, integrierten photonischen Komponenten sowie relevante Herstellungsmethoden, die insbesondere Heißprägen, Reaktivlaminieren und maskenloser Lithographie umfassen. Mit Hilfe dieser Technologien konnten PLCs auf flexiblen Polymersubstraten mit Schichtdicken zwischen 50 μm bis 500 μm realisiert werden. Zur Charakterisierung entsprechender photonischer Komponenten wurden auf Grundlage optischer Simulationen Methoden erforscht und weiterentwickelt, die sowohl eine topographische und volumetrische Charakterisierung als auch Brechungsindex- und Phasenmessungen erlauben. Die Integration von Lichtquellen und Detektoren in flexible, polymerbasierte PLCs erfolgte durch die Erforschung und Herstellung von reflektiv und diffraktiv arbeitenden Koppelstrukturen. Hierbei lag der Fokus auf Herstellungsmethoden, die direkt auf durchsatzstarke Rolle-zu-Rolle Verfahren übertragbar sind. Um Positioniertoleranzen zwischen einzelnen optischen Elementen bei deren optischen Kopplung automatisch kompensieren zu können, wurde im Rahmen dieser Arbeit ein Verfahren entwickelt, das auf selbstschreibenden Wellenleitern (SWW, engl. für Self-Written Waveguides) aufsetzt. Sowohl Herstellungs- als auch Koppelkonzepte sind eingesetzt worden, um vollständige Übertragungstrecken zu realisieren, die zum einen auf organischen und zum anderen auf halbleiterbasierten Lichtquellen und Detektoren aufbauen. Auf Grundlage dieser Arbeiten wurde ein neuartiges Konzept eines intensitätsmodulierten Abstandssensors erforscht und realisiert. Zusätzlich konnten Bragg Sensoren in heißgeprägten Wellenleitern erzeugt und als Temperatursensoren verwendet werden.

Content

1	Introduction.....	1
2	Integrated Photonics	3
3	Contribution and Layout of this Work.....	7
4	Fundamentals of Integrated Optics and Photonics.....	9
4.1	Waveguide Fundamentals.....	9
4.1.1	Light Propagation in Waveguides.....	9
4.1.2	Basic Waveguide Geometries and Structures	13
4.1.3	Light Coupling	16
4.2	Fabrication methods.....	19
4.2.1	Fabrication of Film Structures	19
4.2.2	2.5-D and 3-D Micro-Structuring and Replication	21
4.3	Materials.....	25
4.3.1	Inorganic Materials.....	25
4.3.2	Organic Materials	26
4.4	Optical Design Methods	30
4.4.1	Ray tracing	30
4.4.2	Rigorous Coupled-Wave Analysis	31
4.4.3	Beam Propagation Method	33
4.4.4	Other Design Methods	34
5	Overview of Own Research Results.....	36
5.1	Characterization of Integrated Optical Systems.....	36
5.1.1	Overview.....	36
5.1.2	2-D Topography Measurements.....	37
5.1.3	Volumetric 3-D Measurement.....	39
5.1.4	Measurement of Scattering Parameters	42
5.1.5	Refractive Index Measurements	44
5.1.6	Phase Measurements	46
5.1.7	Optical Loss Measurements	48
5.1.8	Opto-mechanical Properties.....	49
5.2	Fabrication of Integrated Polymer Optical Systems.....	51
5.2.1	Overview.....	51
5.2.2	Hot embossing.....	52
5.2.3	Reaction lamination.....	60
5.2.4	Maskless lithography	62
5.3	Optical Design.....	71
5.3.1	Overview.....	71
5.3.2	Diffraction Optical Elements.....	71

5.3.3	Integrated Photonics	74
5.4	Integration of Photonic Components	76
5.4.1	Overview	76
5.4.2	Beam splitters	77
5.4.3	Optical Couplers	79
5.4.4	Optical Transfer Line.....	84
5.5	Integrated Polymer Sensor Devices.....	86
5.5.1	Overview.....	86
5.5.2	Deformation/Strain Sensing	87
5.5.3	Integrated Fiber Bragg Grating Sensors	89
6	Summary.....	92
7	Zusammenfassung.....	94
8	References	97
9	List of Own Publications	103

Abbreviations and Symbols

Abbreviations

μ CP	Micro-contact printing
2-D	Two-dimensional
3-D	Three-dimensional
ASP	Angular spectrum propagation
AWG	Arrayed waveguide grating
BPM	Beam propagation method
COC	Cyclic olefin copolymer
CVD	Chemical vapor deposition
DEMUX	De-multiplexer
DMD	Digital mirror device
DOE	Diffractive optical element
DRIE	Deep reactive ion etching
EME	Eigenmode expansion
FDTD	Finite difference time domain
FEM	Finite element method
FFT	Fast Fourier transform
HEL	Hot embossing lithography
IAD	Ion assisted deposition
IFTA	Iterative Fourier transform algorithms
IR	Infrared part of the light spectrum
ITO	Indium tin oxide
IVD	Ion vapor deposition
LCD	Liquid crystal display
LD	Laser Diode
LED	Light emitting diode
MC	Monte-Carlo
MMI	Multimode interference
MUX	Multiplexer
MZI	Mach-Zehnder interferometer
NA	Numerical aperture
NIL	Nanoimprint lithography
NIR	Near infrared
OCT	Optical coherence tomography
OLED	Organic light emitting diode
OPD	Optical path length difference
OPD	Organic photodetector
OPL	Optical path length
PC	Polycarbonate
PD	Photo detector
PDMS	Polydimethylsiloxane
PIC	Photonic integrated circuit
PLC	Planar lightwave circuit
PMMA	Poly(methyl methacrylate)
PS	Polystyrene
PVD	Physical vapor deposition
R2R	Reel-to-reel
RCWA	Rigorous coupled-wave analysis

RIM	Reactive micro injection molding
rpm	Rounds per minute
SLM	Spatial light modulator
SMD	Surface mounted device
SOI	Silicon-on-insulator
SON	Silicon-on-nitride
SOS	Silicon-on-sapphire
SQP	Sequential quadratic programming
SWW	Self-written waveguide
TE	Transversal electric
TEM	Transversal electromagnetic
TIR	Total internal reflection
TM	Transversal magnetic
UV	Ultraviolet part of the light spectrum
VCSEL	Vertical-cavity surface emitting diode
VIS	Visible part of the light spectrum
VLSI	Very large scale integration

Symbols

Greek Symbols

α	Attenuation coefficient
α	Thermo-optical coefficient
β_m	Propagation constant of the m -th mode
β_ν	Propagation constant of the ν -th mode
δ	Path length offset of a ray
$\Delta\varphi$	Phase difference
η	Coupling efficiency
γ_m	Extinction coefficient
ϑ_d	Demolding temperature
ϑ_e	Embossing temperature
θ	Polar scattering angle
θ_c	Critical angle
θ_i	Angle of incidence
θ_m	Propagation angle of the m -th mode
θ_γ	Opening angle of Y-shaped beam splitter
μ_0	Vacuum permeability
μ_s	Scattering parameter
ϵ_0	Vacuum permittivity
κ	Coupling constant
Λ	Grating period
λ	Wavelength
λ_0	Vacuum wavelength
λ_B	Bragg wavelength
$\Delta\lambda_B$	Bragg wavelength shift
ν	Number of diffraction order
ω	Frequency

Roman Symbols

a_m	Eigenvalue to eigenfunction u_m , mode amplitude
C_{mn}	Zernike coefficient of m -th and n -th order

d	Waveguide diameter, layer height (RCWA)
d_{max}	Maximal penetration depth of photons
d_s	Waveguide distance
\mathbf{E}	Electrical field vector
\mathbf{E}_0	Initial electrical field vector
F	Focus value
F_d	Demolding force
F_e	Embossing force
F_i	Imprint force
f	Focal distance
Δf	Misalignment from focal position
g	Anisotropic factor
\mathbf{H}	Magnetic field vector
\mathbf{H}_0	Initial magnetic field vector
I_{in}	Intensity launched into device
I_{out}	Intensity coupled out of device
k	Wave number
\mathbf{k}	Wave vector with components (k_x, k_y, k_z)
K	Absolute value of grating vector
\mathbf{K}	Grating vector
l_O	Object arm length
l_R	Reference arm length
l_0	Initial elongation
Δl	Elongation change
L_{bend}	Bend losses
L_c	Coherence layer
L_{coup}	Coupling losses
L_{prop}	Propagation losses
L_{total}	Total losses
M	Maximum number of propagating modes
N	Maximum number of diffraction orders
n	Refractive index
Δn	Refractive index difference
n_{eff}	Effective refractive index
p	Scattering probability density function
q	Number of diffraction order
R	Bent radius
R_{GD}	Molar refraction according to Gladstone and Dale
S	Wavefront
\hat{S}	Vector normal on wavefront S
T_g	Glass transition temperature
u_m	Electrical field eigenfunction of m -th mode
v_d	Demolding velocity
v_e	Embossing velocity
Δz	Shift in z -direction
<hr/>	
Mathematical Symbols	
$\lceil \rceil$	Ceiling function
∇	Nabla operator

1 Introduction

Polymer based photonics has emerged as one of the key technologies of the 21st Century and is considered fundamental technology to tackle major challenges in the communication, energy and also medical to name just a few. Telecommunication is a classic example of an area in which photonic components are being used. These components also typically include silica fibers as they provide high data rates for long distance communication. While polymers will probably not be suitable substitutes for long range data transfer due to significantly larger absorption compared to silica, strong advantages of polymers are their capability for miniaturization at extraordinary low fabrication costs. As a consequence, polymers lend themselves to the fabrication of micro-optics but they even pave the way into fully polymer-based devices with optical functionalities similar to those of electronic components. Today, polymer optical devices are not only state-of-the-art in short broadband communication networks such as the ones used in computer networks but also in organic display technology utilized in mass-market applications such as display fabrication. Organic displays are commonly based on organic light emitting diodes (OLEDs) and fabricated on thin substrates taking advantage of high-throughput manufacturing techniques.

However, the application spectrum of integrated photonics consisting of both organic and inorganic materials is broader than pure display technology or optical networks alone. The transition from pure passive data transferring optical elements to complex active components such as optical switches, modulators and filters and also optical waveguide-based sensors has already been taken place. A basic prerequisite for the fabrication of highly efficient optical networks as well as sensor systems is the integration of light sources and detectors as well as interlinks between single optical waveguides and optical elements into the integrated photonic device. Such optical elements are backbone components of more complex systems such as photonic integrated circuits (PICs) which are about to replace their electronic counterparts in specific applications. Naturally, as integrated circuits (ICs) in electronics represented the early stage of microprocessors, PICs are also the initial step towards optical computing enabling bit-rates which have been limited by classical electronics.

Up until now, research was most often focused on the fabrication of inorganic PICs, as standard manufacturing methods are at hand which have predominantly been utilized in electronics fabrication. Hence, as in electronics, mostly planar photonics boards have been developed so far and silica-based planar lightwave circuits (PLCs) have been demonstrated which exhibit extraordinary high optical performance. However, silica or silicon-on-insulator (SOI) devices are subject to few major disadvantages where, on the other side, polymers offer great advantages: First, fabrication methods are potentially faster and more cost efficient using polymers. Second, the required power consumption in active silica components exceeds that of polymer based components. Third, polymer-based devices are mostly biocompatible and can even be used as disposable sensor devices due to low fabrication cost and, thus, their mass-market potential. As logical consequence it is highly desirable to replace silica-based PLCs with fully polymer-based PLCs

in certain applications and develop suitable manufacturing technologies which enable fabrication and integration not only of polymer waveguides but also light sources, detectors and active optical components.

In this work, we particularly focus on these challenges and investigate low-cost and potentially reel-to-reel capable high-throughput fabrication methods based on thermal imprint (hot embossing) for polymer based integrated photonic components including waveguides, beam splitters as well as coupling structures to be connected with integrated light sources and detectors. We created photonic components in thin polymer foils with thicknesses ranging from 50 μm to 500 μm . Also, novel waveguide based sensor concepts are presented including suitable fabrication techniques primarily based on hot embossing, reactive lamination and UV-laser induced refractive index changes. We exemplarily focus on detection of measurands such as temperature, displacement and strain. In addition, recent results on optical characterization and modeling of waveguide based components and measurement methods are summarized. Most of the presented work was carried out in the framework of the collaborative research center/transregio 123 PlanOS - "Planar Optronics Systems", which is a collaboration between the Leibniz University Hannover and the Albert-Ludwigs-University Freiburg. The research consortium especially aims at the development of novel polymer materials, fabrication methods and sensor concepts to be created in thin fully polymer-based sensors foils.

The results of our work will enable mass fabrication of polymer-based PICs and PLCs but also polymer optical sensors in applications as diverse as optical computing, biomedical sensing and holographic display technology. For example, waveguide based sensors are within reach which are capable to monitor chronic illnesses in point-of-care testing and significantly enhance patient treatment.

Research results presented in this work are based on following projects:

- Collaborative Research Center/Transregio 123 PlanOS - "Planar Optronics Systems" funded by the German Research Foundation (DFG)
- VIP-Project MeDiOO "Melanomdickenbestimmung mittels optischer Kohärenztomographie and Optoakustik" funded German Federal Ministry of Education and Research (BMBF), grant number 03V0826
- EFB-Project HOLO "Method to Emboss Holograms in Sheet Metal Parts with non-planar Surfaces" funded by German Federation of Industrial Research Associations (AiF) (EFB ZN 500)
- „Einsatz der OCT-Bildgebung zur medizinischen Nahfeldnavigation“ funded by DFG under grant RE 1488/15-2

2 Integrated Photonics

Development progress in integrated photonics is often compared to that of electronics. Starting with simple conducting metal wires to transport electrical signals, semiconductor materials allowed the invention of single transistors which are still fundamental elements of recent high-performance computer processors. Future trends in integrated photonics are expected to evolve in a very similar way in analogy to the development of electronics allowing a drastic increase in transmission rates at integration densities which are further increasing. The ultimate goal in photonics is, of course, to achieve very large-integration (VLSI) by utilizing wafer based manufacturing techniques [1].

Nowadays, various materials have been utilized for single photonic elements and especially photonic integrated circuits (PICs). However, silicon is the dominant material in semiconductor industry but it is also suitable as basic material for PIC fabrication as it provides very low transmission losses at telecommunication wavelengths especially around $1.3\ \mu\text{m}$ and $1.55\ \mu\text{m}$. Thus, computer chip manufacturers naturally focus on the development of PICs using silicon which has led to the photonics branch, often denoted as silicon photonics, facing tremendous popularity during the last decade. Industrial mass market products have emerged from large industrial and also academic research attempts in this field and significant progress has been achieved especially in the optical interlink and short range telecommunication sector. Fabrication of photonic components has drastically benefited from complementary-metal-oxide semiconductor (CMOS) developments especially in combination with silicon-on-insulator (SOI) technology [2]. The latter technology is based on a thin crystalline silicon layer on an insulator which is commonly made from silica but also sapphire and nitride were used as substrate materials. These technologies are referred to as silicon-on-sapphire (SOS) or silicon-on-nitride (SON) technologies, respectively [2]. Using SOI processes, various integrated photonic elements have been created such as ring resonator based switches [3] or waveguide based concepts such as photonic crystals [4].

However, silicon exhibits a strong non-linear behavior, which enables the fabrication of optical switches on the one hand but limits data rate transfer on the other [5]. Furthermore, active optical components such as light sources or detectors require different material properties such as direct semiconductors. Therefore, III-V semiconductors came into play and developments also focused on hybrid III-V silicon compound technologies. The combination of both material classes led to promising results in PIC fabrication for passive optical components [6]. Active components were achieved such as multiplexer (MUX) and de-multiplexer (DEMUX) based on Mach-Zehnder interferometers (MZIs) as switches [7]. These recent developments have even enabled simple single-chip microprocessors which utilize light for communication and switching [8]. A feature of semiconductor fabrication processes is that they are limited to planar substrates. If based on waveguides, these are also referred to as planar lightwave circuits (PLCs). Note that a short summary of dominating semiconductor processing methods is given in Section 4.2.

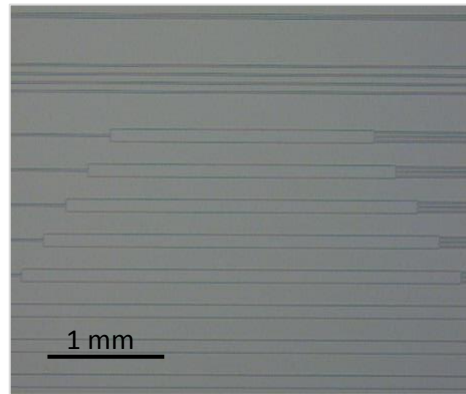


Figure 2.1: Multimode interference (MMI) coupler fabricated in poly(methyl meth)acrylate (HOT 2017, unpublished)

Integrated photonic systems and elements described so far in this Section including their fabrication processes were entirely based on inorganic materials. In recent years, a shift towards organic materials in research and development as well as in industrial applications is observed. Polymers are inexpensive, easier to process and also provide excellent optical properties in terms of transmission losses compared to their semiconductor counterparts [9], [10]. Therefore, research developments were also focused on polymer-based PICs and PLCs.

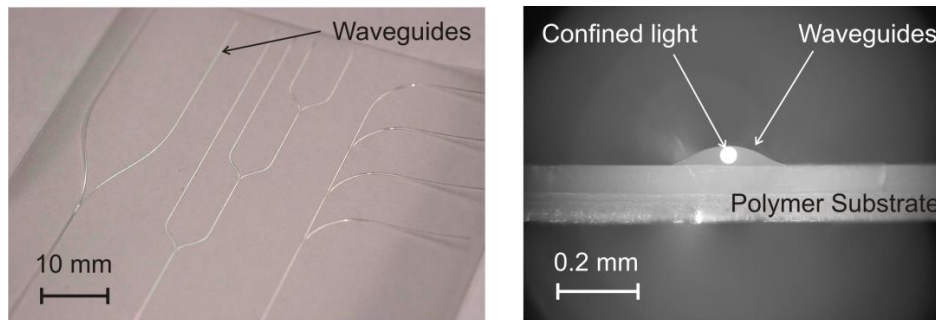


Figure 2.2: Printed multimode waveguides on a poly(methyl methacrylate) (PMMA) substrate: photograph of printed waveguide structures (left); microscope image of a cross section through a waveguide showing light confinement (courtesy of Tim Wolfer, Leibniz Universität Hannover, Germany).

In polymer photonics, examples of fundamental optical elements and structures are, as in silicon photonics, waveguides, beam splitters and also interconnects which were created using various fabrication methods. These fabrication processes include laser direct writing, hot embossing, nanoimprint and printing technologies among others [2], [11], [12]. Figure 2.1 shows multimode interference coupler hot embossed into poly(methyl meth)acrylate. Examples of printed multimode waveguides for PLCs are shown in Figure 2.2. Also, arrayed-waveguide-grating spectrometers and interferometers which are especially designed for PLCs and fully polymer-based were reported [33], [70] (see Figure 2.3 and Figure 2.4, respectively).

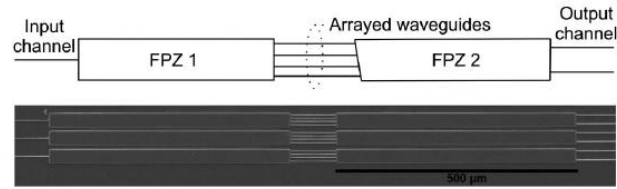


Figure 2.3: Sketch (top) and microscope image (bottom) of an arrayed-waveguide-grating (AWG) spectrometer made from Ormocer™ polymer (source: [13]).

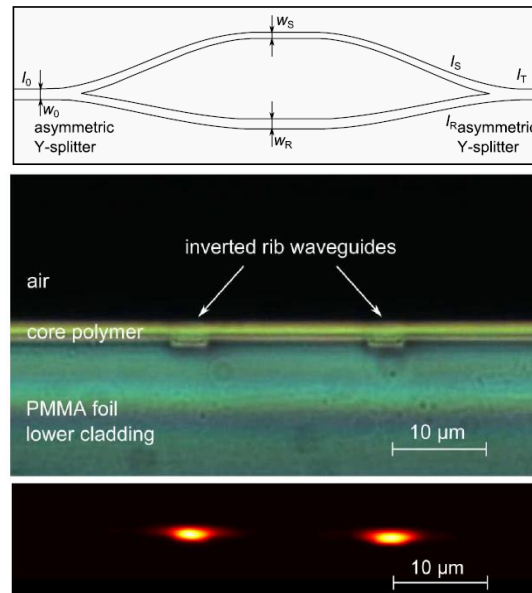


Figure 2.4: Asymmetric Mach-Zehnder interferometer fabricated through hot embossing and spin coating on a thin PMMA substrate using epoxy-based core materials: optical design (top); cross section through interferometer arms (middle); light guiding through fabricated waveguides (source: [14]).

Using polymers, however, refractive index contrasts between single components can never be as large as in silicon photonics and, as a consequence, integration densities will probably not be as small. Also, optical and mechanical properties of polymers suffer much greater from a dependency on environmental influences such as temperature or humidity compared to semiconductors. On the other side, they are promising candidates for large scale fabrication utilizing especially reel-to-reel (R2R) processes and offer more layout flexibility. An example of a polymer-based PICs fabricated by reel-to-reel nanoimprint is shown in Figure 2.5.

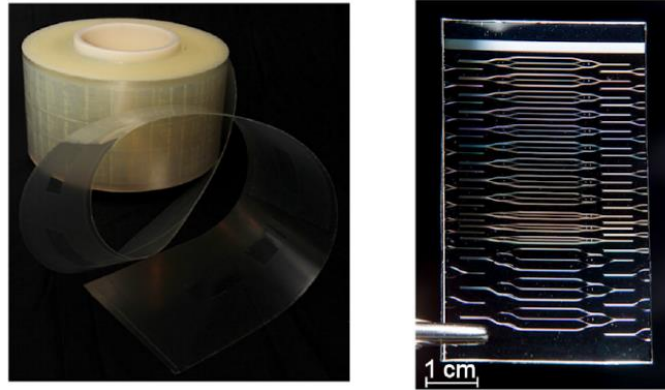


Figure 2.5: Reel-to-reel fabricated polymer sensor chip using nanoimprint: roll of sensor PICs (left) and separated sensor chip (right) (source: [15]).

Hence, future trends in polymer-based photonics will focus especially on R2R processes and suitable polymer materials to fabricate PICs and PLCs at a low-cost level. Up until now, one of the remaining challenges in polymer photonics is the integration of different active and passive photonic components into a single PIC or PLC aiming at high power transmission and simple fabrication methods. Once these issues are resolved, polymer-based PICs and PLCs are capable of replacing silicon-based one in various scenarios such as optical sensing in applications ranging from force, temperature and displacement measurement to biomedical single-use point-of-care sensors. But also simple fully-optical and polymer backplanes as support for optical microprocessors are within reach.

3 Contribution and Layout of this Work

Large scale and high throughput fabrication of polymer-based PICs and PLCs are basic requirements for future developments and down scaling of feature sizes in integrated polymer photonics. While past work has focused on the design, fabrication and optimization of single polymer photonic components, a demand for large scale fabrication through reel-to-reel processes of such devices in recent developments exists. Generating polymer-based PICs and PLCs, however, does not only require fabrication of waveguides but also concepts for interconnects and coupling structures to integrate various optical elements in polymer substrates with sufficient accuracy. For industrial manufacturing and later applications of devices, prime demands on these concepts are not only high coupling efficiencies but they are also required to be realized in reel-to-reel processes. In addition, most work which has been carried out so far has focused on the development of polymer components which are operated in the near infrared (NIR) range of the light spectrum as it includes classical telecommunication wavelengths. However, for some applications such as biomedical sensing, operation wavelengths in the visible (VIS) spectral range are desirable.

To continue recent activities in integrated polymer photonics, in this work we focus on the design, development and fabrication of multimode waveguides, beam splitters, novel coupling structures, and interconnects through manufacturing technologies which are directly transferable to reel-to-reel manufacturing facilities. Processes which were developed and advanced in this work are based on hot embossing, reactive lamination and maskless lithography, where the latter method lends itself to fabrication of hot embossing stamps and direct fabrication of small series also including diffractive optical elements (DOE). In this work, we explicitly focus on wavelengths in the range of 400 nm to 850 nm and targeted waveguide losses well below 1 dB/cm in the VIS. In addition, we introduce two waveguide-based sensors to measure displacement, strain and temperature which were fabricated through the aforementioned process chains. Also, we describe our recent advancements in the optical characterization of integrated photonics based on confocal microscopy and optical coherence tomography (OCT).

To give a brief overview of fundamentals in integrated photonics, a short introduction of mathematical concepts for a theoretical description of light propagation in waveguides is given in Section 4.1. In Sections 4.2 and 4.3, we introduce most commonly used techniques and methods for fabrication of both inorganic and inorganic waveguides and also PICs and PLCs as well as typically used materials. Section 4 is concluded by a description of mathematical concepts of optical design methods which were utilized in this work. The main research results are summarized in Section 5, which is structured as follows:

- **Subsection 5.1** describes work concerning the characterization of integrated photonics. A special emphasis is put on numerical models to describe optical measuring methods and processes for 2-D surface 3-D volumetric metrology based on confocal microscopy and optical coherence tomography (OCT). The results also include calibration strategies and

standards especially suited for these devices. In addition to geometrical measurement procedures, we present a novel refractive index measurement method using OCT and a phase retrieval approach.

- Research focusing on low-cost and potentially reel-to-reel capable manufacturing methods are presented and discussed in **Subsection 5.2**. The investigated processes include hot embossing combined with doctor blading utilizing low-cost core monomers as well as a novel lamination process which links chemically incompatible polymers to embedded multimode waveguides. Furthermore, improvements of maskless lithography and its applications not only for the fabrication of waveguides but also for diffractive optical elements (DOEs) are reported.
- **Subsection 5.3** briefly summarizes self-implemented optical design algorithms used in this work. In addition, we present a novel method to numerically design free-form DOEs also taking deformations of the DOE's micro- and macro-topography into account which occur due to hot embossing and deep drawing used to fabricate DOEs.
- Optical interconnects and coupling structures for integration into PLCs are subject of **Subsection 5.4**. We present optical design and fabrication methods for micromirror and grating couplers. In addition, we present a novel approach to create self-aligning coupling elements based on self-written waveguides (SWWs). To demonstrate the capability of our approaches, we integrate inorganic as well as organic light sources and detectors into waveguide foils using our coupling concepts.
- In **Subsection 5.5**, a novel displacement, tilt and strain sensor concept is introduced which is based on intensity modulation between two waveguide arrays facing each other. The sensor was fabricated through the reactive lamination method presented in Subsection 5.2. Experimental and theoretical results are provided to characterize the sensor performance. Furthermore, we demonstrate results on laser-written Bragg grating sensors inscribed into hot embossed waveguides (Subsection 5.2).

4 Fundamentals of Integrated Optics and Photonics

4.1 Waveguide Fundamentals

4.1.1 Light Propagation in Waveguides

Optical waveguides form the building blocks of almost every integrated optical sensor system. According to Tong in [2], optical waveguides can be classified with respect to their guiding mechanisms into

- Total internal reflection (TIR),
- Antiguiding,
- Photonic bandgap,
- Antiresonant guiding,
- TIR in metamaterials.

Other classifications also include the geometry of waveguides, number of guided modes and materials utilized for fabrication of guiding structures, which will be described later in this section. The most basic type of waveguide structure is a slab waveguide, which is either made from two plane-parallel and reflecting plates or two dielectric materials with refractive indexes n_{clad} and n_{core} , where the material with the refractive index n_{core} forms a core layer as shown in Figure 4.1. To achieve wave guiding, it is further required that $n_{\text{clad}} < n_{\text{core}}$.

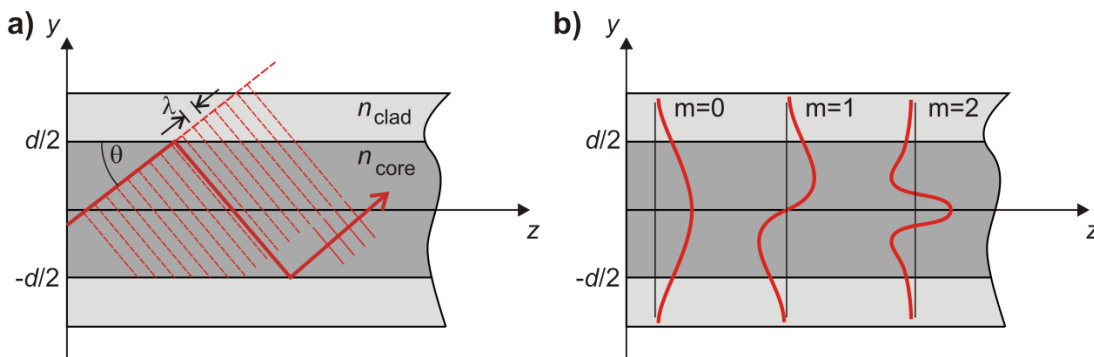


Figure 4.1: Sketch of a slab waveguide and ray propagation in the waveguide core: a) ray-optical and (b) wave-optical model (according to [16]).

Fundamental waveguide theory is either based on Maxwell's equations or a ray-optical approach with principle boundary conditions which need to be fulfilled by the electromagnetic field components [16], [17], [18]. Wave guiding within the ray-optical approach is sketched in Figure 4.1(a) for a slab waveguide. A ray has to fulfill two conditions to be guided: First, the angle of incidence θ needs to be smaller than the critical angle θ_c so that the ray undergoes TIR and, secondly, the phase fronts of the ray need to match after two reflections inside the waveguide and,

thus, interfere constructively, as shown in Figure 4.1(a). As a consequence, only a discrete number $m \in \mathbb{Z}$ of angles of incidence θ_m are accepted by the waveguide and lead to wave propagation. These discrete angles are associated with optical modes of the waveguide. However, if the angle θ_m exceeds θ_c , a fraction of optical power leaks into the cladding region of the waveguide and light is not confined within the waveguide's core. The angle of acceptance θ_i is defined by the numerical aperture (NA) of the waveguide [16] and reads

$$\text{NA} = \sqrt{n_{\text{core}}^2 - n_{\text{clad}}^2} = \sin(\theta_i). \quad (4.1)$$

Within the wave-optical approach, the electromagnetic field inside and outside the waveguide has to follow Maxwell's equations and also has to meet certain boundary conditions. Most importantly, the electrical field $\mathbf{E}(\mathbf{r})$ and the magnetic field $\mathbf{H}(\mathbf{r})$ at the Cartesian coordinates $\mathbf{r} = (x, y, z)$ need to be continuous and differentiable and solve Maxwell's equations

$$\nabla \times \mathbf{E}(\mathbf{r}) = -\mu_0 \frac{\partial \mathbf{H}(\mathbf{r})}{\partial t}, \quad (4.2)$$

$$\nabla \times \mathbf{H}(\mathbf{r}) = -\epsilon_0 n^2 \frac{\partial \mathbf{E}(\mathbf{r})}{\partial t}, \quad (4.3)$$

where μ_0 , ϵ_0 and t denote the vacuum permeability, the vacuum permittivity and time, respectively. In Equation 4.2 it is implicitly assumed that all media are free of charges, non-magnetic, and no currents are present as in the case of dielectric media such as the material utilized for polymer waveguides [19]. Waves travelling inside a uniform waveguide are typically distinguished according to their state of polarization [2]:

- (1) TEM fields with no electrical or magnetic field components in the direction of propagation (z -direction) and, thus, $\mathbf{E} = (E_x, E_y, 0)$ and $\mathbf{H} = (H_x, H_y, 0)$,
- (2) TM fields with no magnetic ($H_z = 0$) but an electrical field component ($E_z \neq 0$) in direction of propagation,
- (3) TE fields with a magnetic ($H_z \neq 0$) but no electrical field component ($E_z = 0$) in direction of propagation.

In analogy to the ray-optical point of view, as illustrated in Figure 4.1 (a), basic solutions to Maxwell's equation are plane waves defined by

$$\mathbf{E}(\mathbf{r}) = \mathbf{E}_0(x, y) e^{i(\omega t - \beta z)} \quad (4.4)$$

$$\mathbf{H}(\mathbf{r}) = \mathbf{H}_0(x, y) e^{i(\omega t - \beta z)} \quad (4.5)$$

where ω is the frequency of the wave and \mathbf{E}_0 and \mathbf{H}_0 are the initial complex electric and magnetic field amplitudes at $z = 0$ and $t = 0$, respectively [20]. Recalling that a slab waveguide has an infinite extent in x -direction, we readily set $\partial \mathbf{E} / \partial x = 0$ and $\partial \mathbf{H} / \partial x = 0$. Propagating waves in TE or fundamental TEM polarization satisfy the wave equation which is obtained by inserting Equation (4.4) and (4.5) into Equations (4.2) and (4.3) and omitting the time dependence of the plane wave solution it reads for the electric field

$$\frac{d^2 E_x}{dy^2} + (k^2 n^2 - \beta^2) E_x = 0. \quad (4.6)$$

Equation (4.6) is a linear and homogeneous differential equation, which is solved by a set of linearly independent eigenfunctions which, again, correspond to optical modes propagating inside the waveguide. The magnetic field analog to Equation (4.6) is derived in a similar way and is omitted here for brevity [20]. According to [16], an eigenfunction solution to Equation (4.6) for a linear slab waveguide with width d is given by

$$E_x(y, z) = \sum_{m=0}^{\infty} a_m u_m \exp(-i\beta z), \quad (4.7)$$

where u_m are the optical mode (eigen)functions with amplitudes a_m . The mode functions are given by

$$u_m(y) = \begin{cases} \cos\left(\frac{2\pi \sin(\theta_m)}{\lambda} y\right), & m = 0, 2, 4, \dots \\ \sin\left(\frac{2\pi \sin(\theta_m)}{\lambda} y\right), & m = 1, 2, 3, \dots \end{cases} \quad \text{for } -\frac{d}{2} \leq y \leq \frac{d}{2}, \quad (4.8)$$

and

$$u_m(y) = \begin{cases} \exp(-\gamma_m y), & \text{for } y > \frac{d}{2} \\ \exp(\gamma_m y), & \text{for } y < -\frac{d}{2} \end{cases}, \quad (4.9)$$

where d denotes the width of the waveguide as shown in Figure 4.1 and

$$\gamma_m = n_2 k_0 \left(\frac{\cos^2 \theta_m}{\cos^2 \theta_c} - 1 \right)^{\frac{1}{2}}. \quad (4.10)$$

Also, $\gamma_m^2 = \beta_m^2 - n_2^2 k_0^2$ where γ_m is known as extinction coefficient. The practical implication of the eigenfunction solutions given by Equations (4.7) to (4.10) can be summarized as follows: In a slab waveguide exists a discrete set of modes with harmonic electric (and magnetic) fields inside the core region which propagate inside the waveguide. The oscillation frequency of a mode increases with its order m as sketched in Figure 4.1(b). Due to boundary conditions for electric and magnetic fields at dielectric interfaces, there is also a field present within the cladding region which decays exponentially and is known as the evanescent field. The extinction coefficient defined by Equation (4.10) implies that waveguide modes where the propagation angle θ_m exceed the critical angle θ_c also propagate inside the cladding region and, thus, the corresponding wave is not confined inside the waveguide core. Hence, these modes do not lead to wave guiding inside the core region. The critical angle is defined as $\cos \theta_c = n_2/n_1$.

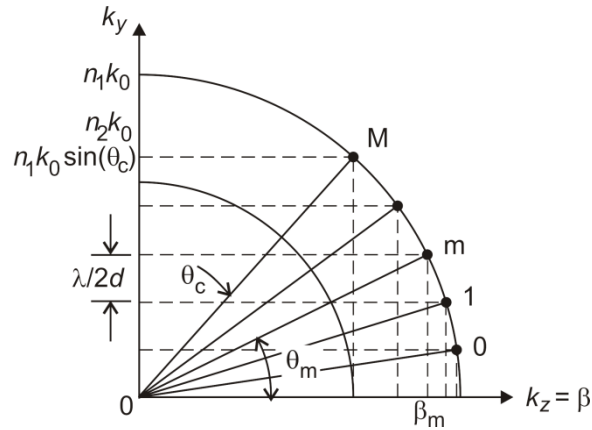


Figure 4.2: Discrete propagation angles θ_m and propagation constants β_m of a mode m accepted by a slab waveguide with refractive indexes n_1 and n_2 (according to [16]).

As modes are represented by plane wave solutions given by Equations (4.4) and (4.5), each solution propagates in direction of its wave vector $\mathbf{k} = (k_x, k_y, k_z)$ with its constant absolute value being $k = |\mathbf{k}| = 2\pi/\lambda$. Since plane wave solutions are discrete due to consistency with boundary conditions, there exists only a discrete set of wave vectors with values in z -direction $k_z = \beta_m$ where

$$\beta_m = n_1 k_0 \cos \theta_m, \quad (4.11)$$

which is denoted as propagation constant. A graphical visualization of propagation constants β_m for a given number of modes M is depicted in Figure 4.2 [16]. Only propagation constants in the interval $n_1 k_0 \leq \beta_m \leq n_2 k_0$ lead to wave propagation. The distance between adjacent modes in k_y -direction is constant and amounts to $\lambda/2d$. The number of modes in a slab waveguide is given by

$$M = \left\lceil 2d \frac{\sin \theta_c}{\lambda} \right\rceil = \left\lceil 2 \frac{d}{\lambda} \text{NA} \right\rceil, \quad (4.12)$$

where $\lceil \cdot \rceil$ denotes the ceiling function. Note, that we restricted ourselves to slab or two-dimensional waveguides to describe basic properties of waveguides. In practical application cross sections of waveguide exhibit various geometries and also refractive index distributions depending on the field of application and the specific fabrication technique. For complex geometries and index distributions, the number of modes M needs to be calculated by means of numerical methods. However, a simple two-dimensional example of practical relevance is a rectangular cross section with width and height d and a homogeneous refractive index distribution within the core as well as the cladding region. In this case the number of modes can be approximated by [16]

$$M \approx \frac{\pi}{4} \left(\frac{2d}{\lambda_0} \right)^2 \text{NA}^2. \quad (4.13)$$

The approximated number of modes M only includes those modes in TE polarization. The same number of modes propagates if the field incident on the waveguide also excites modes in TM polarization.

4.1.2 Basic Waveguide Geometries and Structures

While the theory described in the previous section is based on slab and rectangular waveguide cross sections only, in practical applications there exists a vast amount of different other frequently used geometries. The choice of a specific cross section is not only based on the application purpose but also on the waveguide materials and fabrication processes at hand.

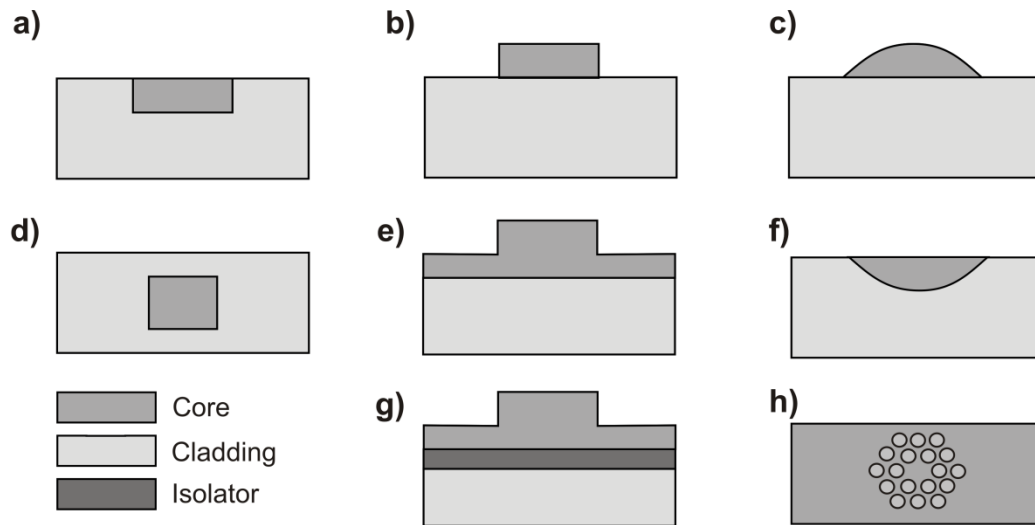


Figure 4.3: Cross sections of different types of waveguides: embedded waveguides (a,d,f), strip waveguides (b,c,g) and photonic crystal waveguide (h).

Common types of cross sections are sketched in Figure 4.3 (compare [2, 16, 20]). Waveguides can be distinguished into embedded waveguides which are either completely buried inside a cladding

substrate as shown in Figure 4.3(d) or partially superficial as shown in Figure 4.3(a) and (f). Strip waveguides are also fabricated as complete superficial structures as illustrated in Figure 4.3(b) or (c) as rib or ridge waveguides displayed in Figure 4.3(e) which are sometimes also placed on an additional isolator layer between substrate material and ridge waveguide as sketched in Figure 4.3(g). A special category of waveguides are photonic crystal structures as illustrated in Figure 4.3(h). Here, periodic structures which are perpendicularly oriented to the direction of wave propagation serve as cladding such that wave guiding only takes place inside the center of the structure. Note, Figure 4.3 gives only a few examples of commonly used waveguide cross sections and other geometries are also suitable for wave guiding. Recent research also focuses on metamaterials and plasmonic structures to guide light due to their potential to be integrated at a higher density, thus, allowing smaller features such as bent waveguides with smaller bend radii. However, these structures rely on the excitation of free electron oscillations and, therefore, require metallic materials for wave guiding such as gold or silver or highly doped semiconductors which are placed on an isolator with certain requirements on the complex refractive index boundaries [21]. Another drawback is the very limited propagation length of the excited surface plasmon polaritons due to high absorption of energy by the carrier material. Since we focus on polymer based systems in this work, metamaterial and plasmonic waveguides are beyond the scope of this work.

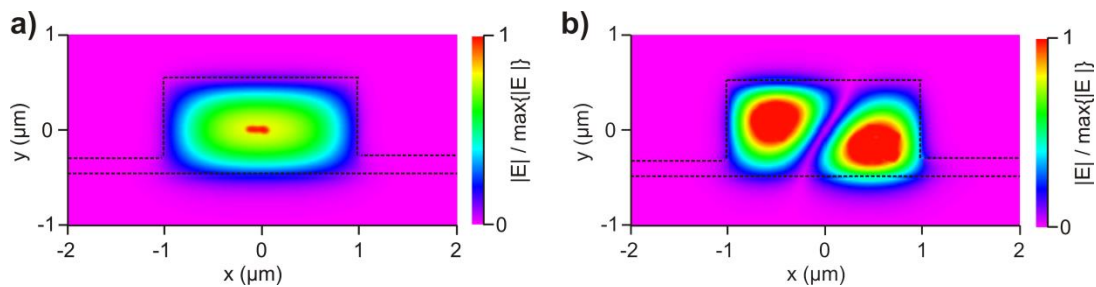


Figure 4.4: Simulated normalized electric field inside a ridge waveguide with core refractive index of 1.52, substrate refractive index of 1.49 and refractive index of the cover layer of 1: a) visualization of fundamental mode and of b) higher order mode.

As mentioned in the previous section, the number M of propagating modes strongly depends on the geometry of the cross section of the waveguide, its diameter and the refractive indices of the materials used as cladding and core materials. In general, the number of modes and the corresponding electric and magnetic fields can only be determined utilizing numerical simulations. Exemplary results of a numerical simulation of the fundamental and higher order modes propagating inside a ridge waveguide are shown in Figure 4.4(a) and Figure 4.4(b), respectively. The simulation is based on the beam propagation method presented in Section 4.4.3.

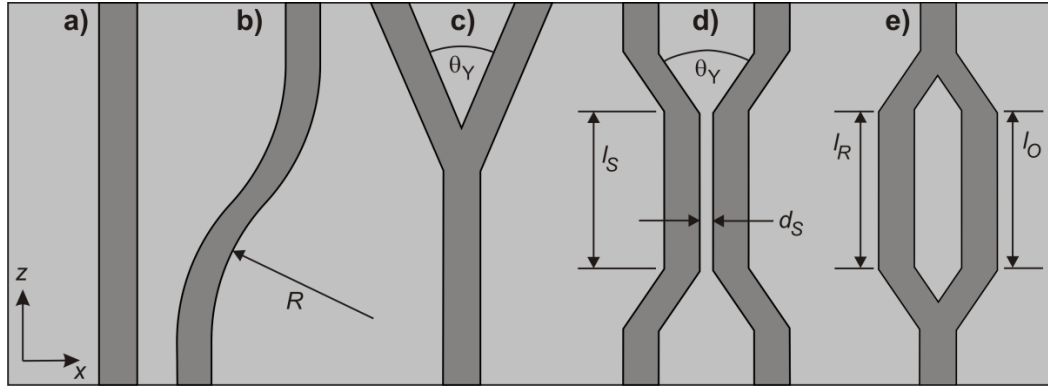


Figure 4.5: Various configurations of waveguide based integrated photonic structures according to [16]: (a) straights; (b) bends; (c) Y-shaped beam splitters; (d) directional coupler; Mach-Zehnder interferometer (darker areas correspond to an increased refractive index).

The choice of a specific waveguide cross section also depends on the field of application of the integrated optical system. According to Saleh and Teich in [16], waveguide devices in integrated circuits can be distinguished in (1) passive devices such as straight, bent and S-shaped waveguides as well as branched waveguides and directional couplers to name just a few and (2) in active components or functional devices which alter the electromagnetic field of a propagating wave. The latter class includes devices to control guided waves by electro-optical or magneto-optic effects and also non-linear material effects to give a few examples. Basic wave guiding structures are shown in Figure 4.5.

In addition to basic straight and bent waveguides as sketched in Figure 4.5(a) and (b), prominent examples of guiding structures include beam splitters such as Y-shaped waveguides as in Figure 4.5(c) and directional couplers such as evanescent field couplers shown in Figure 4.5(d). Important parameters for the design of beam splitters such as Y-shaped 3 dB splitters are the opening angle θ_Y between the two output ports as well as a large bending radius R of the output port waveguides which is often S-shaped as sketched in Figure 4.5(b). Splitting one waveguide into two output ports is accompanied with losses, which are also mode dependent since higher order modes penetrate deeper into the cladding region [22]. In [23], Kuznetsov derived approximations to describe radiation losses in Y-splitter in closed form and showed that losses reduce significantly if the splitter satisfies the relation

$$\theta_Y < \cos\left(\frac{n_{\text{clad}}}{n_{\text{core}}}\right) - \arctan\left(\frac{k_x}{k_z}\right). \quad (4.14)$$

In the previous expression, k_x and k_z point perpendicular to and in direction of the wave propagation, respectively. Equation (4.14) implies that a higher refractive index step allows larger opening angles θ_Y due to a better wave confinement [22]. The same applies to bends where a larger refractive index difference leads to lower bend losses at a fixed bend radius R . An alternative

approach to split or merge light beams is an evanescent field coupler, also referred to as proximity or direction coupler, as shown in Figure 4.5(d). Here, two linear waveguides run parallel with respect to each in a defined distance d_s . The splitting ratio of the device depends on d_s , the refractive index n_{clad} of the surrounding cladding material as well as the splitter length l_s , see Figure 4.5(d). Yariv and Yeh derived an expression in [24] to describe the coupling constant for each TE mode m which reads

$$\kappa = \frac{2\beta_{x,m}\gamma_m \exp(-\gamma_m d_s)}{\beta_m \left(d + \frac{2}{\gamma_m}\right) (\beta_{x,m}^2 + \gamma_m^2)} k_0^2 (n_{\text{core}}^2 - n_{\text{clad}}^2). \quad (4.15)$$

Here, $\beta_{x,m} = \sqrt{\beta_m^2 - k_0^2 n_{\text{core}}^2}$ is the propagation constant in x-direction. Note that κ is given in units of m^{-1} and, thus, states how much energy is transferred independent of the coupler length in z-direction. If we assume an incident electrical field E_{in} at one coupler port while the field at second port is identical to zero, the electrical field at the opposite exit port of the coupler is given by $E_{out} = E_{in} \sin(\kappa z)$. Thus, to obtain a 3 dB coupler, it is required that $\kappa \cdot l_I = \nu \cdot \pi/2$ where ν is an integer number.

For sensing applications and also intensity modulation, Mach-Zehnder interferometers (Figure 4.5(e)) have been proven suitable to be integrated in photonic devices [16, 22]. Such devices consist of a 3 dB Y-splitter and a 3 dB Y-combiner and two interjacent interferometer arms. If a phase change $\Delta\varphi$ is introduced in one arm with respect to the other, the intensity I_{in} at the input port is modulated and relates to the output intensity I_{out} as [22]

$$\frac{I_{out}}{I_{in}} = [1 + \cos(\Delta\varphi)]. \quad (4.16)$$

If we assume the interferometer arms to be equal in length $l_I = l_O$ and, in addition, that the phase change is introduced by refractive index changes Δn of the waveguide's core material only, the phase change is given by $\Delta\varphi = k \cdot \Delta n \cdot l_O$.

4.1.3 Light Coupling

Integrated photonic devices require coupling strategies to transfer light between optical elements such as waveguides, light sources and detector. The coupling efficiency η of an optical coupling element is defined as the ratio between the energy which is emitted by the first element and the energy which is received by the second element. It is the key parameter when designing optical coupling structures while the specific design of such elements is highly dependent on the optical elements to be connected.

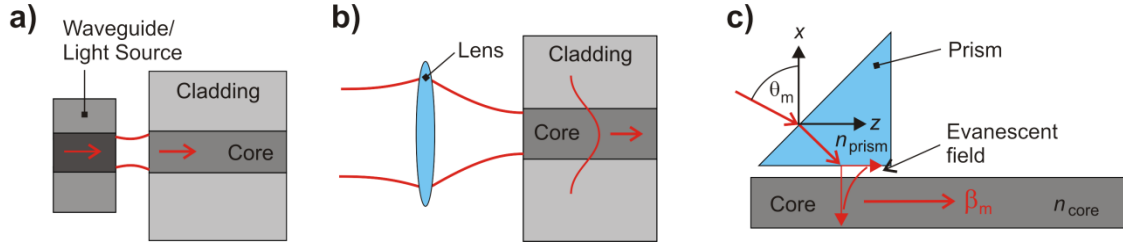


Figure 4.6: Coupling strategies for free space coupling of light into a waveguide: a) butt coupling; b) direct focusing or end-fire coupling; c) prism coupling (according to [16, 22, 25]).

Commonly applied coupling strategies for free space coupling are sketched in Figure 4.6. A frequently used strategy is butt coupling, where optical elements are connected by placing them as close to each other as possible, as shown in Figure 4.6(a). Butt coupling is typically employed for fiber-to-fiber, fiber-to-waveguide or laser diode (LD) to waveguide coupling due to its simple optical setup. However, a high lateral positioning accuracy of less than 100 nm is required and the remaining spacing between optical elements typically needs to be less 1 μm to achieve a high coupling efficiency [22]. Theoretically, coupling efficiencies can be as high as $\eta = 1$ but experimentally achieved values of approximately $\eta = 0.7$ for singlemode LD to waveguide coupling were reported [25]. A significant limitation of this method is a strong dependence of the coupling efficiency on the separation of both components due to interference effects resulting from multiple facet reflections [22, 25]. An alternative approach to couple light from a light source such as a laser into a waveguide is direct focusing, also referred to as end-fire coupling as shown in Figure 4.6(b), which is often used in laboratory setups [25]. Here, a light beam is focused into the waveguide by a lens or microscope objective. To achieve high coupling efficiencies one needs to match the NA of the waveguide and the focusing lens to transfer maximal energy into a guided waveguide mode. The method is often used to excite the 0-order mode in a waveguide by focusing a TEM mode of a laser onto the end facet of the waveguide. A third frequently employed method is prism coupling which is used if light is coupled in a vertical direction into a buried waveguide and, in addition, only the surface of the waveguide is accessible, as sketched in Figure 4.6(c). To couple light directly into a waveguide, coupled light and modes propagating in z-direction inside the waveguide have to fulfill phase matching conditions, which is impossible for realistic angles of incidence of the coupling beam [25]. Hence, prisms which couple light by transferring an evanescent field created by TIR inside the prism into the waveguide are required. There, energy is transferred if the propagation constants of modes traveling inside the prism and the waveguide match and following condition holds:

$$\beta_m = \frac{2\pi n_p}{\lambda_0} \sin \theta_m , \quad (4.17)$$

where n_p and θ_m are the refractive index of the prism and the angle of incidence as defined according to Figure 4.1, respectively. The coupling efficiency of a prism coupler depends on the

separation between the prism and the waveguide, the coupling length determined by the beam diameter of the laser which also depends on the specific mode to be coupled. Prisms represent an efficient way to couple light, but it is required that the refractive index n_p of the prism is higher in comparison to the refractive indices n_{core} and n_{gap} of the core of the waveguide and the material between the prism and the core, respectively [25]. This requirement is especially restrictive in silicon photonics where the refractive index of materials is typically larger than $n = 3$. However, polymer materials typically exhibit refractive indices in the range of $n = 1.49 \dots 1.6$ in the VIS and, hence, prism coupling is easily achieved by means of prisms made from standard glass.

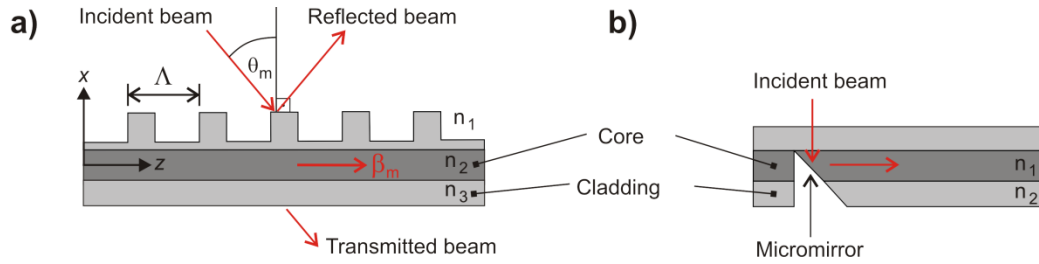


Figure 4.7: Coupling structures frequently used in integrated photonics: a) grating coupler; b) micromirror coupler (according to [25, 2, 26]).

Coupling strategies discussed so far are frequently used under laboratory conditions where free space optical setups are the most suitable choice. When integrating optical elements into PICs or other devices, alternative strategies are required which provide a high coupling efficiency but are, in addition, easy and cost efficient to fabricate utilizing standard manufacturing techniques. The selection of a specific coupling strategy depends especially on the size and material of the waveguides. If the photonic structure is based on singlemode waveguides, grating couplers are frequently employed, as sketched in Figure 4.7(a) [22, 25]. Grating couplers diffract an incident light beam into diffraction orders which excite modes inside the waveguide [26]. A prerequisite for a grating coupler is that a diffraction order of the grating matches with a propagating mode. Due to the periodicity of the grating, harmonics of the propagating field underneath the grating are introduced and their propagation constants read

$$\beta_\nu = \beta'_m + \nu \cdot K, \text{ with } \nu = 0, \pm 1, \pm 2, \dots, \quad (4.18)$$

where β'_m is the propagation constant of the m -th mode within the grating region which approximately equals β_m [25]. $K = 2\pi/\Lambda$ denotes the absolute value of the grating vector, where Λ is the grating period, as indicated in Figure 4.7(a). The propagation constants now satisfy the phase matching condition

$$\beta_\nu = k_0 n_1 \sin \theta_m. \quad (4.19)$$

Again, θ_m is the angle of incidence as defined according to Figure 4.7(a) and k_0 denotes the wavenumber in vacuum. For VIS applications, grating periods typically range between $\Lambda = 100$ nm to 300 nm. However, the efficiency η of a grating coupler not only depends on the height of the grating structure but also on the type of grating. Coupling efficiencies of up to $\eta = 0.5$ were reported for rectangular gratings while blazed or saw tooth shaped gratings yield efficiencies up to $\eta = 0.95$ [25]. However, for multimode waveguides where hundreds or even more modes propagate inside the waveguide simultaneously, high coupling efficiencies cannot be accomplished using grating couplers. A simple alternative to couple light in a vertical direction are micromirror couplers, as sketched in Figure 4.7(b). These couplers are based on reflecting surfaces at an angle of typically 45° with respect to the direction of light propagation inside the waveguide to couple light coming from the vertical direction into the waveguide. Reflection is either achieved by exploiting TIR or by coating a reflective layer made from metal onto the micromirror surface.

4.2 Fabrication methods

In this Section, an overview of techniques for the fabrication of integrated photonics and especially waveguides is given. The selection of processes includes standard techniques in micro-optics and is not restricted to those used in polymer photonics which in turn are also utilized for the fabrication of inorganic optical devices. The latter class of processes was used in our own research to create hot embossing stamps and functionalized surface coatings, as described in detail in Section 5. However, the majority of processes described in this section are also utilized to create polymer or hybrid metal-polymer coatings [9]. Note that the selection of processes is not complete but intended as an overview of the most common ones. The following subsections are distinguished into methods which are used to deposit layered materials or to alter properties of layered structures, or are used to directly structure materials.

4.2.1 Fabrication of Film Structures

Deposition from liquid solutions

Deposition methods are frequently used when dealing either with monomers such as methyl methacrylate (MMA) or polymers which are dissolved in solvents such as PMMA in chloroform and also toluene solution as well as epoxy resins in commercial solvents. Also, multi-component solutions including, for instance, nanoparticles such as TiO_2 can easily be distributed on a substrate in thin layers with thicknesses down to the few nanometers range. A method used in wafer processing technology is *spin coating*. Here, a substrate, such as a silicon wafer, is positioned on a vacuum chuck and rotated at speeds which are typically in the range between a few hundred and thousand revolutions per minute (rpm). When a liquid material is dispensed onto the rotating substrate, it forms a uniform layer where the thickness depends on the viscosity of the liquid and the rotational speed of the spin coater. Alternatively, the substrate can be submerged in the liquid and removed at a defined speed, which is referred to as *dip coating*. Both processes require a

subsequent thermal treatment in an oven or on a hot plate to remove the solvent or to polymerize the monomers. A method which is, in addition, also reel-to-reel capable is *doctor-blading*, which takes advantage of a sharp blade which is guided at a fixed distance to the substrate and distributes the liquid homogeneously.

Physical Vapor Deposition (PVD)

In PVD a material is vaporized from a liquid or solid phase and deposited onto a substrate at an atomistic or molecular level [27]. The vapor is transported either through vacuum or low pressure gases which also includes plasma environments. Film thicknesses fabricated by PVD typically range from a few to several thousand nanometers, which are formed at deposition rates between 0.1-1 nanometers per second. The process also lends itself to create multi-layer films made from various materials. The term PVD summarizes various processes including thermal evaporation, sputter deposition and ion assisted deposition [27].

During *thermal evaporation* a material from a thermal vapor source is deposited without or, with hardly, collisions experienced from the ambient gas particles [2, 27]. *Sputter deposition* relies on the deposition of atoms which are physically ejected from a target material by transferring the momentum of particle bombardment to the solid target. The bombarding particles usually consist of ions accelerated from plasmas. Commonly, metals, semiconductor materials and also compound materials are utilized as target materials such as gold, silver, alloy and even composed transparent electrodes consisting of indium tin oxide (ITO) [27]. To selectively alter thin film properties, *ion assisted deposition* (IAD) utilizes simultaneous or periodic varying bombardment of atomic-sized particles [27]. The properties of the created film is highly determined by the energy, flux and mass of the particles used for bombardment. Ions to be deposited on the substrate also referred to as film ions are either generated from plasmas or launched from a separate ion gun.

Chemical Vapor Deposition (CVD)

In CVD a chemical reaction of gases leads to a deposition of materials onto a substrate. It is a prominent method in semiconductor processing [27]. There exist various CVD methods which are carried out under quite different conditions such as temperature or chamber pressure depending on the specific film material to be coated. All CVD processes are similar in that a thin film is formed on a substrate from chemical vapor precursors by either high temperature reduction or decomposition. Reduction takes place at higher temperatures typically with the aid of hydrogen, whereas decomposition requires thermal activation.

A standard technology is *plasma enhanced CVD* (PECVD), which is frequently utilized for waveguide fabrication using materials such as Si_3N_4 [2]. During the process, plasma is created through electromagnetic fields at radio frequencies or direct current discharge between electrodes from reacting gases. PECVD devices are commonly operated at pressures of a few torr and deposition rates are in the range of 5-100 nm/min [27]. Thin films fabricated by PECVD are usually tempered at

approximately 1000 °C in a post process to minimize Si-H and N-H bonds, which increase absorption at wavelengths around 1500 nm [2].

A dominant process in optoelectronics fabrication is *metal-organic CVD* (MOCVD) also known as *organometallic vapor phase epitaxy* (OMVPE). Mono or polycrystalline films are created by crystal growth (epitaxy) due to chemical surface reactions between a substrate, reaction gases and material compounds. MOCVD is a powerful technique to grow materials such as III-V semiconductors, e.g. AlGaAs, among other groups [2].

Epitaxial Growth

Epitaxial methods include a variety of different methods to grow crystal films which also include MOCVD, as described previously. The oldest epitaxial method is *liquid phase epitaxy* (LPE), where crystal growth is achieved by establishing contact between a substrate and a liquid phase [2]. It is inexpensive, however, the layers created are characterized by a poor uniformity. A more sophisticated method compared to LPE is *molecular beam epitaxy* (MBE) which is capable of creating highly uniform layers including metal-organic films. The process relies on effusion cells from which atomic materials are evaporated and deposited onto a substrate. A prerequisite of the process is a high or ultra-high vacuum.

4.2.2 2.5-D and 3-D Micro-Structuring and Replication

Lithographical and Etching Methods

In silicon photonics, etching techniques are frequently applied to create three-dimensional structures in various materials including silicon or silica. Etching typically is differentiated in wet and dry etching techniques where either liquids or vapors and plasmas are utilized as reactants, respectively [28]. In general, wet etching takes place at faster rates compared to dry etching, but etching rate and selectivity of the process can be modified by an adequate choice of the etchant. Etching methods are characterized by an isotropic or anisotropic behavior, as shown in Figure 4.8(a) and (b). Commonly, anisotropic wet etching is utilized to obtain V-shaped grooves in silicon or other materials. This is achieved due to the crystallographic orientation of the material to be etched, as shown in Figure 4.8(a). In silicon, etching rates are fastest along the $\langle 111 \rangle$ orientated planes which yields grooves at a characteristic angle of $54,7^\circ$ due to the crystallographic orientation in silicon. To achieve 2.5-D structures in bulk micromachining, resist layers are required which serve as lithographical masks such as thermally grown SiO_2 . In contrast, anisotropic etching takes place regardless of the crystallographic planes at the same etching rate in all directions, as illustrated in Figure 4.8(b). However, the etching rate in vertical direction is most often much faster in wet etching which leads to the undesired edge profile sketched dashed line in Figure 4.8(b). This effect is prevented by carrying out vigorous stirring of the etchant which yields undercuts sketched as solid lines in Figure 4.8(b). In addition to wet etching there exist various dry etching methods, such as

plasma etching where, for instance, an O_2 plasma acts as etchant. Plasma etching was applied in this work to achieve optically smooth flanks in silicon.

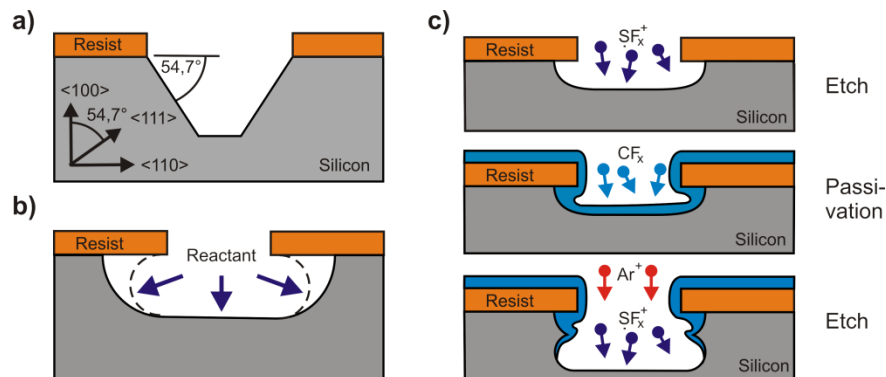


Figure 4.8: Etching methods utilized in photonics: a) anisotropic etching; b) isotropic etching; c) deep reactive ion etching (DRIE) (adapted from [29]).

Another process which was utilized in this work to achieve vertical flanks in silicon was deep reactive ion etching (DRIE) also referred to as the Bosch process [30, 29]. As illustrated in Figure 4.8(c), it is accomplished by an initial etching process step by applying an anisotropic SF_6 chemistry, which forms a typical groove shape as shown in Figure 4.8(b). During the next process step, a polymer resistant layer is deployed onto the silicon and prevents the sidewalls of the silicon groove from being etched. The passivation is followed by another etching process using SF_6 chemistry and a carrier gas, such as Argon. These processes are performed in an alternating order until a predefined groove depth is reached [30].

LIGA (Lithographie, Galvanik, Abformung) - as a non-silicon based technology - represents an alternative to DRIE as fabrication technology, and is commonly applied to create hot embossing stamps [31]. During this process, a resist made from poly(methyl methacrylate) (PMMA) coated on an electrically conducting substrate is structured by X-ray exposure. After development of the resist and, as a consequence, removal of the unexposed resist, the microstructure is built by electroplating and the remaining resist is removed subsequently.

Direct structuring

Laser ablation is a versatile tool used to structure a large variety of materials including polymers, semiconductors and metals [31, 32]. Due to high absorption of most materials in the UV, pulsed laser systems such as CO_2 , excimer or Nd:YAG solid state lasers are commonly used with pulse durations down to femtoseconds [33, 31]. For material ablation, the laser beam is usually focused onto the substrate to be structured and guided via galvanic scanners to achieve a lateral movement of the writing laser beam. Ablation is conducted at energy densities in the few to few ten mJ/cm^2 range. The lateral feature size which can be manufactured depends on the laser wavelength and the focusing optics as well as on the specific kind of surface-laser interactions and is commonly above $1 \mu m$ but can reach the sub-micron range using, e.g., holographic techniques [34].

An alternative method which is often utilized for fabrication of mold inserts in hot embossing and injection molding as well optics fabrication is ultra-precision (UP) diamond tooling [9, 31]. The process is either set up as milling or turning process where a mono- or polycrystalline diamond tool punctually ablates substrate material. In general, all materials which do not contain carbon can be structured. Frequently used materials include nickel, copper and optical polymers such as PMMA, PC, among others, due to their capability to provide a surface roughness in optical quality after processing. However, such processes are limited to certain geometries since the fabricated surface is always a convolution of the planed tool path and the tip shape of the diamond tool and, therefore, are not very flexible. Thus, diamond tooling is not a suitable technique for singlemode waveguide fabrication due to tools sizes which exceed required feature sizes to create singlemode structures.

Nanoimprint Lithography

To create 2.5-D geometries in polymers or glasses, various methods have been developed during the last two decades which are commonly summarized as nanoimprint lithography (NIL) [31]. Depending on the materials utilized for fabrication of nano- and microstructures, these processes can be subdivided into thermal, UV curing and printing based methods.

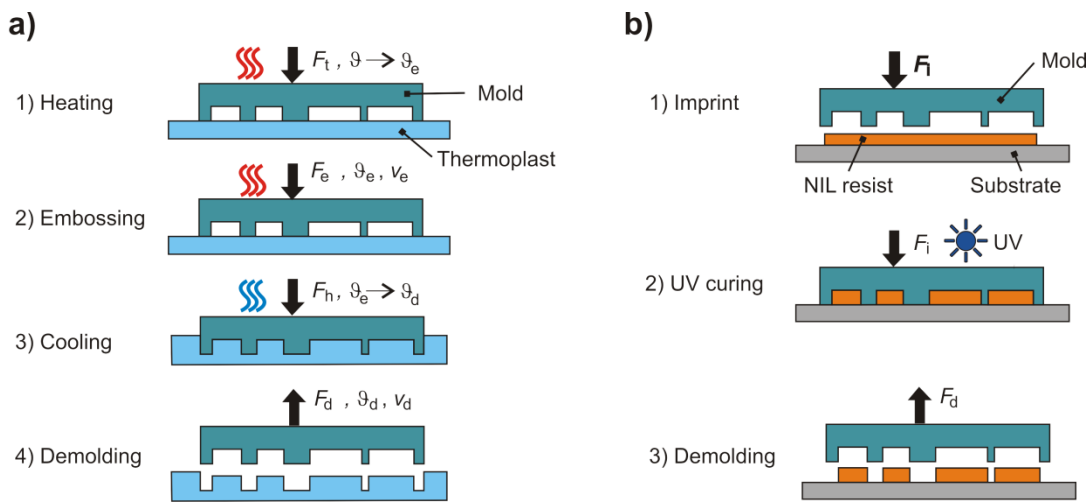


Figure 4.9: Nanoimprint lithography: a) thermal hot embossing; b) UV nanoimprint.

A first NIL method, hot embossing lithography (HEL) relies on a mold which features a higher heat resistance than the material to be embossed such as thermoplastic polymers. The process is sketched in Figure 4.9(a). First, the mold and substrate are fixated by applying a touch force F_t and heated to the embossing temperature ϑ_e which is above the glass transition temperature T_G of the polymer, see Section 4.3.2. As mold materials metals such as nickel but also semiconductor materials such as silicon are frequently used [9, 31, 34]. Structuring of mold materials is commonly carried out by various etching methods or diamond tooling, as described previously in this Section. After heating, the mold is driven into the substrate at an embossing speed v_E by applying an

embossing force F_E . Since the substrate is in a viscous state, material flow results in a deformation of the substrate and, thus, to a decrease of the embossing force if not counteracted by a suitable mold feed. Hence, there are different strategies to control the process: The first approach is force controlled, where the force is monitored and the mold is fed to achieve a constant force F_E . Secondly, the feed is dependent on the mold position and is discontinued if a certain mold position with respect to the substrate is reached. Commonly, the control strategy is carried out for a defined embossing time t_E to allow the viscous polymer to completely fill the microstructures of the mold. Subsequently, mold and substrate are cooled down to the demolding temperature ϑ_d , where mold and substrate are separated by applying a demolding force F_d . Demolding may also be carried out at a fixed demolding speed v_d which, again, is controlled. The latter parameters are important to prevent ridges or edges to be deformed or damaged during demolding.

In contrast to HEL, UV nanoimprint lithography (UV-NIL) is based on UV curing of liquid monomers rather than on a change in rheological properties of polymers due to a raised temperature. A typical process cycle in UV NIL is shown in Figure 4.9(b). A mold is pressed into the liquid monomer which is coated on a substrate such as glass or silicon by applying an imprint force F_I . Commonly, UV light at a wavelength typically ranging between 400 nm and 365 nm is radiated through the mold which requires the mold to be transparent in this wavelength range. Thus, different types of glass and polydimethylsiloxane (PDMS) are frequently utilized as mold materials. In the next process step, the monomer is cured through UV exposure until the monomer is fully polymerized and the mold is removed using a demolding force F_d subsequently. Comparing HEL and UV-NIL, feature sizes created by the latter method have been reported down to a few nanometers while HEL is capable of reproducing structures which exhibit sizes of a few ten nanometers [31].

A third method which is also considered to be an NIL technique is micro contract printing (MCP or μ CP) [35]. During the process, a stamp tool is wetted with a liquid ink and pressed onto a substrate. The stamp is usually made from PDMS to obtain a flexible and soft stamp.

Injection Molding

The methods presented so far are suitable for creating micro- and nanostructures in planar substrates. If chip based optical devices such as lab-on-chip sensors are required and in addition high throughput fabrication is required, alternative techniques come into consideration. Especially, micro injection molding is a standard technique in an industrial context. Here, a thermoplastic is heated up to its viscous liquid state and is injected into a high precision mold utilizing extruders [31]. A variation of this method is micro reaction injection molding (RIM), where two different components, which commonly consist of a monomer and a starter, are injected into the mold and a chemical reaction leads to a rigid micro-part [31].

4.3 Materials

The choice of adequate optical materials depends on the application as well as on the fabrication techniques of the integrated device to be fabricated, as introduced in the previous Section. Traditional fabrication methods rely on inorganic materials including silica (SiO_2), silicon (Si) and silicon oxynitride (SiO_xN_y). This material class has served as a leading platform for silicon-on-insulator technology (SOI) due to low optical losses and high temperature stability. However, silicon based devices are limited in wavelength range to telecom wavelength and are not suited for operation in the VIS.

4.3.1 Inorganic Materials

Inorganic materials are classical materials for fabrication of optical fibers but also integrated photonic devices such as optical sensors. The selection of a specific material depends on various parameters of the device such as operating wavelength, maximal operating temperature and optical functionality. The latter parameter relates to special properties of materials such as a strong non-linearity which might even be tunable by external electric or magnetic fields. Such materials, for instance, play an important role when fabricating optical switches [25]. A selection of inorganic materials commonly used in integrated photonics and corresponding manufacturing techniques are given in Table 4.1.

Table 4.1: Selection of important inorganic materials for integrated photonics (according to [2, 36, 37, 38]).

Material	Abbreviation	Fabrication technique	Components	Property
Chalcogenide	-	Vacuum evaporation, reactive deposition, embossing	Photodetectors, interconnects, waveguides	Semiconductor
Gallium arsenide	GaAs	Epitaxy	Waveguides, Substrate	Insulator
Indium gallium arsenide	InGaAs	MBE	Photodetector	Semiconductor, elector-optic
Indium phosphide	InP	MOCVD	Optoelectronic switch	Semiconductor, Electro-optic
Lithium niobate	LiNbO_3	Epitaxy	Modulator, interconnect	Electro-optic
Lithium tantalate	LiTaO_3	Epitaxy	Modulator, attenuator, interconnect	Piezoelectric
Sapphire	Al_2O_3	Epitaxy, reactive deposition	Substrate, waveguides, interconnects	Insulator
Silica	SiO_2	Sol-gel, CVD, PECVD, spin-on	Optical fiber, arrayed waveguide grating, MEMS structures, integrated circuit material	Insulator
Silicon	Si	Epitaxy	Substrate, Waveguide, interconnects, conductive path, mechanical structure	Semiconductor
Silicon nitride	Si_3N_4	CVD	Waveguide, interconnects	Insulator

In application fields such as telecommunication, wavelengths in the NIR and especially around 1.3 μm and 1.5 μm are state-of-the-art. Therefore, silicon became a standard material due to its transmission windows which extends from 1.1 μm to approximately 7 μm in addition to other important materials properties such as high optical damage threshold, high thermal conductivity, and high crystal quality at low material costs. With standard semiconductor fabrication technologies at hand, silicon-on-insulator (SOI) devices also became state-of-the-art. As substrate material fused silica (SiO_2) is often employed as well as sapphire (Al_2O_3) in silicon-on-sapphire (SOS) devices. For mid IR applications in a wavelength range between 2.4 μm and 6.6 μm also nitride serves as substrate material for silicon-on-nitride (SON) devices.

4.3.2 Organic Materials

In silicon photonics, fabrication processes are well established as they are also used for fabrication of micro-electronical devices and integrated circuits. However, such processes are only cost effective in mass fabrication with an extraordinary number of items produced. Therefore, polymers came into attention as an alternative material system for the fabrication of polymer based integrated photonic devices and even circuits (PICs).

In general, polymers consist of macromolecule chains which are built from individual unit cells called monomers [31]. Artificial polymers are made through polymerization, polycondensation or polyaddition where monomers are linked to macromolecule chains through covalent bonds. Polymers are classified according to their internal structure into three classes: thermoplastics, thermosetting polymers and elastomers.

Table 4.2: Properties of selected conventional optical polymers [9, 39, 40].

Polymer	Abbreviation	Type	Refractive index n ($\lambda = 532 \text{ nm}$)	T_g ($^{\circ}\text{C}$)	Attenuation (dB/cm)
Poly (methyl methacrylate)	PMMA	Thermoplast	1.49	105	0.20 (at 850 nm)
Polystyrene	PS	Thermoplast	1.59	100	n.s.
Polycarbonate	PC	Thermoplast	1.56	145	0.15 (at 532 nm)
Cyclic Olefin Copolymer	COC	Thermoplast	1.53	80-160	0.08 (at 532 nm)
Epoxy Resin (e.g. Epocore/Epoclad)	-	Thermosetting	1.51 - 1.57	-	0.10 (at 830 nm)

Thermoplastics consist of linear or branched chains without interlinks [31, 41]. They are characterized by a solid state at a temperature below the glass transition temperature T_g of the specific polymer. If the temperature increases above T_g , polymer segments start to rotate first until the chains are able to move with respect to each other and the polymer softens and gets deformable. Since this process is reversible, the polymer hardens again during cooling and exhibits an amorphous state with intertwined chains or a semicrystalline state with additional regions of parallel oriented chains, depending on the specific polymer.

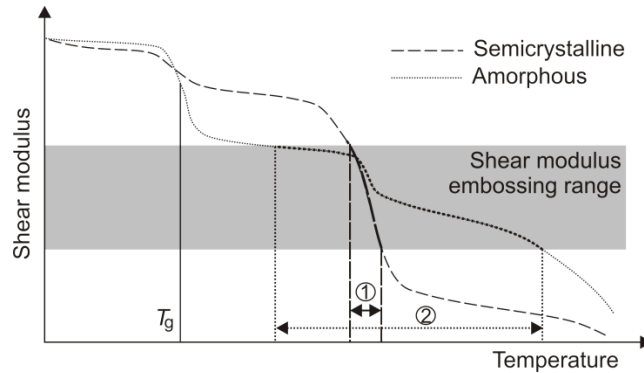


Figure 4.10: Schematic behavior of the shear modulus (logarithmic scale) of amorphous and semicrystalline polymers as function of temperature – embossing temperature range of semicrystalline and amorphous polymers are indicated by “1” and “2”, respectively (according to [41]).

The glass transition temperature T_g of polymers can be determined from the progression of the shear modulus as function of temperature, as shown in Figure 4.10. Around T_g an increase in temperature is accompanied by a rapid decrease of the shear modulus. Amorphous polymers are in a glassy state below T_g and transform into a rubber-like state followed by a viscous state as the temperature increases, both leading to a rapid decrease of the shear modulus. As the temperature is further increased the polymer reaches its decomposition range, where its chains decompose. Semicrystalline polymers exhibit a similar behavior as they consist of amorphous as well as crystalline parts. As the temperature increases towards T_g the amorphous parts of the polymer behave as described above. However, in contrast to fully amorphous polymers the crystalline parts start to melt at higher temperatures where the largest gradient of the shear modulus is observable, as shown in Figure 4.10. As a consequence, the temperature range which is suitable for fabrication processes such as hot embossing is narrower for semicrystalline compared to amorphous polymers, as indicated in Figure 4.10. Examples of commercially available amorphous thermoplastic polymers are poly(methyl methacrylate) (PMMA) or polycarbonate (PC), as summarized in Table 4.2.

The second polymer class, thermosetting polymers, is characterized by cross-links between polymer chains and, as a consequence, cannot be melted [31]. In addition to chemical bonds, physical bonds between polymer chains are also present, which weaken with increasing temperature leading to a decreased stiffness of the polymer. Nevertheless, thermosetting polymers are not deformable once cross-links are established. In optical applications epoxy resins are thermosetting polymers which are frequently used for waveguide and also interlink fabrication.

Elastomers on the other side exhibit coarse-meshed chemical cross-links with intertwined macromolecules. The molecular configuration allows the polymer chains to reversibly slide with respect to each other within certain limits which leads to a rubber-like behavior. Elastomers are hardly used in optics with exception of polydimethylsiloxane (PDMS), which is transparent and used,

for instance, as flexible membrane in adaptive optical system [22] (for chemical structure of PDMS see Figure 4.11 and discussion below).

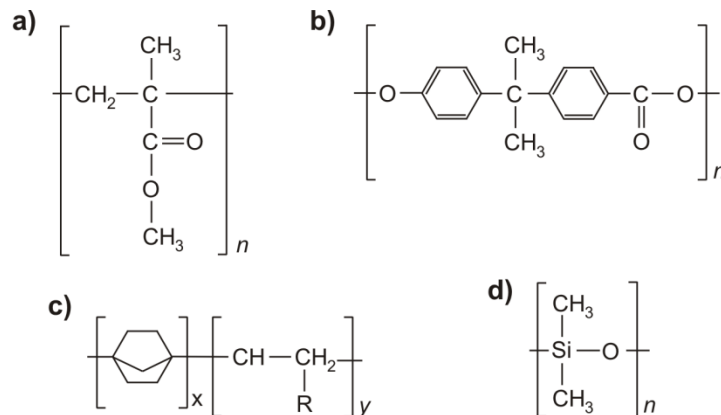


Figure 4.11: Chemical structure of various polymers: a) poly(methyl methacrylate) (PMMA); b) polycarbonate (PC); c) cyclo-olefin-copolymer Topas (COC); d) Polydimethylsiloxane (PDMS) (according to [9]).

The optical, mechanical and thermal properties of polymers are determined by the chemical structure of their monomers and, to a certain extent, the degree of polymerization which indicates the chain length of the macromolecules. In general, a higher degree of polymerization relates to a higher melting temperature and higher mechanical strength [42]. However, other properties can approximately be determined from the chemical structure, which is exemplarily shown in Figure 4.11(a) to (c) for selected polymers used in integrated optics. In optical applications, refractive index, absorption and birefringence are highly important parameters. The refractive index can be estimated by the chemical groups forming the specific monomer. For instance, to determine the refractive index n of PMMA, as shown in Figure 4.11(a), one needs to calculate the molar refraction R_{GD} according to the Gladstone and Dale model.

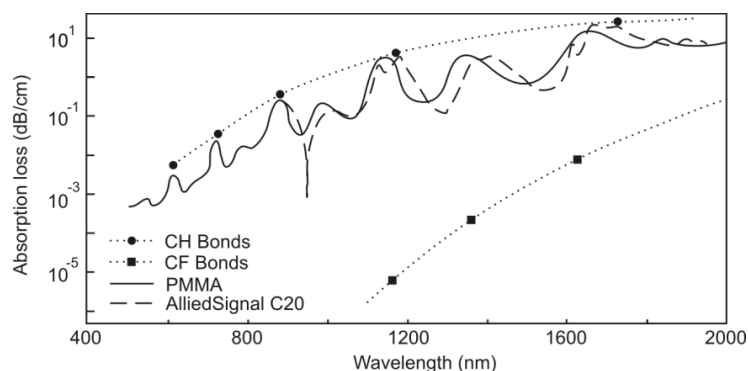


Figure 4.12: Measured absorption of PMMA and AlliedSignal C20 as function of wavelength in comparison to calculated absorption caused by CH and CF bonds (adapted from [43]).

To do so, the contributions to R_{GD} have to be summed up according to the chemical groups forming PMMA: $R_{GD} = 1(-CH_2-) + 2(-CH_3) + 1(-COO-) + 1(>C<) = 24.754 \text{ cm}^3/\text{mol}$, which was calculated according to

data presented in [44]. Together with the molar volume of PMMA $V = 86.5$ cm, Gladstone and Dale's model states that $R_{GD} = (1-n)V$ and yields $n_D = 1.485$ which is in good agreement with the experimentally obtained value $n_D = 1.49$. In comparison, polycarbonate (PC) contains aromatic rings which give a significant contribution to R_{GD} and, hence, its refractive index calculates to $n_{D,PC} = 1.6$ (see Figure 4.11(b)). Also other optical properties such as birefringence are readily determined from the chemical structure of polymers. However, this is beyond the scope of this work and we refer to [44] for a detailed discussion.

Table 4.3: Properties of selected advanced polymers/monomers [2, 10, 43, 45].

Manufacturer	Type	Patterning Technique	Attenuation (dB/cm)	Other properties
Corning (AlliedSignal)	Acrylate	Photoexposure, wet-etching, RIE, laser ablation	0.02 (at 840 nm) 0.2 (at 1300 nm) 0.5 (at 1550 nm)	Low birefringence, cross-linked, environmentally stable
	Halogenated acrylate	Photoexposure, wet-etching, RIE, laser ablation	< 0.01 (at 840 nm) 0.03 (at 1300 nm) 0.07 (at 1550 nm)	Low birefringence, cross-linked, environmentally stable
NTT	Deuterated acrylate	RIE	0.17 (at 1310 nm) 0.43 (at 1550 nm)	
	Fluorinated polyimide	RIE	TE: 0.5, TM: 0.7 (at 1550 nm)	
Dow Chemical	Perfluorocyclobutane (XU 35121)	Photoexposure, wet etching	0.25 (at 1300 nm) 0.25 (at 1500 nm)	$T_g = 400$ °C
Asahi Glass	Perfluorovinyl ether cyclopolymer (CYTOP)	s.n.	0.005 (VIS, NIR)	$n_D = 1.34$
DuPont	Tetrafluoroethylene and perfluorovinyl ether copolymer (Teflon AF)	s.n.	s.n.	$n_D = 1.31$ (AF 1600) $n_D = 1.29$ (AF 2400)
Ipitek	Poly (methyl methacrylate) with CLD-1 chromophore (PMMA-CLD-1)	RIE	5.0 (at 1300 nm)	Non-linear optical polymer

One of the most important optical properties when dealing with integrated photonics is absorption. In commonly used polymers, predominant absorption takes place due to vibrational states of molecular bonds. As can be seen in Figure 4.12 for PMMA and C20 (AlliedSignal), vibrational states of CH-bonds account for most of the absorption in the VIS to NIR. In contrast, vibrational states of CF-bonds exhibit significantly lower absorption losses and, thus, past material developments focused on fluorinated and also deuterated polymers to reduce propagation losses in optical fibers. Such polymers are commercially available from various manufactures such as NTT or Corning (later AlliedSignal), as summarized in Table 4.3.

In addition to a reduction of absorption, recent developments also include novel high performance polymers which focus on specific polymer properties, see Table 4.3. For instance, the thermoplastic XU 35121 (Dow Chemical) provides glass transition temperatures as high as 400°C and is, thus, suitable to be deployed at elevated temperatures. In applications such as biological or medical optical sensing, there exists an increasing demand in polymers with refractive indices close to that of water ($n_D = 1.3$). Such polymers are commercially available from various companies, e.g. CYTOP ($n_D = 1.34$, Asahi Glass) or Teflon AF ($n_D = 1.29...1.31$, DuPont). For optical sensing, specific optical properties are required such as a strong non-linear behavior as, e.g., provided by PMMA-CLD-1 (Ipitek). These examples are just a few and can easily be extended to polymers also exhibiting electro-optical or magneto-optical effects [2, 10].

4.4 Optical Design Methods

Designing integrated photonic devices is most often based on an optical simulation of the optical system including material properties as well as the optical layout of the photonic system. A parameter sweep is usually performed to optimize the optical system where geometric features of the layout such as waveguide diameters or material properties such as refractive indices are used as free parameters. Regardless of the specific design task, numerical simulations form the basis of such optimization procedures. Commonly used numerical methods are briefly outlined within this section, especially some of which are utilized in Section 5. In general, design methods are classified in (1) ray-optical, (2) scalar wave-optical and (3) and rigorous methods. A specific choice of the simulation method depends on the wavelength of light with respect to the feature sizes of the optical elements used for the optical layout. Typically, scalar or even ray-optical based methods are applicable if the smallest feature size of the optical exceeds approximately ten times the wavelength of the light.

4.4.1 Ray tracing

If the wave character of light can be omitted, light propagation is modeled by rays. The mathematical formulation is based on Fermat's principle which states that a light ray always propagates along the path which leads to the shortest propagation time. Hence, refractive index changes within the modeled area lead to a change in propagation direction and, in case of refractive index steps or gradients, to reflection and refraction. In general, ray propagation is described by the Eikonal equation

$$\nabla S(\mathbf{r}) = n(\mathbf{r})\hat{\mathbf{s}}, \quad (4.20)$$

where S denotes the wavefront of a ray or wave traveling inside the region of interest, $\hat{\mathbf{s}}$ is the vector normal on the wavefront at a point in space defined by \mathbf{r} with n being the refractive index distribution [17]. Equation (4.20) forms the basis of ray tracing which is often used to model and optimize multimode waveguides and optical elements such as couplers. Rays travel along rectilinear

lines inside a step index multimode waveguide, as shown in Figure 4.13(a). However, ray tracing methods are also capable of simulating light scattering at rough surfaces and in random media as long as wave effects can be neglected, also shown in Figure 4.13(a). Sidewall roughness and bulk scattering can drastically increase optical losses in waveguides and may be considered in optical simulations by ray tracing. Typically, scattering enters the simulation through a probability density function (PDF) which defines the probability that an incident ray is scattered into a certain angular direction.

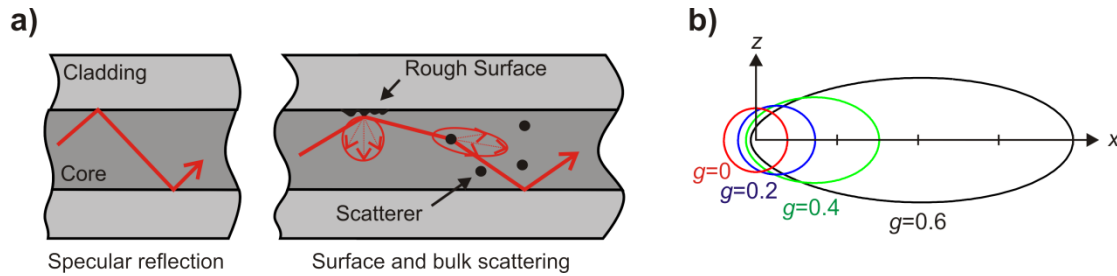


Figure 4.13: Light propagation in waveguides: a) Comparison between specular reflection and beam deviation caused by scattering on rough boundaries and bulk scattering at particles; b) Henyey-Greenstein phase function.

In ray tracing, a large number of up to several millions of rays are traced through the optical system to be modelled. Hence, ray tracing is a Monte-Carlo based simulation technique and light distributions are modelled by considering the probability that a ray travels a certain optical path. Various PDFs are utilized but most often surface scattering is considered to follow Lambert's cosine law while bulk scattering at particles is described in the framework of Mie theory [17]. However, the PDF governed by Mie theory is not easily implementable in terms of numerical simulations and an approximation referred to as Henyey-Greenstein phase function (HGPF) is frequently used, especially but not only to model light scattering in biological tissue [46]. The PDF of the HGPF reads

$$p(\theta) = \frac{1}{4\pi} \frac{1 - g^2}{[1 + g^2 - 2g \cos(\theta)]^{3/2}}, \quad (4.21)$$

where θ is the polar scattering angle and g is a free parameter determining the degree of isotropic scattering. The HGPF is displayed in Figure 4.13(b) for various values of g .

4.4.2 Rigorous Coupled-Wave Analysis

When designing integrated photonic systems, there are various scenarios where periodic structures act on the electromagnetic field. Prominent examples are grating couplers, which diffract light into a certain order due to their specific shape, depth and material selection. To model the effect of periodic structures on fields the rigorous coupled-wave analysis (RCWA) also referred to as Fourier Modal Method (FMM) is widely used. RCWA takes advantage of the periodicity of gratings and, thus, the electric and magnetic field.

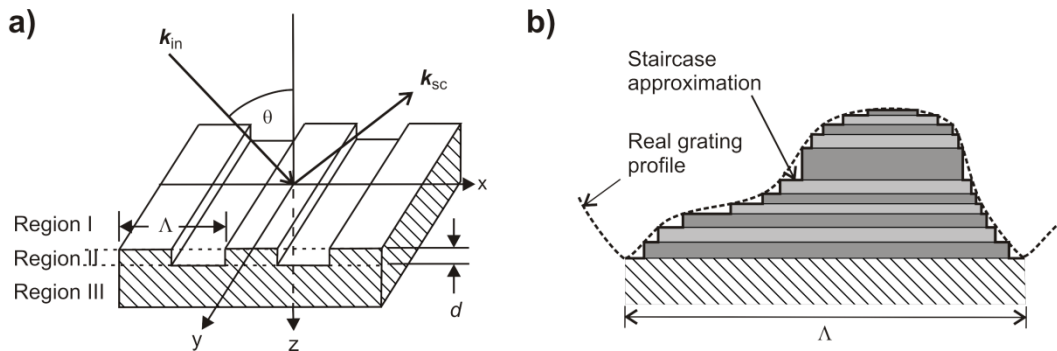


Figure 4.14: Rigorous coupled-wave analysis (RCWA): a) sketch of a binary grating considered as basic model in RCWA; b) staircase approximation used in RCWA as approximation of a continuous grating profile.

If we consider a grating as sketched in Figure 4.14(a) and an incident plane wave with the electric field \mathbf{E}_{inc} and the wave vector \mathbf{k}_{inc} impinging on the grating, transmission and reflection only takes place in discrete diffraction orders being defined by the grating period Λ and the refractive indices of the media. Accordingly, the wave vector \mathbf{k}_q of a diffracted order $q \in \mathbb{Z}$ is given by

$$\mathbf{k}_q = \mathbf{k}_{inc} + q \cdot \mathbf{K}_g, \quad (4.22)$$

where \mathbf{K}_g is the grating vector with $K = |\mathbf{K}_g| = 2\pi\Lambda^{-1}$. Taking advantage of the periodicity inside the grating region and assuming, for the sake of simplicity, that the grating varies in x -direction only, the permittivity ϵ , its inverse ϵ^{-1} (required for convergence improvement of the algorithm), the electrical field \mathbf{E} and magnetic field \mathbf{H} can be expressed as

$$\epsilon(\mathbf{r}) = \sum_{\nu=-N}^N \epsilon_{\nu} \cdot \exp[i\nu Kx] \quad \text{and} \quad \epsilon^{-1}(\mathbf{r}) = \sum_{\nu=-N}^N a_{\nu} \cdot \exp[i\nu Kx] \quad (4.23)$$

$$\mathbf{E}(\mathbf{r}) = \sum_{\nu=-N}^N [S_{x\nu}(z)\mathbf{e}_x + S_{y\nu}(z)\mathbf{e}_y + S_{z\nu}(z)\mathbf{e}_z] \cdot \exp[-i(k_{x\nu}x + k_y y)], \quad (4.24)$$

$$\mathbf{H}(\mathbf{r}) = \sum_{\nu=-N}^N [U_{x\nu}(z)\mathbf{e}_x + U_{y\nu}(z)\mathbf{e}_y + U_{z\nu}(z)\mathbf{e}_z] \cdot \exp[-i(k_{x\nu}x + k_y y)], \quad (4.25)$$

where the sums run over a fixed number $\nu = -N \dots N$ of diffraction orders which also include evanescent orders, \mathbf{e}_x , \mathbf{e}_y and \mathbf{e}_z are unit vectors point in x , y and z -direction, respectively, and $U_{x,y,z;\nu}$, $S_{x,y,z;\nu}$ and ϵ_{ν} and a_{ν} are Fourier coefficients. The truncation of the sum at N is a free simulation

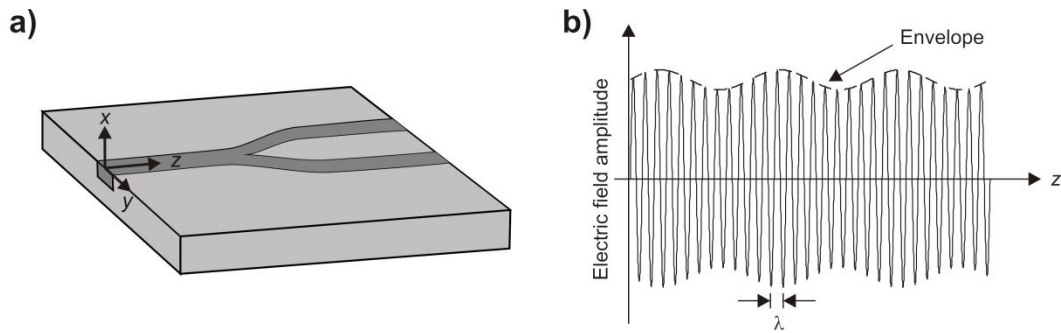


Figure 4.15: Simulation of light propagation in waveguide structures: a) Y-splitter holds as an example for an optical element suitable to be designed using BPM; b) Electric field amplitude along z -direction with a slowly varying envelope with respect to the wavelength (according to [47]).

parameter that needs to be chosen according to a given problem and strongly determines the convergence of the method. Especially, N needs to be chosen carefully if the materials involved exhibit a high complex part of the refractive index such as in the case of gold where convergence of the RCWA algorithm is a problem. To proceed further, Equations (4.23) to (4.25) are inserted into Maxwell's Equations (4.2) and (4.3) yielding a set of second order differential equations which are readily solved by eigenvalue methods, as described in detail in [48]. However, to solve these equations boundary conditions are crucial and follow from the requirement that all fields need to be continuous at the boundaries between region I, II and III, as shown in Figure 4.14(a). Note, that for binary gratings the only the dependence in z -direction enters Equations (4.23) and (4.25) in form of the Fourier coefficients. The dependence of the electromagnetic field in z -direction is calculated via boundary conditions when matching fields at the interface between different regions, e.g. between Region I, II and III in Figure 4.14(a). To be able to model gratings which exhibit continuous surface profiles using RCWA, the grating is subdivided in z -direction into layers with the same periodicity but possibly varying height d , as sketched in Figure 4.14(b) [49]. Among convergence problems, computational artifacts due to this so-called staircase approximation are limiting factors of RCWA simulations [48, 50].

4.4.3 Beam Propagation Method

When designing optical waveguides, Y-splitters or even more complex structures such as Mach-Zehnder interferometers (MZI), the beam propagation method (BPM) is the most widely used [2, 25, 47]. There exist scalar but also fully vectorial BPM variations and also different approaches to solve the governing BPM equations. However, they all have in common that in typical integrated photonic devices a distinct direction of propagation is predominant and the refractive index distribution of the device is only slowly varying in this direction. Optical structures which can be designed using BPM are, for example, Y-splitters as exemplarily shown in Figure 4.15(a). Without loss of generality, we assume the direction of propagation coincides with the z -axis. In BPM it is furthermore required that the paraxial approximation holds, which implies that the z -component of the electric field is

negligible due to small propagation angles of field with respect to the z-axis. Thus, the total field reads

$$\mathbf{E}(\mathbf{r}) = \begin{pmatrix} E_x \\ E_y \end{pmatrix} \cdot \exp[-in_r k_r z], \quad (4.26)$$

where n_r and k_r are the refractive index and wave vector of reference medium surrounding the waveguide, respectively. Another important requirement of the BPM is that the electric and magnetic fields are only slowly varying, as depicted in Figure 4.15(b). In mathematical term the corresponding condition reads

$$\left| \frac{\partial^2 E_{x,y}}{\partial z^2} \right| \ll 2n_r k_r \left| \frac{\partial E_{x,y}}{\partial z} \right|. \quad (4.27)$$

Again, using Maxwell's equations with the solution (4.26) and assume that Equation (4.27) holds, we arrive at [47]

$$2in_r k_r \frac{\partial E_{x,y}}{\partial z} = \left(\frac{\partial^2}{\partial x^2} + \frac{\partial^2}{\partial y^2} \right) E_{x,y} + \frac{\partial}{\partial x,y} \left(\frac{1}{n^2} \frac{\partial n^2}{\partial x} E_x + \frac{1}{n^2} \frac{\partial n^2}{\partial y} E_y \right) + k_r (n^2 - n_r^2) E_{x,y} \quad (4.28)$$

The subscripts x, y indicate that Equation (4.28) consists of two equations with subscripts being x or y , respectively. Equation (4.28) gives the two basic full vectorial equations which are solved using different approaches. Early solver approaches were based on Fast Fourier Transform (FFT) which were referred to as FFT-BPM [20]. Modern solvers in FD-BPM most often use finite differences (FD) methods and are capable of delivering fully vectorial solution in 3-D problems. In this case, all electric and magnetic field components are calculated in x -, y - and z - direction.

4.4.4 Other Design Methods

While BPM, RCWA and Ray tracing are simulation algorithms specifically used to simulate light or wave propagation, there exist other simulation tools which were not explicitly developed for optics but are powerful tools to solve differential equations numerically. If small features at the nano- or micrometer scale need to be designed such as ring resonators, finite difference time domain (FDTD) is frequently used [51]. It is often considered as brute force approach due to the fact that it solves Maxwell's equation directly in small time steps. However, the method requires a vast amount of computational power and is therefore limited to small simulation areas not to exceed a few cubic microns in the VIS wavelength case.

An alternative to FDTD is the Finite Element Method (FEM) which is a well-established method to solve differential equations in many disciplines such as mechanics but also electromagnetics [52]. In FEM, the simulation domain is subdivided in smaller units according to the geometry of the problem. These subdomains can exhibit different shapes ranging from rectangles and triangles in 2-D or tetrahedrons and cubes in 3-D. Inside the subdomain, the differential equations are solved

through variation approaches and boundary conditions enter into the solution at the node points. Applications are versatile and range from simulation of optical waveguides to photonic sensors such as whispering gallery mode resonators [53].

To design multimode interference (MMI) or directional couplers, the eigenmode expansion (EME) approach delivers reliable results. Here, the electromagnetic field is considered as a superposition of modes propagating in the forward and backward directions inside the optical element. Different optical elements exhibiting different optical modes or optical interfaces can be matched through boundary conditions [2].

5 Overview of Own Research Results

In this section, an overview of own research results is given which were obtained during my group leader, i.e. habilitation, research at the Hannover Centre of Optical Technologies (HOT). If not stated otherwise, the results were published in peer-reviewed journals and/or presented at international conferences and proceedings which are indicated at the beginning of each subsection. Furthermore, each subsection contains an overview of related research which was conducted by other groups in the respective research field.

5.1 Characterization of Integrated Optical Systems

5.1.1 Overview

In a first step, evaluating integrated photonic devices essentially boils down to an extensive characterization of optical waveguides as they represent basic components in integrated photonics. Presumably, the property of highest interest is optical attenuation, i.e. losses in a certain wavelength region, followed by geometrical dimensions of waveguides as well as other material properties, e.g. refractive index, dispersion or elasticity [2]. The geometry of a waveguide is typically determined by classical surface topography measurement techniques such as white light interferometry, confocal microscopy, atomic force microscopy or raster electron microscopy [54], [55], [E 17], [E 48]. However, optical measuring methods are prone to measurement artifacts, which have not been fully understood, yet. Properties of optical profilers were studied by various authors [56], [57] and it was found that the shape of a microstructure leads to measurement artifacts in certain circumstances [58]. This is a known phenomenon when considering sharp edges but has also been observed at curved microstructures in case of white light interferometry. The latter microstructures are of special interest in waveguide fabrication when dealing with printed waveguides [20], [25] and, thus, a comprehensive understanding of imaging properties and optical artefacts of optical microscopes is required. In this work, we used a mathematical model for confocal microscopy to study the influence of optical aberrations on measurement errors.

In addition to 2-D topography measurements, tomographic 3-D measurements of integrated optics provide insight into accuracy and capability of fabrication processes. Here, we applied optical coherence tomography (OCT) as 3-D measurement technique and introduce novel methods for calibration of OCT and refractive index measurements [59], [E 36], [E 39], [E 40]. Alternative methods for determining of refractive indices include reflectometry, ellipsometry, propagation-mode near-field method and refracted near-field method [2], [60]. However, reflectometry is limited to 2-D structures, ellipsometry to layered media and the mode near-field as well as the refracted near field method to linear waveguide structures which do not alter their geometry in direction of propagation [2]. In addition to the characterization of waveguides, refractive index changes introduced by optical elements such as gratings may lead to phase changes of an incident

light field [17]. Hence, characterization methods which are capable of directly measuring phase changes are of great interest. In addition, a phase retrieval method is also introduced in this section and applied to fs-laser written phase gratings [E 5].

To quantify optical loss values of waveguides, several techniques are at hand which all rely on the measurement of the optical power which is coupled into and out of the waveguide, as described in Section 4.1.3. Loss is calculated from the fraction of intensity/power which is coupled out of the waveguide at defined lengths in comparison to the intensity being coupled into the waveguide. Measuring intensities at various lengths requires either to cut the waveguide (cut-back method) or to measure stray light along the whole structure. The first method is widely used because it provides reliable and precise measurement data but, however, it leads to destruction of waveguides [2]. In this section, we introduce waveguide characterization methods utilized in this work. In addition, we present an optical-mechanical setup which was developed to characterize fabricated waveguides with respect to mechanical stability and also optical strain sensors with respect to their measurement precision [E 11].

The results presented in this section are based on publications [E 3], [E 4], [E 5], [E 11], [E 16], [E 17], [E 18], [E 24], [E 29], [E 36], [E 39], [E 40].

5.1.2 2-D Topography Measurements

In optical profiling, optical artifacts can significantly affect measurement errors. In this subsection, we focus particularly on confocal profiling and the influence of optical aberrations on measurement errors. We consider a confocal microscope imaging a sample as illustrated in Figure 5.1.

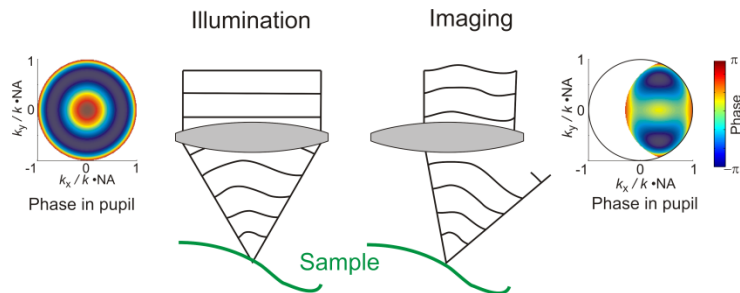


Figure 5.1: Beam path through a microscope objective with third order spherical aberration and phase distribution inside the entrance/exit pupil of the objective when illuminating and imaging a curved microstructure (from [E 18]).

If, in addition, we assume that a high NA lens of the microscope suffers from optical aberrations such as spherical aberrations, the illuminating electromagnetic field deviates from a perfectly converging spherical wave front. After being reflected from the specimen, light passes the lens again and an additional phase error is added to the field. As a consequence, light leaving the microscope lens in the imaging case deviates from a perfect plane wave (with a possible defocus term). The introduced phase error is not only dependent on the aberration of the lens but also on

the inclination angle of the sample, as shown in Figure 5.1. The resulting confocal measurement signal is strongly dependent on both and, hence, changes with the inclination angle of the sample. To investigate this effect in depth, we developed a mathematical model of a confocal microscope as sketched in Figure 5.2 (Note, the numerical model is based on initial work performed in my PhD thesis [E 48], while the obtained results are from [E 18]). The model consists of an illumination and an imaging part, where a monochromatic and circularly polarized light field is focused onto a sample with an inclination angle α .

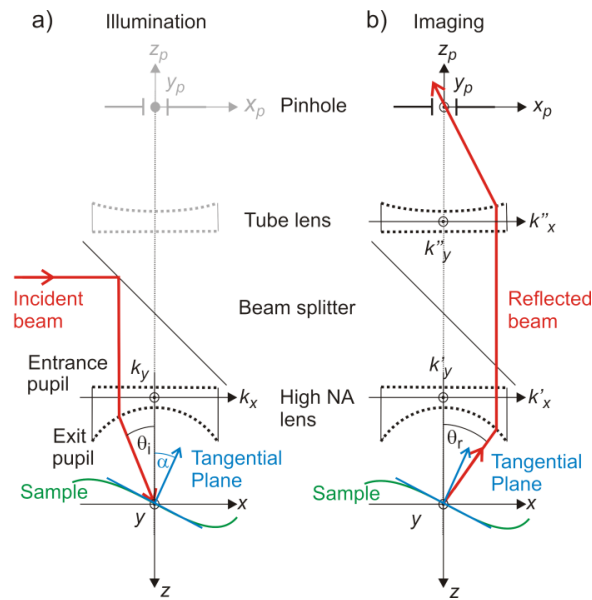


Figure 5.2: Numerical model of a reflection-type confocal microscope consisting of an illuminating (a) and an imaging optical path (b) (from [E 18]).

Focusing is achieved by utilizing a microscope lens with a high numerical aperture which is modelled according to Debye's theory [E 18]. Aberrations are introduced to the incident field by an additional phase term which consists of a series expansion of Zernike polynomials. Imaging is modeled by assuming that the reflected light passes the same objective again and is subsequently focused by a tube lens onto a pinhole detector which is assumed to be infinitesimally small. The model was used for numerical simulations to determine the influence of the surface tilt angle α and Zernike aberration on the measured confocal response. It was found that both parameters combined lead to a strongly deformed confocal intensity response curve which causes a systematic deviation Δz between the actual and measured profile height. As a consequence, inclined surfaces will be imaged at a false depth z and topography measurements on curved microstructures yield erroneous radii of these structures. A detailed mathematical description of the model is given in [E 18]. Simulation results obtained using our model are presented exemplarily in Figure 5.3 and Figure 5.4, which show the systematic deviation Δz as function of the surface tilt angle α and Zernike coefficients C_{nm} , respectively. It was found that commonly observed aberrations lead to errors of up to 200 nm, which is a significant error when performing topography measurements including feature sizes in the few micron range.

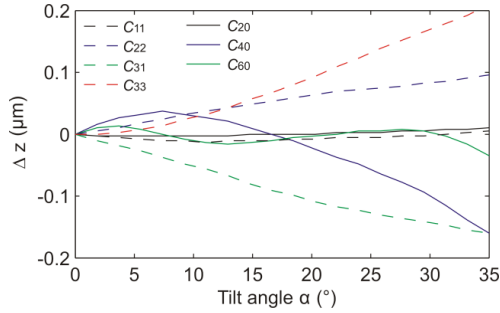


Figure 5.3: Simulated systematic error Δz as function of the inclination angle α caused by various aberrations: distortion (C_{11}), defocus (C_{20}), astigmatism (C_{22}), coma (C_{31}), trefoil (C_{33}), 3rd order spherical aberration (C_{40}) and 5th order spherical aberration (C_{60}); each aberration coefficient accounts for 0.05λ (from [E 18]).

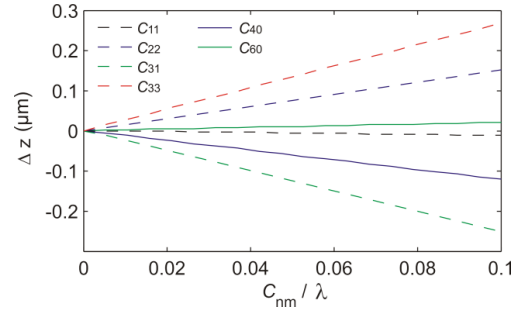


Figure 5.4: Simulated systematic error Δz as a function of various Zernike coefficients C_{nm} : distortion (C_{11}), astigmatism (C_{22}), coma (C_{31}), trefoil (C_{33}), 3rd order spherical aberration (C_{40}) and 5th order spherical aberration (C_{60}); the tilt angle is fixed to $\alpha = 25^\circ$ (from [E 18]).

Experimental in comparison to theoretical results are presented in [E 18] and support our findings. To account for the introduced measurement error, an extensive calibration of the microscope including spherical objects significantly improves the accuracy of the microscope [E 18].

5.1.3 Volumetric 3-D Measurement

Non-destructive measurements of sub-superficial features and boundary layers in integrated photonics can yield useful information on manufacturing accuracy and resulting defects without the need to destroy devices for measurement purposes.

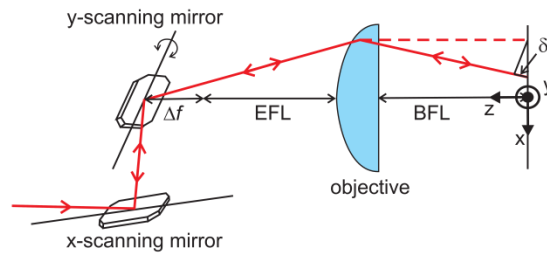


Figure 5.5: Sketch of the OCT scanning head and beam path inside the head; EFL: effective focal length, BFL: back focal length (from [E 16]).

An approach pursued in this work is to utilize optical coherence tomography (OCT) to obtain volumetric 3-D measurements of refractive index distributions. However, OCT has merely been used as quantitative measurement device but rather as imaging tool in biomedical applications [E 24], [E 28], [E 40]. Therefore, to deliver reliable data of volumetric data, a faithful calibration strategy of the OCT system is required and was developed in [E 16]. In addition, OCT suffers from optical distortions which need to be corrected as described in [E 39]. For calibration purposes, first we developed a ray optical model of the OCT scan head to identify parameters which may cause optical

artifact of the system and lead to erroneous volumetric data. The model is based on the optical layout of the OCT scan head as sketched in Figure 5.5. It was implemented using the commercially available ray tracer ZEMAX™.

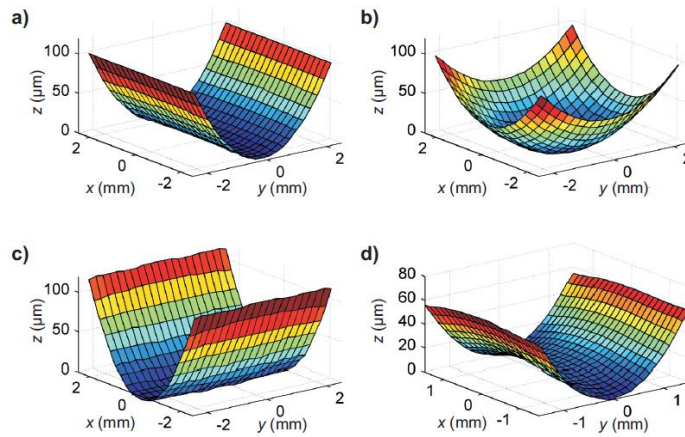


Figure 5.6: Simulated curvature-of-field: a) simulated for $\Delta f = 0$ mm; b) simulated for $\Delta f = -2.5$ mm; c) simulated for $\Delta f = -5$ mm; d) measurement (using a Thorlabs SS1300 OCT) – Δf according to Figure 5.5 (from [E 39]).

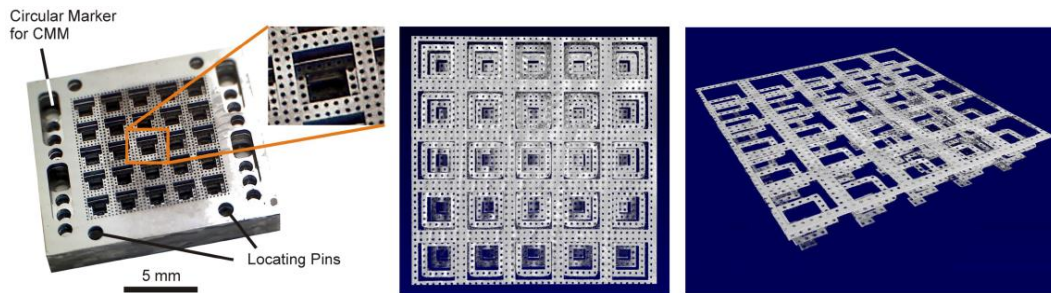


Figure 5.7: Left: Picture of the calibration standard with circular markers and locating pins, which consists of 5×5 inverse pyramidal structures with four layers. Middle/right: OCT images of the 3-D reference structure shown at different observation angles (from [E 16]).

The simulation results reveal that the position of the x- and y-scanning mirror with respect to the focal point of the OCT lens yields a significant curvature of field, as exemplarily shown in Figure 5.6. Also, if the scanning mirrors are not exactly positioned at the focal point of the OCT lens (offset denoted as Δf), the beam path in object space deviates from the ideal telecentric path (compare Figure 5.5) which leads to a volumetric distortion. To obtain calibrated OCT measurement data, we developed a novel calibration standard and procedure especially suited for OCT. The calibration standards consist of an array of inverted pyramidal structures featuring four equally spaced height levels covering a total height of 2 mm. As shown in Figure 5.7, the height levels act as support for circular landmarks with a diameter of $100 \mu\text{m}$.

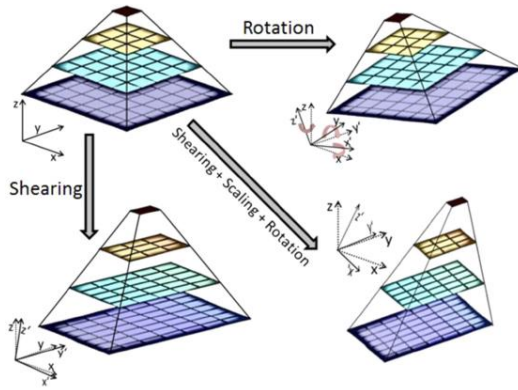


Figure 5.8: Illustration of linear transformations: rotation, scaling and shearing. The change between the original and transformed images is indicated by coordinate systems (from [E 16]).

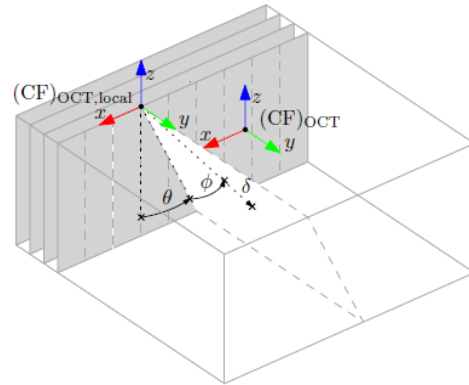


Figure 5.9: Non-linear transformation of an A-scan with respect to a local coordinate system $(CF)_{OCT; local}$. The transformation corrects the A-scans direction with angles θ and ϕ and a depth offset δ (from [E 39]).

The standard covers a total measurement volume of 10 mm x 10 mm x 2 mm. Due to the large measurement volume of the OCT, the standard was fabricated in silicon using a DRIE process. Each height level was made from single silicon chips, which were positioned under a microscope and bonded adhesively. Circular markers at the margins of the standard were used as reference markers for a coordinate measuring machine (CMM) utilized to characterize the standard after fabrication [E 16]. However, to account for the observed measurement error, a mathematical calibration model is required. The developed model takes intrinsic such as non-telecentric scanning as well as extrinsic sources of error such as misalignment of the calibration standard into account. Linear intrinsic sources of error are scaling, shearing and rotation, which can be accounted for by linear transforms, as illustrated in Figure 5.8. However, the errors being introduced by the optical design of the scanning head such as the position of scanning mirrors are of non-linear kind. To also account for such errors, the OCT calibration model corrects for an erroneous and non-telecentric beam path in object space by taking the angles θ and ϕ and a depth offset δ into account, as shown in Figure 5.9. A detailed description of the OCT calibration model is given in [E 16], [E 39] and [E 40].

To demonstrate the capability of the calibration procedure, we performed volumetric OCT measurements on the calibration standard utilizing a commercially available Fourier domain OCT system (Telesto II, Thorlabs) with an f - θ -scanning lens (LSM03, Thorlabs). Measurement results are visualized in Figure 5.7 for various observation angles. For calibration, the landmark positions were obtained from the measured data by means of a Hough transform. Subsequently, the sum of the squared differences between measured and actual landmark positions was minimized during a least-square-fit by using the OCT model parameters as free parameters of the fit which amounts to a total of 30. The calibration procedure was implemented in MatlabTM utilizing a sequential quadratic programming (SQP) optimizer to determine the optimal parameters.

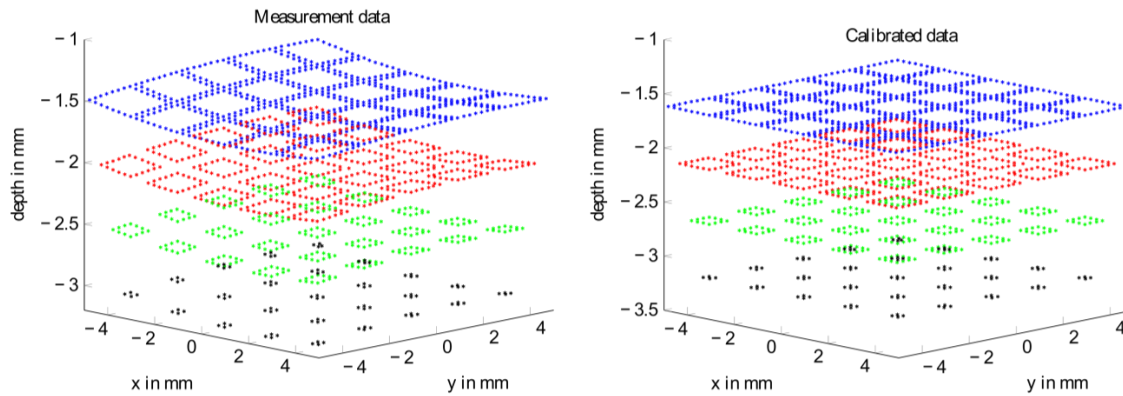


Figure 5.10: The measurement data (left) obtained by using an f-Theta OCT lens (LSM03). A transformation was calculated to best match these measurement data to the reference model data. The results (right) are nearly planar layers with a small deviation with respect to the reference model data (from [E 16]).

These parameters can be used to correct all subsequent measurement results by applying an inverse of the transform to each data set. Representative results of the calibration procedure are displayed in Figure 5.10 which shows the measured landmark positions before and after calibration.

5.1.4 Measurement of Scattering Parameters

The optical performance of waveguides does not only depend on its material and geometry but also on effects such as absorption due to scattering caused by particle inclusions or imperfections. Scattering is commonly determined by goniometric measurements where the intensity of light is measured which is scattered into a certain solid angle. Integrating over a full sphere yields the complete scattering characteristic of the sample. However, in high performance waveguides volume scattering is almost negligible but it becomes important when, for example, particles are included in waveguides or particle flow in micro-optofluidic sensor chips are to be determined [61]. Having OCT measurements at hand, they may serve as an adequate alternative to goniometric measurements. An undesired phenomenon in OCT, however, is the strong dependence of the depth signal on volume scattering but on the other hand this phenomenon can also be used to determine scattering parameters such as μ_s and absorption parameters such as μ_a of a medium [E 4]. OCT measurements rely on light with a broadband spectrum yielding a short coherence length L_c , which penetrates the medium under test. As OCT is an interferometric technique, light contributing to the measurement signal emerges from the specimen and interferes with a reference beam constructively. In time domain OCT (TD-OCT), only light with an optical path difference (OPD) between object and reference beam which lies within the coherence length L_c contributes to the OCT measurement signal. Hence, a contributing light beam may undergo several possible trajectories inside the sample exhibiting one to several scattering events as illustrated in Figure 5.11.

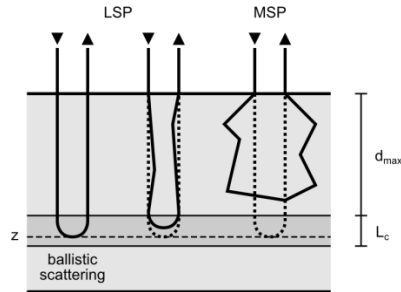


Figure 5.11: Schematic of different photon scattering orders. The left and the middle photon trajectories represent the least scattered photons (LSP), which include the ballistic case. The trajectory on the right shows an example for a multiple scattered photon (MSP) (from [E 4]).

Typically, the major part of the OCT signal arises from photons which are scattered once and are referred to as ballistic photons. The probability that a specific light ray (photon) adds to the OCT measurement signal decreases drastically with the number of scattering events it undergoes. Multiple scattered photons (MSP) hardly contribute and, hence, the signal-to-noise ratio of the signal increases with sample depth due to MSP.

An OCT depth signal also denoted as A-scan which is obtained using a sample with homogeneous refractive index as well as scattering and absorption properties exhibits an exponential decay as depicted in Figure 5.12 for OCT measurements carried out on a sample consisting of a 10% water-milk emulsion. The scattering parameter μ_s is readily determined for weakly scattering media by calculating the exponential decay parameter of the A-scan. In [E 4], we simulated the OCT depth signal by means of Monte-Carlo (MC) simulations as described briefly in Section 4.4.1. Exemplary simulation results of an OCT A-scan are also presented in Figure 5.12 for comparison and match well with the experimental data. We included scattering parameters ranging from $\mu_s = 1.35 \text{ cm}^{-1} \dots 13.5 \text{ cm}^{-1}$. The results were validated using comparative OCT measurements which were carried out using water-lipid solutions (water-milk) with concentration of 2.5 wt. % to 25 wt. %.

The actual scattering parameters μ_s of each concentration were determined from goniometric measurements (GON360, Instrument Systems), which yield a linear dependence of the measured μ_s utilizing OCT on the milk concentration as do our MC simulations. This is in contradiction with the experimental findings as can be seen in Figure 5.13. The experimentally obtained non-linear behavior results from physical effects such as dependent scattering and depolarization, which require a large amount of computational power to be simulated, and are not included in our basic MC models.

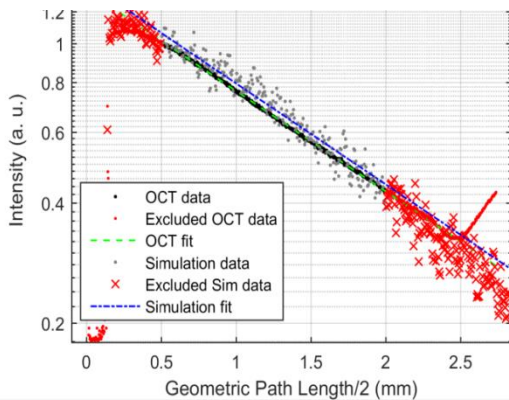


Figure 5.12: Comparison of fitted measurement (OCT data) and fitted simulation (Sim data) and their fits for a milk concentration of 10% (from [E 4]).

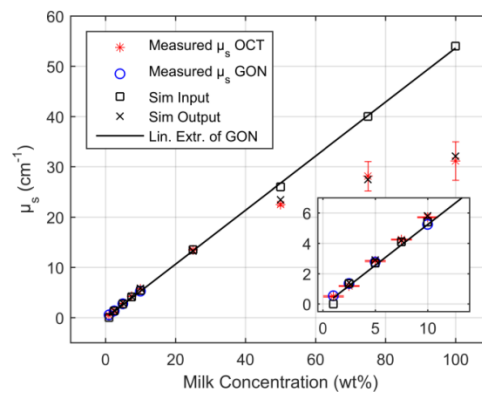


Figure 5.13: Comparison of μ_s obtained from goniometer (GON) measurements, simulation input data linearly extrapolated from these measurements (Sim input, $\mu_s LIN$), simulation results (Sim output, $\mu_s SIM$) and OCT measurements ($\mu_s OCT$). The black line is a linear extrapolation from the goniometer measurements as a guide to the eye. The inset shows a magnified part of the data for low milk concentration (from [E 4]).

To keep the numerical effort as small as possible and include the aforementioned physical effects as well, we introduced a heuristic weighting function in [E 4] which reads

$$F_W(N_{se}) = \frac{1}{1 + \exp[a \cdot (N_{se} - b)]}, \quad (5.1)$$

where N_{se} denotes the number of scattering events of a specific photon and a and b are free parameters. During each MC simulation run, each photon is weighted by F_W according to its number of scattering events N_{se} and, hence, the contribution of MSP to an OCT A-scan decreases. The parameter $a = 5$ and $b = 0.5$ were found to be the most suitable to match the experimental data assuming an anisotropy factor $g = 0.98$ which corresponds to literature values of milk. The results of our heuristic model are presented in Figure 5.13 and reproduce the non-linear behavior found in experimental data.

Hence, applying our MC model allows for determining scattering coefficients μ_s from experimental data for a large range of scattering parameters in the weak but also strong scattering regime and reproduces data obtained by more complex numerical models at far less numerical effort.

5.1.5 Refractive Index Measurements

As presented in the previous section, OCT lends itself for a high precision analysis of integrated photonic devices. However, if volumetric 3-D data are obtained, refractive index variations and boundaries lead to a distortion of OCT images due to the fact that OCT measures the optical rather than the geometrical path inside a medium. To account for this, various authors have presented

methods to correct OCT images for refractive index distortion. Most of this work is based on simulating the propagation of light rays through the medium based on Fermat’s principle and/or Snell’s law [17]. The deviation of a light ray from its initial path due to refraction and the impact of this distortion on OCT images are illustrated in Figure 5.14.

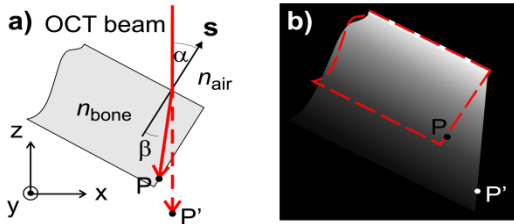


Figure 5.14: (a) OCT beam path (solid red line) inside a homogeneous and isotropic sample compared with a telecentric beam path as imaged by the OCT (dashed red line); (b) drawing of the expected B-scan and real sample dimensions (red line) (from [E 17]).

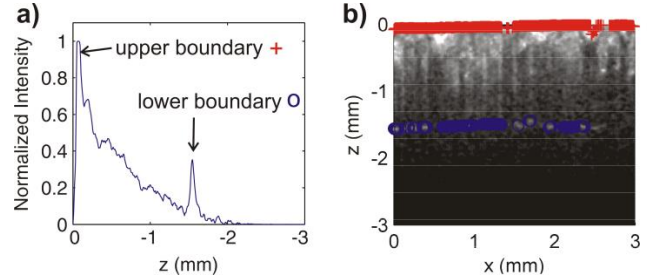


Figure 5.15: (a) Ten averaged A-scans through the porcine bone sample; (b) B-scan of the bone sample; red crosses and blue circles indicate upper and lower air-bone interfaces, respectively (from [E 17]).

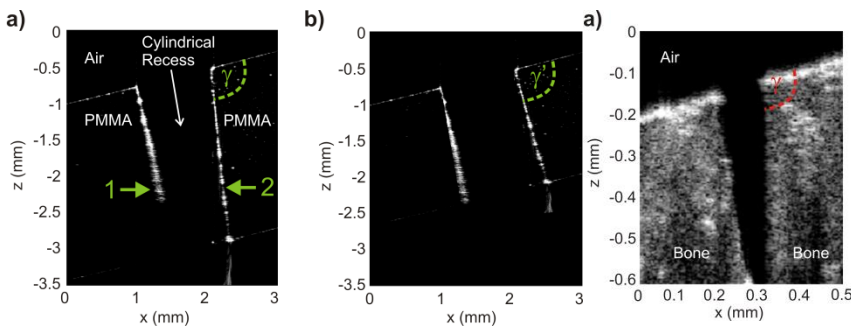


Figure 5.16: OCT B-scan through the cylindrical recess in PMMA; (a) uncorrected B-scan; (b) same B-scan corrected for a refractive index of $n=1.484$ (from [E 17]).

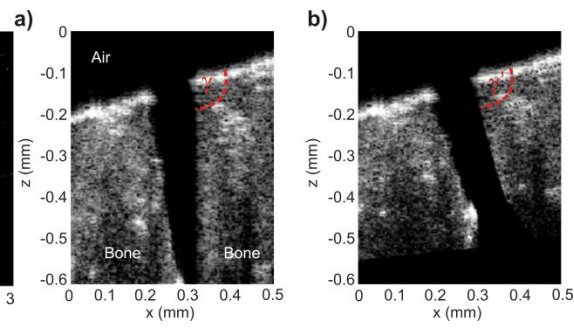


Figure 5.17: OCT B-scan through the cylindrical recess in porcine cranial bone; (a) uncorrected B-scan; (b) same B-scan after correction (from [E 17]).

Image correction requires a precise knowledge of the refractive index inside a sample to determine its actual geometry. However, the same approach can also be applied if the geometry of a sample is known but the refractive index needs to be determined, as we presented in [E 17]. This is achieved by modeling the OCT image using a ray optical approach based on Fermat’s principle assuming an initial estimated refractive index distribution. Refractive index boundaries inside the specimen change the direction of the beam path and distort OCT images. Assuming a sample with its surface gradient being inclined with respect to the optical axis of the OCT, an incident beam is deflected as obvious in the OCT image presented in Figure 5.16(a), which was obtained using a Telesto II OCT (Thorlabs). The image shows a circular recess which was drilled perpendicular to the surface of a PMMA sample. Due to refraction, the imaged flank of the recess indicated by “1” is located at its

actual position in the OCT image while the position of flank “2” in the image is erroneous. To calculate the refractive index of PMMA, we carried out a sequence of refractive index corrections of the OCT images for various refractive indices assuming an initial index of 1.5. In a next step a cylinder can be fitted to the corrected image and compared to the known geometry of the recess by means of least-square fitting, where the refractive index and the position of the recess are free fitting parameter.

The final corrected OCT image for PMMA is shown in Figure 5.16(b). In addition to technical samples, we applied the method to porcine cranial bone samples, as shown in Figure 5.17(a) and (b). The obtained refractive indices of PMMA and porcine bone are summarized in Table 5.1 and compared to reference measurements as well as literature values.

Table 5.1: Results of refractive index measurements using inverse refractive index correction (I-RIC) and comparative data obtained at a wavelength of 1300 nm (from [E 17]).

Sample material	Measured n (I-RIC)	Reference measurements of n	Literature value of n
Polymethylmethacrylate (PMMA)	1.48 ± 0.04	1.484 ± 0.004	1.476 [62] ; 1.488 [63]
Porcine cranial bone	1.52 ± 0.04	1.51 ± 0.03	1.623 [64]

Reference measurements were carried out by comparing the optical to geometrical path length determined by OCT for a sample of known thickness, as exemplarily shown in Figure 5.15.

5.1.6 Phase Measurements

The refractive index of a medium is of special interest since it influences the phase of an electromagnetic wave propagating inside the medium. As an alternative to determining the refractive index, one can also measure the introduced phase change of an electromagnetic field impinging the medium under test. This method also enables the determination of more complex phase structures such as phase gratings embedded in bulk material, as presented in [E 5].

In this subsection, we present results on the determination of phase changes by means of a phase retrieval algorithm based on the work of Farn [65]. To demonstrate the capability of the method, we measured phase changes introduced by periodic discontinuities inside a PMMA sample. The discontinuities were inscribed in PMMA utilizing a femtosecond laser writing process, as described in detail in [E 5], and exhibit a width of approximately $2 \mu\text{m}$ at a periodicity of $10 \mu\text{m}$, as shown Figure 5.18 for various pulse energies of the writing laser system. For phase measurement, a laser beam of a helium-neon (HeNe) laser was launched into the sample, which generates a far field diffraction pattern with discrete diffraction orders. The intensity diffracted into each order was measured through a power meter (S120C photodiode attached to a PM200 handheld device, Thorlabs) and serves as input parameter for the phase retrieval algorithm, which is outlined in Figure 5.19(a).

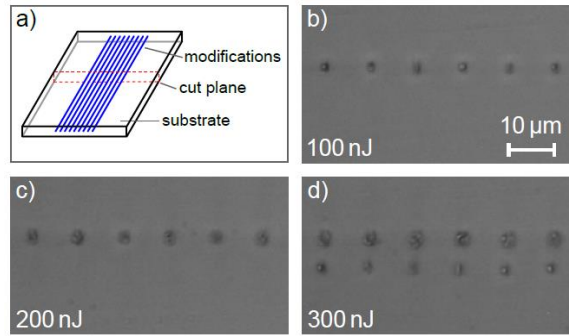


Figure 5.18: Cross sections of material modifications in PMMA: a) Schematic of the measured sectional plane. b)-d) Microscope images of written modifications using pulse energies ranging from 100 nJ to 300 nJ (from [E 5]).

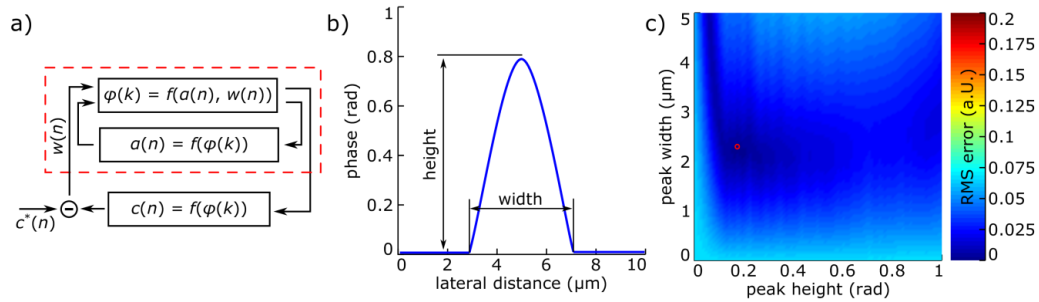


Figure 5.19: a) Sequential function chart of the phase retrieval algorithm; b) Constructed start phase function φ_0 ; c) Two-dimensional error map displaying the RMS-error between actually measured diffraction intensities and intensities as produced by the start phase function. The red dot marks the minimum RMS error (from [E 5]).

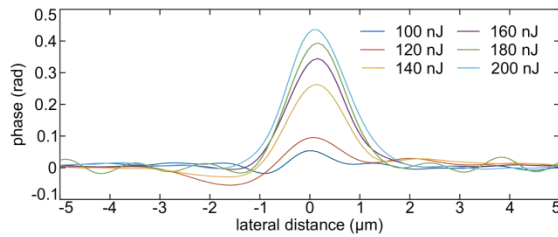


Figure 5.20: Phase given in radians over lateral distance of one grating period (from [E 5]).

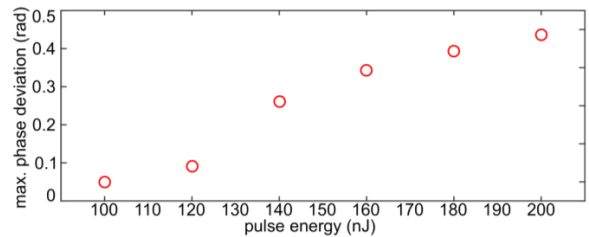


Figure 5.21: Maximum phase deviation over pulse energy. A saturation is observed at a phase value of $\max = 0.43$ rad. (from [E 5]).

An initial estimated phase distribution was utilized as starting phase φ_0 and was constructed as shown in Figure 5.19(b). Now, the algorithm carries out a parameters sweep under variation of a discrete phase $\varphi(k)$ and iteratively calculates the corresponding power which is diffracted into a certain diffraction order n . A square sum is calculated taking the measured and simulated results into account. This step is continued until the square sum reaches its minimum denoted as RMS error

in Figure 5.19(c). The phase distributions obtained for gratings fabricated using various pulse energies are presented in Figure 5.20.

5.1.7 Optical Loss Measurements

An important parameter which determines the maximal distance over which waveguides transfer data is optical loss defined as the power attenuation over waveguide length. Optical losses can be caused by various effects such as waveguide roughness, imperfections inside the waveguide and also absorption of the waveguide material as described in detail in Section 4.3. These losses can be summarized in propagation losses denoted as α and are specific to each waveguide. However, propagation losses are defined for straight waveguides. If a photonic structure contains bent waveguides, not all of the propagating modes may be confined inside the waveguide and a fraction of power leaks into the cladding of the waveguide due to a violation of the condition for TIR. The influence of this effect increases with the order of propagating modes and also the bend radius R of the waveguide. At a given bend radius R , bend losses also increase with the optical profile height Δ of the waveguide which is, again, readily explained by missing TIR.

In this work, we utilized two different setups for loss measurements at wavelengths of 650 nm and 850 nm, which are sketched in Figure 5.22. In the first setup sketched in Figure 5.22(a), we utilized a helium-neon laser (25-LHP-991) as light source. The laser beam is focused by a microscope lens (Epiplan 50x, Zeiss) with an NA=0.5 into the device under test (DUT) while the entrance facet is monitored by a CCD camera (DCC1545, Thorlabs) for convenient adjustment of the laser beam. Light at the output port of the DUT is collected at the output port of the DUT by an optical fiber with a core diameter of 50 μm which is attached to a power meter (S151S, Thorlabs). Due to the available laboratory equipment, we utilized a fiber coupled laser diode source (MCLS1-850, Thorlabs) for measuring optical losses at 850 nm, as sketched in Figure 5.22(b).

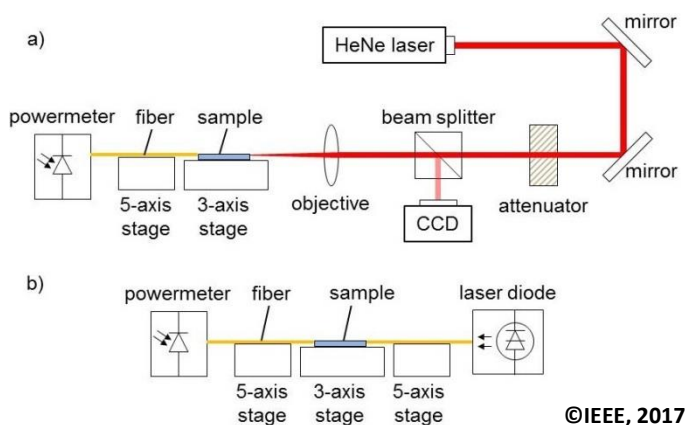
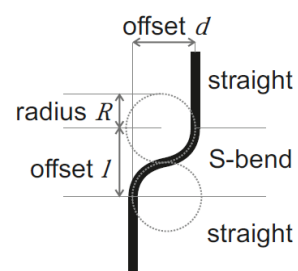


Figure 5.22: Characterization setup: (a) for $\lambda=633$ nm, (b) for $\lambda=850$ nm (from [E 3]).



©IEEE, 2017

Figure 5.23: Waveguide design for measuring bend losses (from [E 3]).

For alignment purposes, the DUT was placed on a manual three axis translation stage (Elliot Scientific) and all fibers were fixated to five axis translation stages (Elliot Scientific). Prior to all optical measurements, the end facet of the waveguides were prepared using a lab-build cleaver described in [E 11]. Loss measurements are typically carried out for different waveguide lengths. The gradient of the loss as function of the waveguide length determines the propagation loss α .

In addition to the characterization of straight waveguides, we put a special emphasis on bent structures (see Figure 5.23), as they represent the most basic components to realize highly integrated and complex PICs. Especially, the radius R_{min} at which lowest losses are observed at a particular waveguide determines the compactness of PICs to be designed. For bend loss measurements, we designed and fabricated waveguides (see Section 5.2) as sketched in Figure 5.23. The total bend loss L_{total} are given by [66], [E 3]

$$L_{total}(R) = L_{coup} + L_{bend}(R) + L_{prog}(R), \quad (5.2)$$

where L_{coup} denote coupling losses due to in and out coupling of light into and out of the sample. Pure bend losses are represented by L_{bend} . L_{prog} describes propagation losses inside the bend region. For measurement purposes, we evaluate relative losses L_{rel} within this work as described by [67, 25]

$$\begin{aligned} L_{rel}(R) &= -10 \log_{10} \left(\frac{P_{out}(R)}{P_{out}(R_{max})} \right) \\ &= a \exp \left(-\frac{R}{b} \right) + 3\alpha \left(4R \arcsin \sqrt{\frac{d}{4R}} \right) + c, \end{aligned} \quad (5.3)$$

where R_{max} denotes the largest bend radius featured by the sample design. The geometrical parameters R and d are defined according to Figure 5.23. The constant c summarizes constant contributions and a, b are free parameters used for data fitting. Note, the exponential decay term describes bend losses while the inverse sine term takes propagation losses within the bend region into account.

The theory and setups described in this section are presented to describe the measurement methodology according to [E 3]. Characterization results obtained using fabricated waveguides are presented in Section 5.2.

5.1.8 Opto-mechanical Properties

During recent years, there exists an increasing demand to monitor mechanical properties by optical means [E 9]. A prominent example is structural health monitoring where the integrity of metal or concrete structures is monitored through optical sensors such as fiber-Bragg-grating (FBG) sensors. This type of sensors was also realized not only in optical fibers but also in integrated photonic

circuits [68], [69]. To characterize optical waveguide based strain, force and displacement sensors such as presented in [E 9], we developed an opto-mechanical test setup, i.e. tensile testing machine, as shown in Figure 5.24.

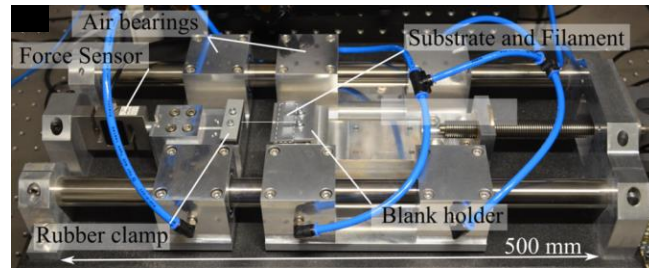


Figure 5.24: Photograph of the tensile testing machine, here with a grating under test, with laser light coupled in free-space configuration (from [E 10]).

The detailed mechanical setup is sketched in **Fehler! Verweisquelle konnte nicht gefunden werden.** The setup consists of a moving and a fixed sledge mounted on air bearings which can be positioned with respect to each other using a high precision stepper motor (Nanotec ST5909L3008-B). The sample under test can be mounted on top of both sledges as shown in Figure 5.24. To monitor forces or force as function of displacement, a force sensor (AST KAP-S/2kN) is attached to the fixed sledge. Results of force versus displacement measurements obtained during pull-out tests performed on laminated fibers are described in detail in Section 5.2.3. In general, the setup allows us to measure forces up to 2 kN starting at a minimal force of 0.1 N.

5.2 Fabrication of Integrated Polymer Optical Systems

5.2.1 Overview

Polymer based photonic integrated circuits (PICs) provide several advantages compared to their semiconductor based counterparts as they offer the potential for high throughput fabrication at low material and process costs. In addition, asset costs of fabrication technologies are significantly lower compared to wafer based technologies. However, these major advantages are somewhat counterbalanced by an increased cross-sensitivity towards environmental influences such as moisture and temperature which need to be addressed in polymer-based sensor and PIC designs [9], [2].

Depending on the specific application area and sensor design, several fabrication technologies for polymer-based optical integrated photonic devices come into question. Monolithic items have predominantly been manufactured by injection molding and hot embossing on a large-scale industrial level utilizing even reel-to-reel methods [31], [70]. Prominent examples are holograms for copy protection [E 34], [E 38], [E 47], [E 50] freeform lenses [71] or large area optics such as solar panel concentrators [72]. Also, hot embossing has already been utilized for fabrication of complex integrated photonic devices in polymers such as spectrometers [73]. Such devices often require waveguides which can be fabricated by embossing a trench structure into a polymer substrate acting as waveguide cladding. Trenches are filled either with thermal or UV curing resins which serve as waveguide cores [14], [74], [75], [E 7], [E 25], [E 26]. A fundamental parameter in waveguide fabrication is optical loss as function of waveguide length. Typical losses in hot embossed waveguides are in the range of 0.8 dB/cm for thermosetting [74], 0.2 dB/cm [75] and 1 dB/cm [76] for UV curing resins and were obtained at wavelengths of 1550 nm, 850 nm and 633 nm, respectively. Especially in waveguide fabrication, recent trends are leading towards waveguide arrays integrated in thin and flexible substrates which are fabricated with high throughput manufacturing techniques [77]. Especially continuous reel-to-reel processes are in the focus of many research groups and have successfully been developed for micro-structured optical thin foils [78] and also integrated slab waveguides [76]. Various materials have been used as core materials on hot embossed substrates including various epoxy-based and also hybrid polymer-based materials [74], [79], [80], [81], [E 3], [E 7], [E 11], [E 25], [E 26], [E 31].

Alternative high throughput methods for polymer-based waveguide and integrated photonics fabrication include printing technologies such as inkjet and offset printing [82], [83], [84]. Printing has already been applied to fabricate rare-earth doped ($\text{Er}^{3+}, \text{Yb}^{3+}$) polymer waveguides which act as optical amplifiers [85]. Another technique to directly structure waveguides and integrated photonic elements into polymers is direct UV laser writing in which refractive index changes are introduced in the bulk polymer through UV radiation. Such methods were applied to create optical structures simultaneously utilizing lithographic masks which contain the optical structures to be transferred but also single point processing were used [86], [87]. UV writing was developed using continuous

wave (cw) lasers such as argon-ion lasers for fabricating waveguides but also splitters and sensing elements such as Bragg gratings [86]. The latest research also focuses on infrared (IR) femtosecond laser written waveguides, which was demonstrated in fused silica [88] and was recently transferred to polymers such as PMMA [12]. Propagation losses of 0.52 dB/cm and 0.35 dB/cm at wavelength of 660 nm and 850 nm were reported, respectively [12].

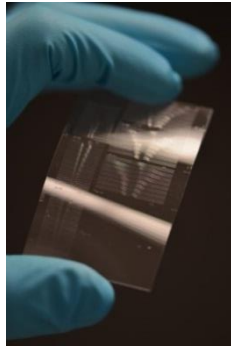


Figure 5.25: Photograph of a hot embossed waveguide substrate made from PMMA.



Figure 5.26: Microscope image of a PDMS soft stamp for waveguide fabrication.

The fabrication methods described so far directly modify fully polymerized plastics. However, a frequently used alternative is to selectively polymerize a liquid monomer resin to obtain optical elements. These processes also include lithographical techniques, in which a lithographical mask is transferred into the resin yielding wave guiding structures and even more complex optical elements such as arrayed waveguide gratings [13]. To avoid lithographic masks, many researchers have opted for spatial light modulators (SLM) such as liquid crystal display (LCD) or digital mirror devices (DMD) to omit cost intense lithographic masks [89], [E 19], [E 20], [E 30]. This technique has already been used to fabricate micro lens-arrays [90] but also waveguides and beam splitters [E 8], [E 23]. In Section 5.1.2 to 5.1.8, a short summary of our own research in the field of fabrication methods and fabrication of optical waveguide structures based on lamination, hot embossing and maskless lithography is given and optical characterization results are provided to demonstrate the capability of our methods.

Results presented in this section are based on publications [E 3], [E 6], [E 7], [E 8], [E 10], [E 11], [E 12], [E 19], [E 20], [E 21], [E 23], [E 25], [E 26], [E 27], [E 30], [E 31], [E 33], [E 34], [E 35], [E 38], [E 50].

5.2.2 Hot embossing

Processes, Tools and Experimental Apparatus

Waveguide fabrication using hot embossing starts by transferring a trench structure into polymer substrates as shown in Figure 5.25. The hot embossing process is described in detail in Section 4.2.2 and, therefore, we restrict ourselves to a description of waveguide fabrication only. Hot embossing

was performed on a commercial hot embossing machine (HEX 03, Jenoptik) as well as on a lab-made hot embossing machine comprising a manual force unit as described in detail in [E 30].

As hot embossing stamp, various stamp materials were utilized in this work including silicon (Si), polydimethylsiloxane (PDMS), polyimide (PI) andOrmocore hybrid polymer [E 4], [E 6], [E 8], [E 20], [E 21], [E 23]. The silicon stamps were fabricated utilizing the deep reactive ion etching (DRIE) process introduced in Section 4.2.2. Since DRIE is prone to a remaining waviness on sidewalls, an O₂-plasma etching treatment was applied to remove the waviness which is required to minimize propagation losses of the fabricated waveguides.

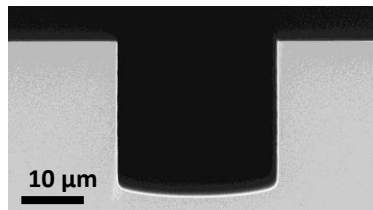


Figure 5.27: SEM image of a cross section of a silicon waveguide stamp.

Our work so far focused on the fabrication of multimode waveguides with rectangular cross sections with a height and width of 25 μm x 25 μm, see for example [E 4]. However, the method is easily transferrable to the fabrication of singlemode waveguides. An SEM image of a rectangular cross section fabricated in silicon is exemplarily shown in Figure 5.27.

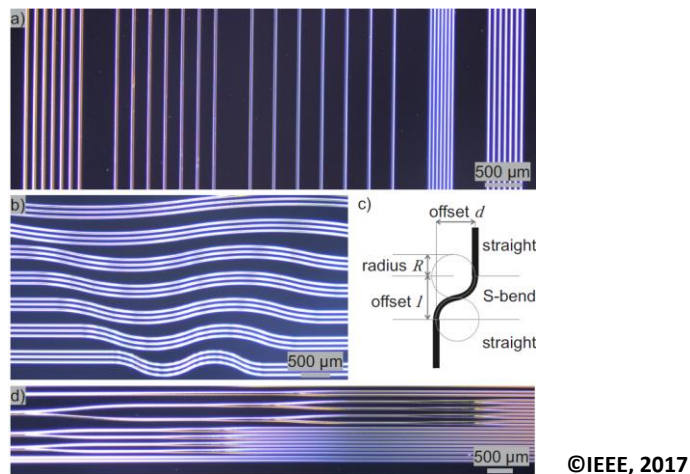


Figure 5.28: Structures included in the silicon-based embossing stamp: (a) Micrograph of straight waveguide structures with different spacings, (b) micrograph of bent structures having different radii R and a bend offset d of 0.5 mm, (c) schematic representation of the used S-curve bends (d) and micrograph of structures for the replication of beam splitters (from [E 4]).

To fully evaluate optical properties of the fabricated waveguides, we included test structures in this study as can be seen on the microscope images of the surface of the silicon stamp shown in Figure

5.28. These test structures consist of straight waveguides, bent waveguides with radii (see Figure 5.28(c)) ranging from $R = 2 \dots 20$ mm as well as waveguide arrays with spacings ranging from $25 \dots 400 \mu\text{m}$ to measure propagation and radial losses as well as crosstalk between adjacent waveguides, respectively.

However, silicon is an extraordinary brittle material and, therefore, easy to damage during the hot embossing process. In addition, polymers tend to stick to the silicon stamp during demolding which may also result in an irreversible damage of the stamp. Sticking was significantly reduced in this work by using silane monolayer coatings which were evaporated onto the micro-structured surface of the stamp by placing the silicon wafer inside a desiccator together with liquid silane. In addition, to avoid the aforementioned drawbacks, we also performed hot embossing runs using PDMS as stamp material [E 19], [E 20], [E 30]. The stamp was fabricated by coating a structured silicon wafer with liquid PDMS. The PDMS layer was cured inside a desiccator and removed manually after curing. A fabricated PDMS stamp is exemplarily shown in Figure 5.26. However, since PDMS is a flexible material, it tends to geometrical deformation during hot embossing which is undesirable if the shape of the microstructures to be embossed is of great importance.

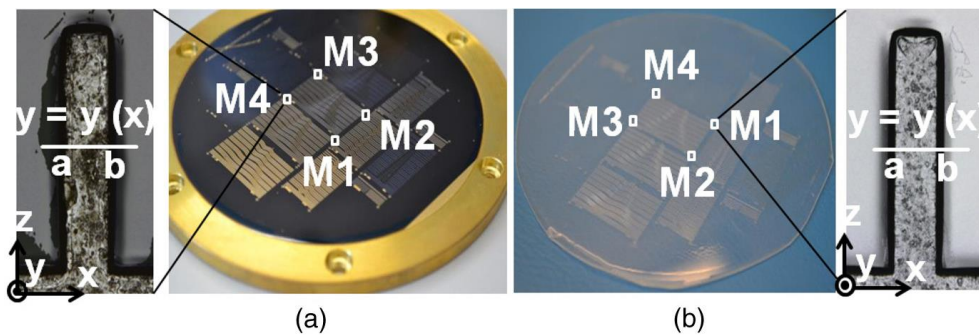


Figure 5.29: Measurement locations (M1, M2, M2 and M4) on (a) 4 inch embossing stamp (ST) and (b) 4 inch embossed poly(methyl methacrylate) films (PM) and micrographs of the corresponding patterns. $y = y(x)$ denotes the location of the extracted two-dimensional profiles from the scanned patterns (from [E 6]).

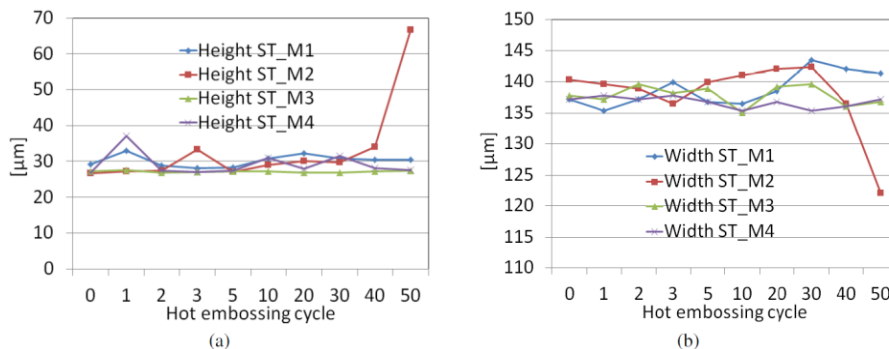


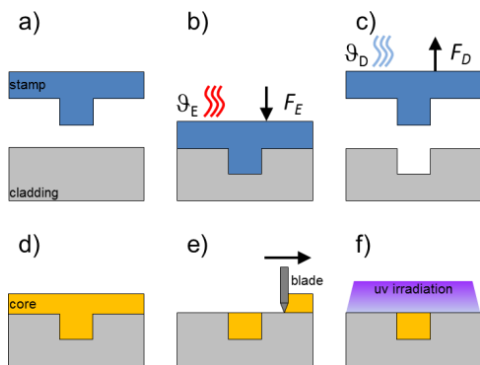
Figure 5.30: Evolution of height (a) and width (b) of stamp micro-patterns at four measurement locations (M1, M2, M3, M4) over 50 embossing cycles (from [E 6]).

Utilizing silicon wafers, or even a negative PDMS copy as hot embossing stamp, requires cost-intensive structuring of master stamps as described in detail in Section 4.2. This is especially a drawback when small series are to be fabricated. Therefore, we introduced a novel process in [E 6] which relies on structuring polyimide (PI) coated onto a silicon wafer and which was achieved by means of photolithography. The process is superior compared to purely silicon based methods described previously since it does not require etching methods. In addition, it can easily be combined with maskless lithography as described in Section 5.2.4 to even further increase its flexibility.

Figure 5.29(a) shows an image of a 4 inch silicon wafer including PI waveguide structures. The stamp was placed on a stamp inset of a commercial hot embossing machine (HEX 03, Jenoptik) which served as embossing tool holder. Figure 5.29(b) shows a replicated PMMA substrate containing trenches for waveguide fabrication. Since PI is a polymer material itself, the question arises whether it provides an adequate tool lifetime and tool wear compared to other stamp materials. Therefore, we carried out 50 embossing cycles in PMMA using the tool depicted in Figure 5.29(a). To determine tool wear, we performed confocal surface topography measurements on the replicated PMMA sample at the positions indicate by “a” and “b” in the enlargements in Figure 5.29. Results are exemplarily shown in Figure 5.30. As discussed in detail in [E 6], no significant wear was observable after 50 cycles except at location M2 which showed peel off effects mainly due to manual demolding.

Waveguide fabrication and characterization

To fabricate waveguides from hot embossed substrates, we pursued the two general concepts illustrated in Figure 5.31 and Figure 5.32.



© IEEE, 2015

Figure 5.31: Schematic of the waveguide fabrication process: (a) Heating, (b) embossing, (c) cooling and demolding, (d) material deposition, (e) doctor blading, (f) UV curing (from [E 3]).

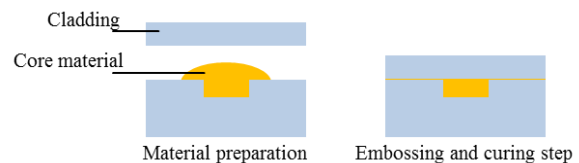


Figure 5.32: The main steps of the hot embossing of planar optical waveguides: After deposition of the liquid core material, a force is applied on the cladding layers. The sample is then heated to the curing temperature of the core material and the pressing force is released after the curing time (from [E 21]).

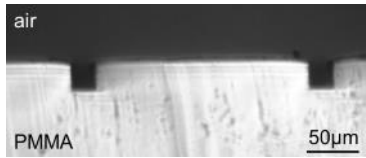


Figure 5.33: Cross section of a fabricated PMMA cladding using a silicon stamp.

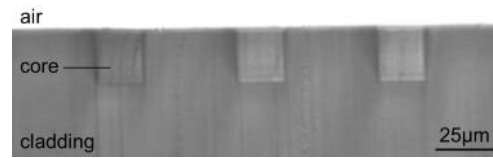


Figure 5.34: Cross section of a fabricated waveguide array using doctor blading (Core material: NOA68).

Both processes rely on an initial hot embossing step, see Figure 5.31(a)-(c), to create trenches in polymer substrates made from PMMA, PC and COC as shown in Figure 5.33. To create waveguides, the trenches need to be filled with liquid core materials which are cured thermally or by UV exposure. Optical losses and crosstalk between adjacent waveguides are prevented by reducing the thickness of a remaining residual layer on top of the waveguide well below a few 100 nm. This was achieved by a doctor blading process or by distributing the liquid core material manually, applying a second upper cladding and by performing the curing process under constant and well defined pressure. Core materials which were utilized for waveguide fabrication are summarized in Table 5.2. A cross section of a fabricated waveguide is exemplarily shown in Figure 5.34.

Table 5.2: Polymer materials utilized for waveguide fabrication (partially from [E 3], [E 7], [E 21]).

Polymer	Curing Method	Usage	Refractive Index (n_D)	Manufacturer
PMMA	-	Cladding	1.491	ThyssenKrupp
SB40	thermal	Core	1.555	PlanOS
Epo-Tek 301	UV	Core	1.519	Epoxy Technology
Epo-Tek 310-M2	UV	Core	1.4947	Epoxy Technology
OG142	UV	Core	1.568	Epoxy Technology
OG198-54	UV	Core	1.524	Epoxy Technology
NOA68	UV	Core	1.525	Norland
Supraflex	UV	Core	1.514	J+S Druckfarben
EP601	thermal	Core	1.5645	Polytec
EP610	thermal	Core	n.a.	Polytec

After fabrication, the waveguides were characterized with respect to refractive index distribution, propagation and bend losses according to the methods described in detail in Section 5.1. Results of measured refractive index distributions, propagation as well as bend losses are exemplarily shown in Figure 5.35, Figure 5.36, and Figure 5.37, respectively. The lowest obtained propagation losses are summarized in Table 5.3. The smallest substrate thickness utilized for waveguide fabrication was 50 μm .

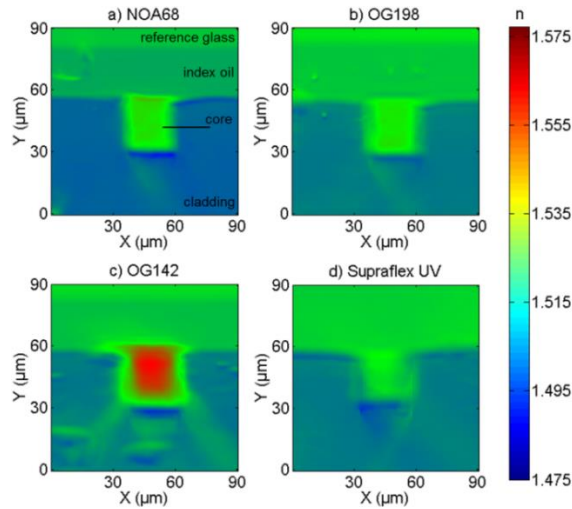


Figure 5.35: Measured refractive index distributions of cross sections of fabricated waveguides using PMMA as substrate material and different core polymers: a) NOA68; b) OG198; c) OG142; d) Supraflex (according to [E 3]).

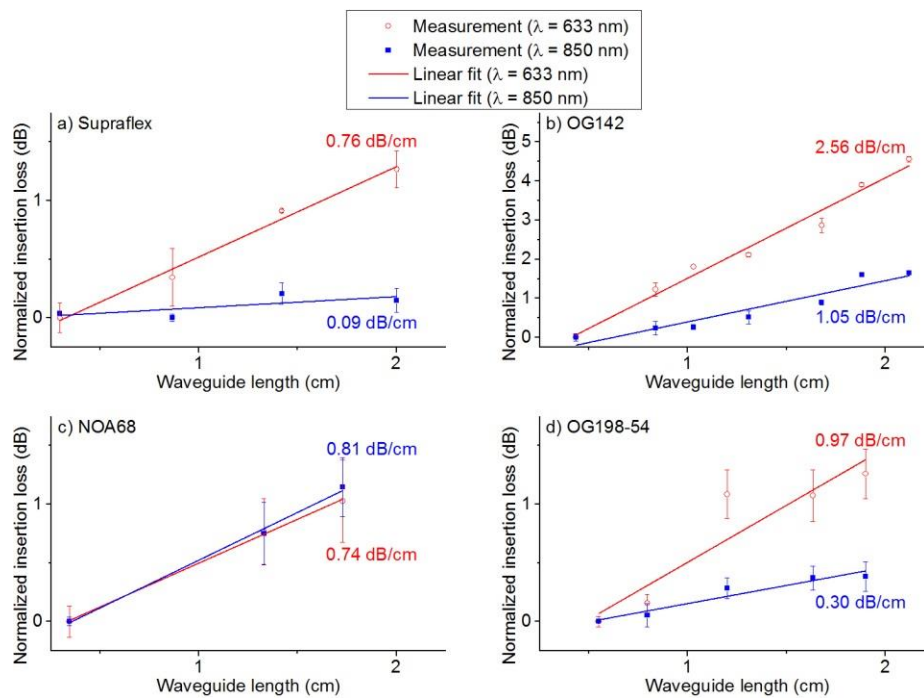


Figure 5.36: Normalized insertion losses of the waveguides as a function of waveguide length for the investigated materials and their corresponding propagation losses: (a) Supraflex, (b) OG142, (c) NOA68, (d) OG198-54 (according to [E 3]).

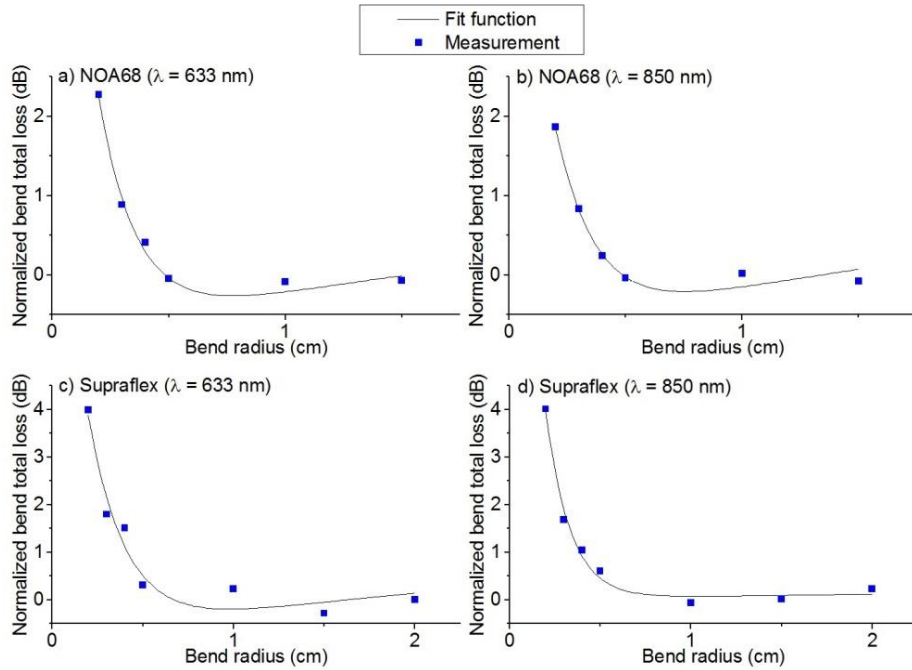


Figure 5.37: Normalized total bend losses as a function of the bend radius: (a) for NOA68 at a wavelength of 633 nm (b) for NOA68 at a wavelength of 850 nm, (c) for Supraflex at a wavelength of 633 nm (d) for Supraflex at a wavelength of 850 nm (according to [E 3]).

Table 5.3: Results of propagation loss and refractive index measurements for various core materials and wavelengths

Core material	Loss in dB/cm ($\lambda = 633$ nm)	Loss in dB/cm ($\lambda = 850$ nm)	Refractive index ($\lambda = 638$ nm)
OG142	2.56	1.05	1.568
OG198-54	0.97	0.30	1.524
NOA68	0.74	0.81	1.525
Supraflex	0.76	0.09	1.514

When using waveguide arrays, another important aspect concerns the amount of optical power which leaks from one waveguide to another and essentially determines data crosstalk between single waveguides. Crosstalk is commonly caused by evanescent fields which encompass the core of the waveguide and generate a propagating mode inside adjacent waveguides. This is dependent on the refractive index as well as the spacing between single waveguides and wavelength of the propagating light. However, also waveguide imperfections causing scattering and remaining residual layers may cause crosstalk. Exemplary results on crosstalk measurements as function of distance between adjacent waveguides are shown in Figure 5.38 for a PMMA substrate and NOA68 as well as Supraflex which serve as core materials, respectively. The results show that even at a separation distance of 25 μm between adjacent waveguides, the measured crosstalk values were as low as 30 dB.

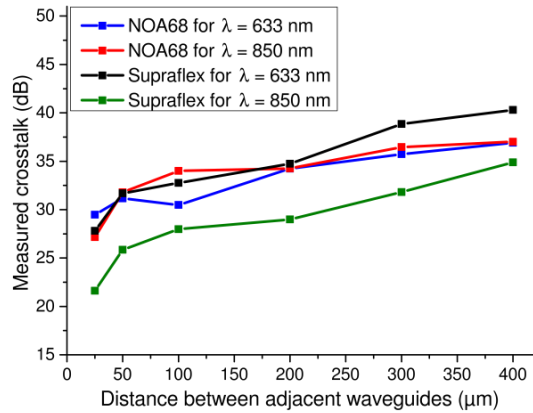


Figure 5.38: Measured crosstalk of a 20 mm long sample for the core materials Supraflex and NOA68 at the wavelengths of 633 nm and 850 nm as a function of the distance between adjacent waveguides (from [E 3]).

Multi-layer waveguide arrays

So far, only waveguide arrays were discussed which include waveguides aligned in parallel in two-dimensions. In many telecommunication and sensing applications, multi-level waveguide arrays are desirable to either enhance data transmission or to allow for multidirectional sensing. An example of such a sensor design is sketched in Figure 5.39 (for details see [E 7]).

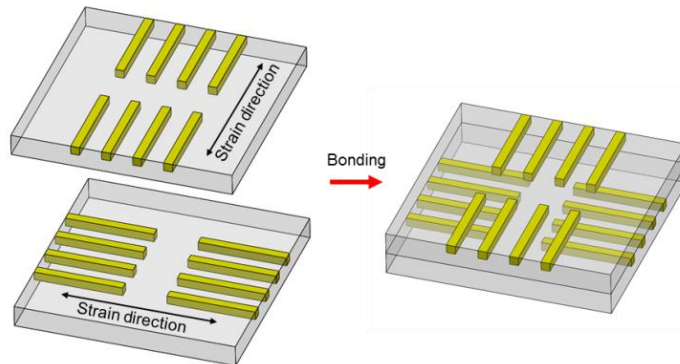


Figure 5.39: Multilayer configuration enabling 2-D strain sensing using orthogonal 1-D strain sensors: Arrows designate the strain direction that can be measured (from [E 7]).

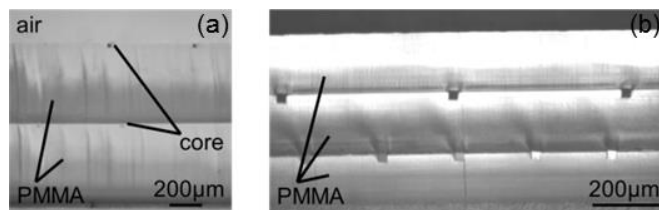


Figure 5.40: Cross section of multilayer waveguides fabricated through thermal bonding: (a) Multilayer with capped waveguide cores; (b) Multilayer with exposed top layer (from [E 7]).

For fabrication of such multi-level structures, we created two-dimensional waveguide arrays which were positioned manually under a microscope and linked through a thermal bonding process in a hot embossing machine [E 7]. Microscope images of cross sections of two-layer waveguide arrays are shown in Figure 5.40.

5.2.3 Reaction lamination

Waveguide fabrication methods discussed so far were characterized by liquid monomers which are inserted into a hot embossed trench structure and cured subsequently. Essentially, these processes are easily transferable to reel-to-reel processes and suitable for mass and high-throughput production. However, a novel approach was introduced in [E 10] which is based on a lamination technique and takes advantage of pre-fabricated and commercially available filaments exhibiting circular cross sections. To obtain waveguides, a COP filament is laminated into two PMMA sheets. Since the refractive index of COP is 1.53 and that of PMMA 1.49, both materials lend themselves for wave guiding. However, from the chemical point of view, these materials are incompatible and do not form rigid mechanical links during lamination resulting in a delamination of core and cladding under thermal or mechanical load. Nevertheless, to benefit from the excellent optical properties of both materials, we developed a process which utilizes a chemical reaction agent based on PMMA copolymers containing photoreactive 2-acryloyloxyanthraquinone (PMMA-co-AOAQ) repeat units. The reactant was developed at IMTEK (Albert-Ludwigs-Universität Freiburg, Germany), see [91].

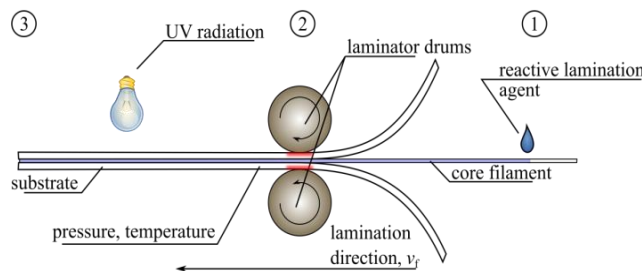


Figure 5.41: Schematic of the (1) coating, (2) lamination, and (3) irradiation processes (from [E 10]).

Table 5.4: Measured attenuation at $\lambda=625$ nm of laminated waveguides for different substrate materials and different lamination temperatures (from [E 10]).

Sub- and superstrate material	Att. w/o coating	Att. w coating
PMMA 66524 GT, $T_L = 145$ °C	2.8634 dB/cm	1.765 dB/cm
PMMA 0F058, $T_L = 145$ °C	2.3905 dB/cm	2.399 dB/cm
PMMA 0F058, $T_L = 165$ °C	3.054 dB/cm	2.253 dB/cm

The developed lamination process is illustrated in Figure 5.41 and consists of a three consecutive steps: (1) applying the reactive lamination agent, (2) lamination of the COP core filament (Zeonex 480R) between top and bottom PMMA foils serving as cladding (materials see Table 5.4), and (3) a final UV exposure to establish the chemical interlinks. A key feature of the process is that lamination takes place at a temperature T_L which is close to the glass transition temperature of the Zeonex core

filament of $T_g = 138^\circ\text{C}$. Since the PMMA materials utilized as cladding materials during the experiments exhibit a T_g ranging from 105°C to 113°C , they are deformed during the lamination process while the COP core filament retains its initial cylindrical shape due to its higher T_g .

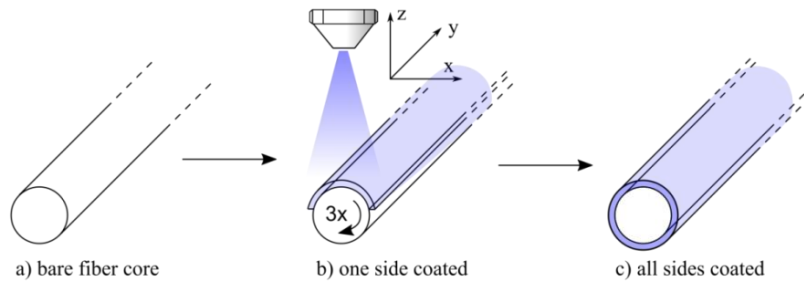


Figure 5.42: Schematic view of the coating process; a) bare fiber fixed in acrylic frame (not shown), b) coating from one side by moving the airbrush along the filament's length, c) after three rotations, the filament is uniformly coated from all sides (from [E 10]).

To completely link the core filament to the PMMA cladding, the filament was coated with reactive agent utilizing a Walter Pilot® Signier airbrush as illustrated in Figure 5.42. Lamination runs were carried out on an Ozatec hot roll laminator (HRL) 350 HRL as described in detail in [E 10]. After fabrication, waveguides were characterized in terms of propagation losses using the cut-back method introduced in Section 5.1.7 and mechanical stability by performing pull out test using the lab-build tensile testing machine presented in Section 5.1.8. Results of loss measurements are summarized in Table 5.4 and are as low as 1.765 dB/cm ($\lambda=625\text{ nm}$). The results indicate that the optical attenuation is not increased when using the reactive lamination agent. In fact, optical losses are, in average, even slightly lower compared to the case without reactive lamination agent as obvious from Table 5.4. This effect is due to a smoothing of the core's surface caused by the agent.

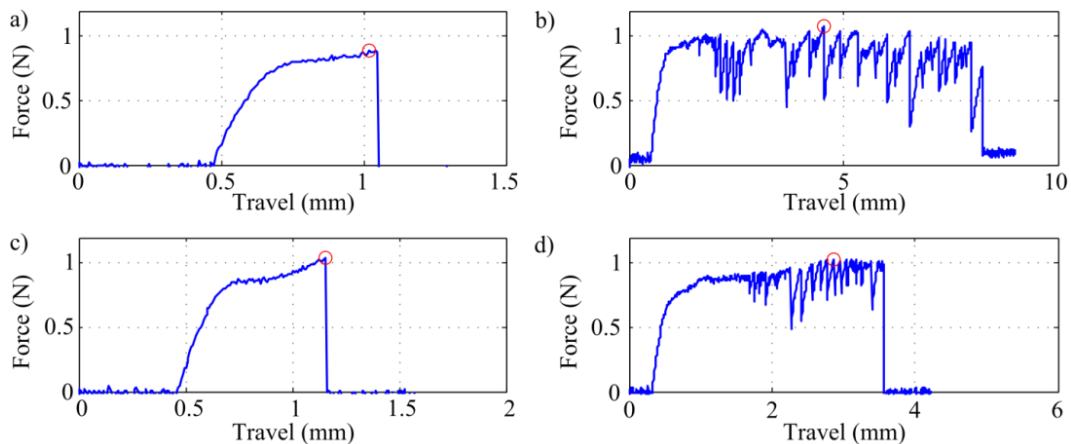


Figure 5.43: Force over travel for a) coated and b) uncoated filament with substrate material PMMA 0F058. Force over travel for c) coated and d) uncoated filament, substrate material is PMMA 99524 GT. The red circle marks the maximum force (from [E 10]).

Results of pull-out test are exemplarily presented in Figure 5.43. The force progression as function of travel of the tensile testing machine reveals that when using a reactive lamination agent (see Figure 5.43(a) and (c)), the force increases continuously due to rigid links between core and cladding until a certain maximal force is reached and linkage failure occurs. In contrast, the force versus travel curve determined for waveguides fabricated without lamination agent (see Figure 5.43(b) and (d)) exhibits discrete spikes being caused by a slippage of the core filament inside the cladding due to missing mechanical links. Hence, our method enables for the first time to our knowledge fabrication of low-loss optical components made from chemically incompatible polymers.

5.2.4 Maskless lithography

Most hot embossing methods for photonic fabrication presented so far in this work are based on a cost-intensive process step for hot embossing master fabrication using lithography or ultraprecision tooling for direct structuring of stamp materials. However, small series production as well as research and development applications would benefit from a reduction of master stamp fabrication to reduce stamp costs as well as stamp fabrication time. An approach which provides a flexible and fast manufacturing of components is maskless lithography. Here, chrome mask which are commonly utilized in lithographic process are replaced by spatial light modulators (SLMs).

Experimental setups

To fabricate microstructures and optical elements, we build two different maskless lithography setups which are illustrated in Figure 5.44 and Figure 5.45. Both setups are described and compared in detail [E 19].

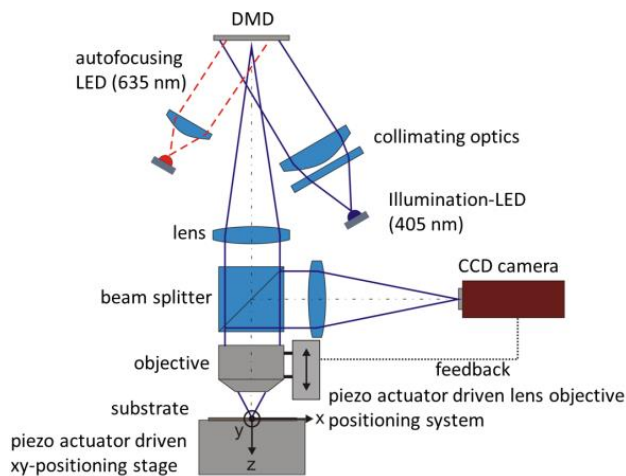


Figure 5.44: Maskless lithography setup based on a DMD (from [E 12]).

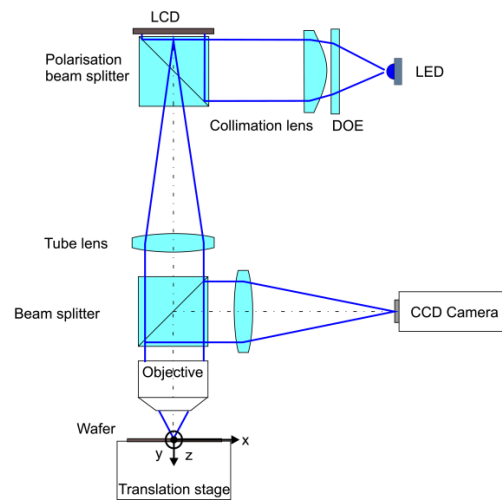


Figure 5.45: Maskless lithographic setup based on an LCD (from [E 19]).

The setup from Figure 5.44 is based on a digital micromirror device (DMD) where small micromirrors with a pixel pitch of $13,8 \mu\text{m}$ can be switched between two discrete inclination angles.

The DMD (Vialux ALP 4.1) consists of 1024 x 768 discrete pixels, i.e. micromirrors, which can be addressed individually by a personal computer. It is attached to a microscope setup consisting of a tube lens (Carl Zeiss) and planapochromate microscope objective (Epiplan 10x, Carl Zeiss). The objective is mounted on a vertical piezoelectric driven translation stage (SLC-1780-S, Smaract) to automatically find the optimal focal position. The autofocus relies on an optical feedback which is achieved by a CCD camera (Pike F421, Stemmer Imaging GmbH). The DMD image is demagnified by the microscope and imaged onto a substrate which is placed on a xy-translation stage (two SLC-1780-S linear axis, Smaract) and allows to perform a stitching process, thus, enhancing the maximal structurable area to a size of 50 x 50 mm². Two different LED light sources were utilized in the setup: the first LED runs at a wavelength of $\lambda = 405$ nm for exposure purposes and the second at a wavelength of $\lambda = 635$ nm for autofocus. The latter is achieved by projecting a specific autofocus pattern such as a checkboard pattern onto the substrate and calculating the focus value F from the recorded CCD image. In [E 12], we utilized various autofocus algorithms to calculate F such as Brenner gradient, Vollath-F4, Variance and FFT based algorithms. In addition, several focus patterns, e.g. checkboard like structures as well as images including horizontal and vertical lines at various spatial frequencies, were analyzed in terms of focusing accuracy. The best focal position was determined by finding the maximum of F .

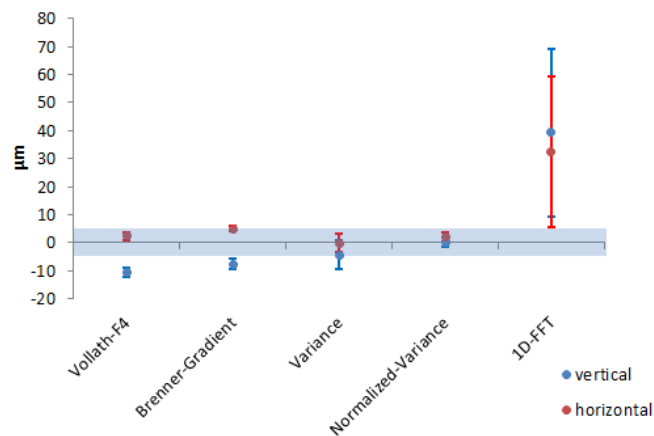


Figure 5.46: Results for locating the focal position ($z=0$) under vertical and horizontal sampling direction using a checkboard like focus pattern. The blue area around $z = 0$ indicates the range of depth of focus (DOF) position (from [E 12]).

A comparison of the accuracy of the investigated focus algorithms is exemplarily shown in Figure 5.46 for a checkboard like focus pattern. We found that the normalized variance algorithm yields the most precise focusing results with the lowest standard deviation.

The second maskless lithography setup utilizes a liquid crystal display (LCD) instead of a DMD. Both setups are described and compared in detail in [E 19] including a comprehensive discussion on light sources utilized for maskless lithography. In general, DMD devices allow for shorter wavelength exposures and higher power levels compared to LCDs. Hence, DMDs are suitable for structuring a

larger variety of polymers such as SU-8 resists. However, most LCDs, in turn, support grey levels and are therefore suitable for greyscale lithography. The LCD based setup is sketched in Figure 5.45 and utilizes an LCD (LC-R 1080, Holoeye) which rotates the polarization of the incident light. To convert the initially unpolarized light emitted by the red LED into intensity levels, we placed an LED in front of a polarizing beam splitter as sketched in Figure 5.45. All other optical components are similar to the DMD based setup, except that autofocusing was performed manually.

Methods for diffractive optical element fabrication: Binary and greyscale lithography

Fabrication of microstructures through maskless lithography requires photosensitive materials coated on a planar substrate. Depending on the intended use of the microstructure, we utilized S1813 (Shipley), SX AR-P 3500/6 (Allresist), ma-P 1275G (Microresist Technology) and Ormocomp (Microresist Technology) resists during our experiments. The first resist is a standard resist used in electronics fabrication, the second and the third are analog resists to create multilevel structures and the latter is an Ormocere™ hybrid polymer which is highly transparent in the VIS and used for waveguide fabrication. Except Ormocomp, all resists were distributed on standard 3 or 4 inch silicon wafer through spin coating and treated by a pre- and postbake on a hot plate prior to development. Experimental parameters for each resist can be found in [E 19], [E 20], [E 23], [E 30], [E 38].

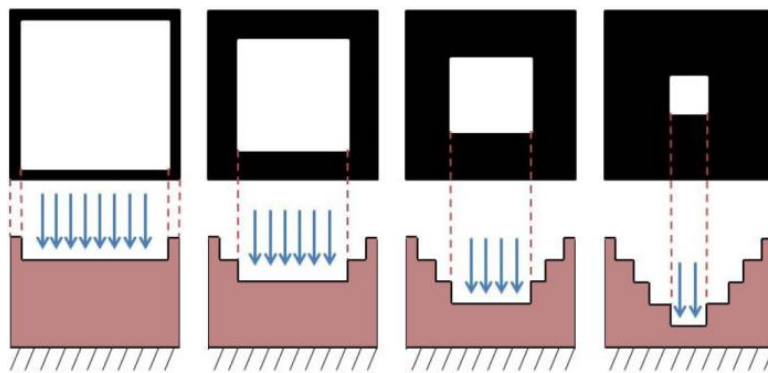


Figure 5.47: Exposure sequences to create four height levels in photosensitive resist using the DMD based setup (from [E 50]).

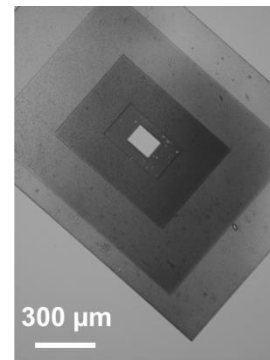


Figure 5.48: Microscope image of a pyramidal structure in ma-P 1275G resist fabricated through greyscale lithography.

Both setups as sketched in Figure 5.44 and Figure 5.45 which were utilized to create binary structures with only two height levels but also to fabricate multi-level structures exhibiting several discrete height levels. This is of special interest when fabricating diffractive optical elements (DOEs) as the diffraction efficiency strongly increases with the number of height levels. While the LCD based setup is suitable for 8-bit greyscale lithography directly, the DMD based setup is only capable of generating 2-bit black and white images. Therefore, an alternative exposure method is required which is illustrated in Figure 5.47 and relies on sequential exposure runs. Confocal topography

measurement results obtained at a four-level pyramid structure fabricated using sequential exposures is shown Figure 5.49. In diffractive optics, optical elements are often used in transmission but common photoresists coated onto silicon or silica wafers do not provide suitable optical properties in the VIS in terms of transparency. Therefore, a replica of the fabricated microstructures in transparent media such as polymers is required which can be achieved by soft stamp lithography as described in Section 5.2.2. In this work, we fabricated a PDMS copy of the resist microstructure and transferred its negative topography into PMMA polymer foils with a thickness of 375 μm [E 19], [E 20], [E 30].

Methods for waveguide fabrication: Maskless lithography

In addition to the fabrication of DOEs, maskless lithography provides a time and cost efficient alternative to established methods for waveguide fabrication such as etching methods. In this work, we pursued two different approaches for waveguide fabrication which are illustrated in Figure 5.49 [E 8], [E 23]. During the first method (see Figure 5.49, left), Ormocomp is spin coated onto a fused silica substrate. The liquid Ormocomp is selectively polymerized by maskless lithography using the DMD based setup and the remaining liquid monomer is removed in a developer bath (Ormodev, Microresist Technology), subsequently. In a next step, the Ormocomp structures are transferred into a PMMA substrate through a lift-off process and a bottom cladding is applied to embed the Ormocomp structures. To achieve wave guiding, the PMMA substrate and Ormocomp microstructures serve as cladding and core materials, respectively.

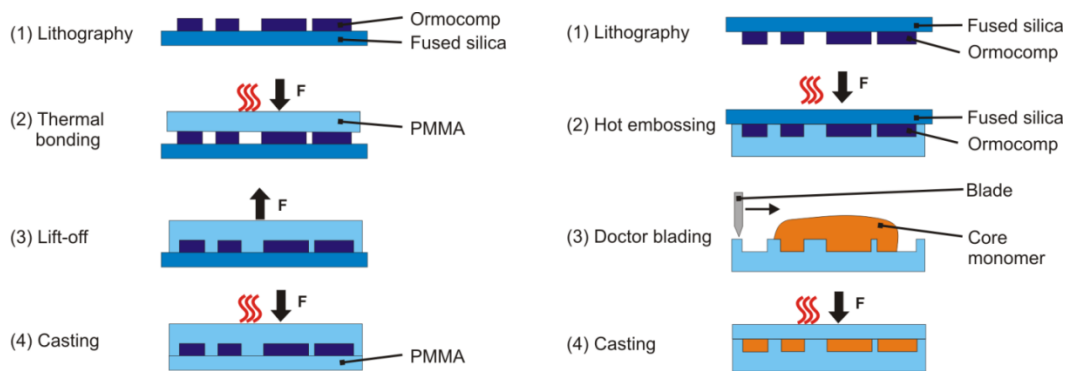


Figure 5.49: Process chains for fabrication of waveguides and optical structures: Direct structuring of monomers (left) and hot embossing based process (right) (from [E 23]).

The second approach is illustrated in Figure 5.49 (right). It is also based on micro-structuring and curing of Ormocomp hybrid polymer spin coated on a fused silica substrate. In contrast to the first method, the silica substrate is used as hot embossing stamp to create trenches in a PMMA foil without transferring the Ormocomp into the PMMA. Waveguides are fabricated by employing the doctor blading process described in Section 5.2.2.

Results: Diffractive optical elements

Maskless lithography lends itself for the fabrication of individual DOEs in binary as well as greyscale photoresists as described previously. In this work, various microstructures were transferred into photoresist to evaluate both, the LCD- and DMD-based lithography setups. Microscope images of diffraction gratings created in S1813 electronic resist are exemplarily shown in Figure 5.50.

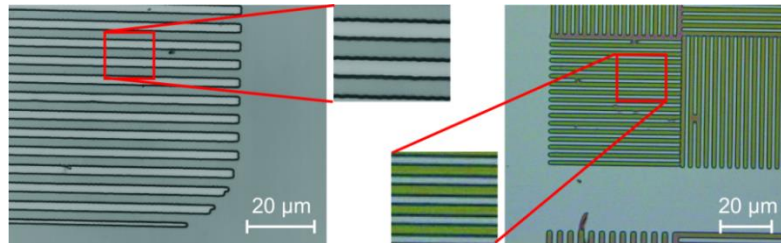


Figure 5.50: Microscope images of master stamps created in photoresist using (a) the DMD-based setup and (b) the LCD-based setup (from [E 30]).

A detailed discussion of the performance of both setups including their capability in terms of process cycle times and smallest producible feature size is given in [E 8], [E 19], [E 20], [E 30]. In summary, we achieved smallest feature sizes down to 824 nm using lenses with an $NA = 0.3$ and an LED light source with a wavelength of 435 nm. The resolution can theoretically be reduced to 176 nm using immersion lenses with an $NA = 1.4$. Fastest exposure runs were carried out at exposure times of 10 seconds to structure an area of 1.4 mm x 1.1 mm during a single exposure. Areas of 3 cm x 2.5 cm were structured through a stitching process utilizing the lateral piezoelectric translation stage (results are presented later in Figure 5.54). However, using the DMD device, we observed a significant line edge roughness compared to the LCD setup. This effect is due to a larger pixel pitch of the DMD based setup of 14.3 μm compared to that of the LCD based setup of 7,8 μm which leads to resolved pixels in the microscope projection system when using the DMD.

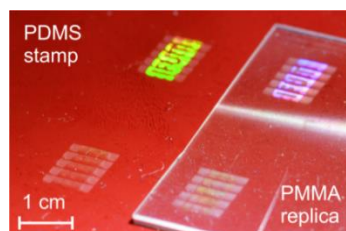


Figure 5.51: Large area diffractive structure on a PDMS stamp containing two structured areas and corresponding PMMA replica fabricated using the HEX03 (from [E 19]).

To create DOEs in polymers such as PMMA, the silicon substrate containing the microstructures were casted by a PDMS monomer (Sylgard 184, Dow Corning) which was cured in a desiccator to remove air inclusions subsequently. After removal from the silicon wafer, the PDMS copy was used as embossing stamp in both, a commercial hot embossing machine (HEX 03, Jenoptik) and a lab-made low-cost embossing device as described in [E 19]. A photograph of a DOE PDMS master stamp

and its PMMA replica are shown in Figure 5.51. The structure consists of a periodic grating structure with a pitch of $5.37\ \mu\text{m}$ at a grating depth of $471\ \text{nm}$ which were determined from confocal microscopy measurements [E 19]. In general, confocal measurements reveal that performing maskless lithography, PDMS molding and hot embossing subsequently is a suitable method to create microstructures on polymer substrate such as PMMA. It yields form deviations between design and final PMMA structure of less than $20\ \text{nm}$ and $150\ \text{nm}$ in vertical and lateral direction, respectively [E 19], [E 20], [E 30]. The latter deviation is caused by stretching of the PDMS stamp. However, this can be accounted for by considering the PDMS material flow as described in Section 5.3.2. For a detailed analysis in terms of stamp quality and replication accuracy we refer to [E 19], [E 20], [E 30].

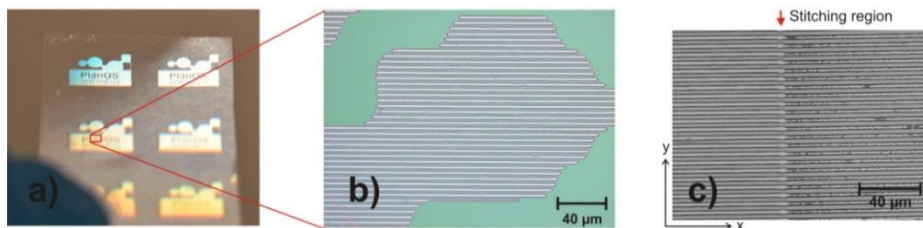


Figure 5.52: Photograph of a logo with an incorporated diffraction grating replicated in a thin PMMA foil (a), magnified image of the diffractive structure on the logo (b), and microscope image of a diffraction grating within the stitching region (c) (from [E 20]).

A great advantage of maskless lithography compared to its mask-based counterparts is the capability to combine a macroscopic geometry and a diffractive microstructure as can be seen in Figure 5.52.

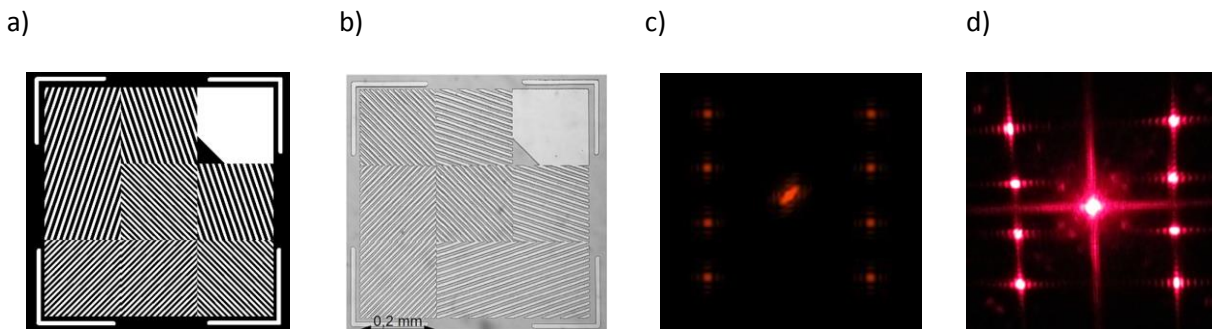


Figure 5.53: Diffractive optical element to generate an “H” shaped light distribution: a) results of the optical design; b) fabricated DOE in S1813 photoresist; c) light distribution used as target distribution for the optic design; d) experimentally obtained light distribution using the fabricated diffractive optical element (HOT 2016, unpublished).

The logo which is shown in Figure 5.52(a) was fabricated using 5×5 single exposure runs utilizing a stitching process which exhibits a remaining stitching error in the range of $300\ \text{nm}$ as obvious from Figure 5.52(c). Application examples of the presented fabrication method range from DOEs for holography, beam shaping and illumination technology. An application in illumination technology is

exemplarily shown in Figure 5.53 where a DOE is used to generate a light distribution in the shape of an “H” (see Figure 5.53(c)). The DOE concept is based on a 3 x 3 cell array including diffraction gratings with different grating periods and orientations (see Figure 5.53(a)). To design DOEs, we implemented an iterative Fourier transform algorithm (IFTA) in Matlab™ using the Gerchberg and Saxton algorithm [92] which is an alternative phase retrieval method to the algorithm utilized in Section 5.1.6 [E 5]. Light propagation itself is calculated using FFT based angular spectrum propagation methods (see [93]). The algorithm converges towards an optimal DOE design. In our case, each grating cell generates a light spot in the far field (3 m distance). The cell array to display an “H” was fabricated by maskless lithography in S1813 photoresist coated on a silicon wafer and is shown in Figure 5.53(b). To compare the initial optical design to experimental data, we recorded the far field diffraction pattern using a helium neon laser as light source. As can be seen from Figure 5.53(c) and Figure 5.53(d), the experimentally obtained light distribution is in very good agreement with the optical design. In future applications, we also aim at the fabrication of thin back and brake lights for applications in cars, for example, using DOEs and laser diodes which meet legal requirements but also provide novel and more flexible design methods in the automotive sector.

Methods, Results: Replication of diffractive optical elements in sheet metals

Structuring substrates by means of soft stamp HEL using PDMS stamps is limited to thermoplastics or soft materials which do not lead to a deformation or destruction of the stamp. However, the methods described previously are directly transferrable to the fabrication of DOEs and holograms on metal surfaces. A corresponding process chain was developed within this work and is sketched in Figure 5.54 [E 38], [E 50].

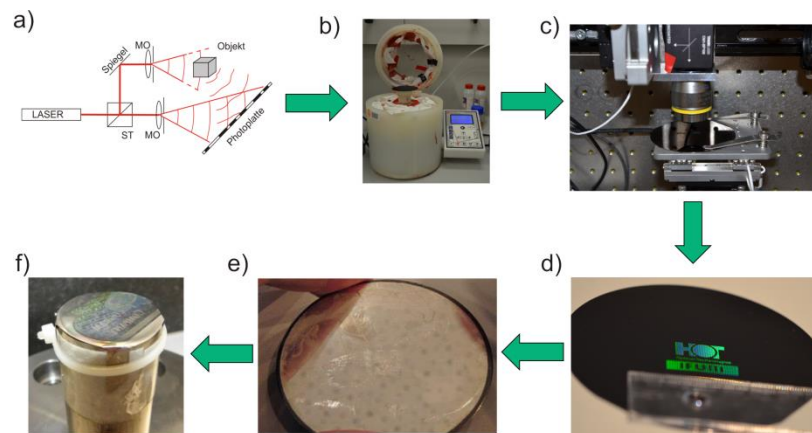


Figure 5.54: Nickel stamp fabrication process chain for embossing DOEs and holograms into sheet metals: a) DOE design; b) coating photoresist onto a silicon substrate; c) maskless lithography to create DOEs; d) development of resist; e) negative nickel copy of DOE by electroplating; f) integration on embossing stamp (from [E 50]).

In an initial step, the DOE or hologram is designed with the aid of computer algorithms described briefly in Section 5.3. This step is followed by fabricating the calculated micro- and macrostructure of the DOE in photoresist utilizing maskless lithography. An example of a DOE acting as a logo is

shown in Figure 5.54(d). In contrast to the previous process chains, a rigid negative copy of the microstructure is obtained by electroplating in nickel. The copy is attached on top of an embossing stamp and used for embossing subsequently. Examples of holograms embossed in copper and DC 04 steel using nickel stamps are shown in Figure 5.55.

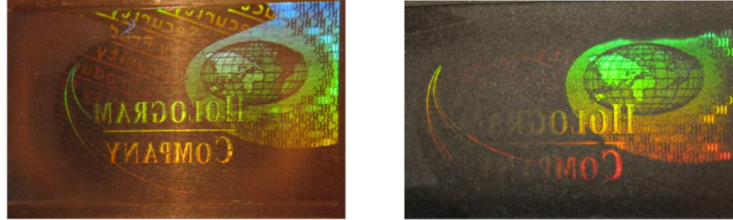


Figure 5.55: Holograms created on metal substrates through embossing using an electroplated nickel stamp: copper substrate (left) and DC 04 steel (right) (from [E 50]).

Results: Waveguiding and integrated photonic elements

In addition to DOE fabrication, we utilized maskless lithography to create linear waveguides, 3 dB splitters and interferometric structures such as Mach-Zehnder interferometers as shown in Figure 5.56 [E 8], [E 23].

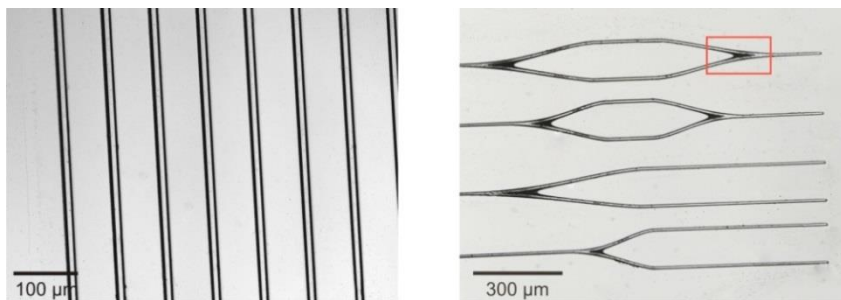


Figure 5.56: Microscope images of Ormocomp structures on fused silica cover slide fabricated by maskless lithography: linear waveguide array (left) and Y-splitter and Mach-Zehnder interferometers (right) (from [E 23]).

As described previously in this section, first we fabricated waveguide structures made from Ormocomp on a silica substrate before applying a thermally supported lift-off process or, alternatively, using the silica substrate as hot embossing stamp. Results of fabricated Ormocomp structures are displayed in Figure 5.56. Fabrication was carried out utilizing the DMD-based setup due to its shorter exposure wavelength of 405 nm required to cure the Ormocomp compared to the one of the LCD-based setup of 435 nm. Waveguide structures which are shown in Figure 5.56 were embossed into a PMMA foil with a thickness of 375 μm and filled with NOA68 core material as described previously. A microscope image of an optical fiber launching coherent light at a wavelength of 635 nm into a 3 dB splitter is shown in Figure 5.57. As can be observed there, wave guiding as well as spitting is achieved.

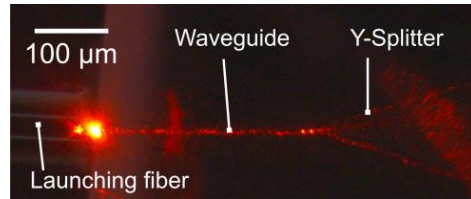


Figure 5.57: Laser light with a wavelength of 635 nm launched into the Y-splitter fabricated by hot embossing and doctor blading (from [E 23]).

However, confocal topography measurements carried out on the stamp yielded a remaining surface waviness and line edge roughness with amplitude and roughness values of approximately 20 nm which limits light propagation to a distance of a few centimeters [E 8], [E 23]. Again, this is readily explained by resolved pixels using the DMD setup. The shape of each single pixel is transferred into the Ormocere and leads to the observed roughness. We expect that using a smaller pixel pitch in a future setup will resolve these issues and, thus, will reduce optical losses.

5.3 Optical Design

5.3.1 Overview

Fabrication of integrated photonic devices and also diffractive optical elements is inextricably connected to a preceding optical design task which needs to be carried out to optimize a specific functionality of the optical element to be produced. In this work, we utilized several design methods ranging from simple ray tracing (see Section 4.4.1) to more complex methods such as coupled wave analysis (see Section 4.4.2), while also taking the vector and wave nature of light into account. These methods were both self-implemented in MatlabTM and C++ as well as provided by commercially available optical design software tools such as ZEMAXTM, RSoftTM and ComsolTM. A brief outline of the most important self-implemented simulation algorithms is given in Section 4.4. For a comprehensive description of the numerical as well as the theoretical background of the algorithms utilized in this work, we refer to [17], [18], [47], [51], [52], [93]. A short overview of integrated optics related design methods is given in [E 11].

In this section, beam propagation method (BPM) based simulation results of interferometric sensors are presented and, in addition, we introduce a novel approach to design diffractive optical elements on the surface of freeform objects. The latter method also takes workpiece deformation during fabrication through hot embossing by means of FEM simulations into account. The introduced approach is not only suitable to design diffractive structures such as holograms but also lends itself for the design of integrated photonic elements on freeform surfaces.

The results presented in this section are partially based on publications [E 8], [E 11], [E22], [E 23], [E 34], [E 38], [E 47], [E 50].

5.3.2 Diffractive Optical Elements

Diffractive optical elements (DOEs) are present in a broad range of applications ranging from laser beam shaping, planar focusing elements to holography. The latter application is often related to product protection where DOEs are integrated in products as copy protection items. The specific design method utilized for DOEs development is strongly dependent on its purpose. For example, in integrated optics diffraction gratings are often utilized as coupling elements such as the ones described in Section 5.4.3. Such devices are commonly designed by means of RCWA (see Section 4.4.2) [34]. The RCWA algorithm calculates the complex field which is diffracted by 1-D or 2-D gratings. However, for the design of micro-optical elements which generate a defined intensity in the far field, design methods based on the paraxial field propagation such as the Huygens-Fresnel principle and angular spectrum propagation (ASP) are often used [93]. A main challenge when designing such elements is that the design intensity pattern does not give any information about the phase of the involved electromagnetic wave. Hence, algorithms such as the Gerchberg-Saxton algorithm are required to retrieve the phase distribution introduced to an incident electromagnetic wave by the DOE which generates a desired intensity pattern [65]. In digital holography as well as

diffractive optics, iterative Fourier transform algorithms (IFTA) are frequently applied to obtain the design of a DOE [92]. Here, a common technique is to start with a random phase distribution in the DOE plane and propagate the corresponding electromagnetic field virtually into the far field where the diffraction pattern is to be observed. In a next step, the obtained complex field amplitude in the far field is multiplied by the amplitude of the desired design pattern and an inverse propagation to the DOE is carried out. The corresponding phase distribution is, again, used to calculate the far field diffraction pattern. This procedure is performed iteratively until a predefined stop criterion is reached. In this work, the IFTA algorithm was implemented in Matlab™ to calculate digital holograms which are to be transferred in photoresist by maskless lithography and then into polymers or even metals (see Section 5.2.4) [E 30], [E 34], [E 38], [E 47], [E 50].

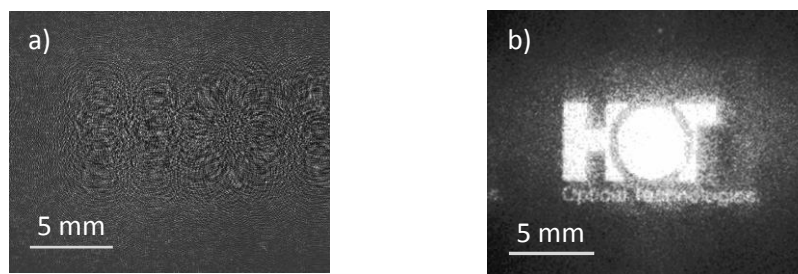


Figure 5.58: Digital hologram of HOT logo: a) calculated amplitude hologram by means of the IFTA algorithm; b) Image of the experimental reconstruction using a spatial light modulator (HOT 2016).

Figure 5.58(a) exemplarily shows the transmission of a calculated amplitude hologram using the IFTA algorithm which generates the logo of our research centre (HOT) in the far field. The experimental reconstruction of the “HOT”-hologram is shown in Figure 5.58(b). For the experimental reconstruction, a liquid crystal display (LCD) from Holoeye (LC2002) was utilized.

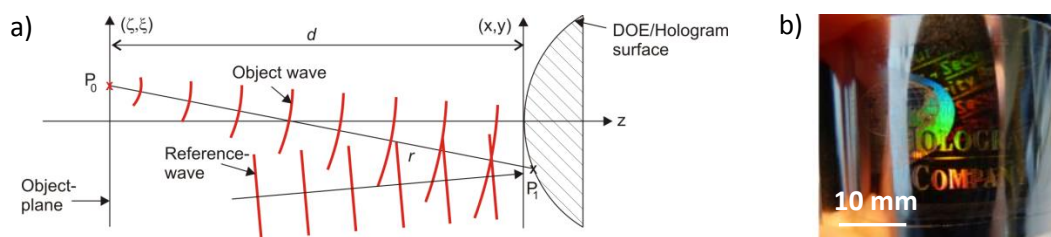


Figure 5.59: Calculating holograms on curved freeform elements: a) sketch of the simulation geometry; b) photograph of a fabricated curved hologram on sheet metal (from [E 50]).

In certain applications such as in the case of design or product protection items, the hologram or DOE is not placed on a flat surface but exhibits a curved shape defined by the shape of the product. In this case, classical IFTA algorithms are limited as they most often rely on angular spectrum propagation (ASP) methods to calculate electromagnetic wave propagation. ASP is limited to the

simulation of light propagation between planar DOEs and observation planes (compare [17], [93]). Hence, these algorithms are not suitable when dealing with freeform DOEs. Therefore, we implemented algorithms to calculate holograms based on propagation of spherical waves which correspond to 3-D Green's function in free space, a fundamental solution to the Helmholtz equation [17]. The general layout of the numerical problem is sketched in Figure 5.59(a). At the expense of numerical efficiency, we do not use ASP. Instead, the hologram freeform surface serves as source plane for spherical waves which are propagated from the surface to the observation plane. Hence, integrating over all spherical waves is required and the integration domain can be arbitrarily shaped – in contrast to ASP. The numerical effort is directly determined by the numerical grid size used for integration over the hologram surface and the observation plane. However, the numerical effort can be reduced to a certain extent by using interpolation methods, which virtually reduce the grid size without leading to aliasing effects in the calculated fields. For example, we introduced a linear interpolation method in [E 22].

In addition to calculating holograms, we also included the fabrication process and the resulting material deformation in the numerical simulations. Since all processes utilized in this work are based on embossing using stamps which were fabricated by standard semiconductor technology or maskless lithography (see Sections 4.2 and 5.2.4), we are limited to planar substrates. However, freeform DOEs were created by deep drawing or embossing using flexible stamp materials (PDMS) (see [E 50]). To achieve DOEs on curved surfaces, first we fabricated the DOE on a planar substrate in photoresist and transferred a negative copy to PDMS or nickel through spin coating or electroplating, respectively. In the latter case, the nickel DOE was embossed in steel or copper sheet metal [E 50]. In a final process step, the DOEs obtained its final freeform shape by forming the sheet metal through deep drawing or by embossing the PDMS into curved polymer surfaces. Both processes either lead to a material flow of the workpiece or stamp. In both cases, the micro- and macro-topography of the DOE undergoes deformations during the process which are required to be compensated in the optical design. This was achieved by carrying out FEM simulations of the material deformation during the deep drawing process which were carried out at the Institut für Umformtechnik und Umformmaschinen (Leibniz Universität Hannover, Germany). Figure 5.60 visualizes the general workflow of our approach: First, the deformation of the workpiece was simulated by means of FEM simulations. A coarse grid was used as FEM nodes to simulate the material flow during deep drawing or embossing. The 3-D movement of the nodes corresponds to the material flow during the process and was used to calculate a coordinate transform between the initial and the processed material coordinates. 2-D deformation vectors are shown in Figure 5.60(c) which were calculated for a planar sheet metal plate made from copper, which is deep drawn to a ball segment shaped surface as shown in Figure 5.60(b). The inverse of the vectors define the inverse coordinate transform and yield the structure of the planar substrate to be fabricated. Up till now, only the deformation of the macro-geometry was considered, however, the diffractive microstructure is also deformed and optical properties may change. To also account for this deformation, we interpolated the deformation between four proximate nodes linearly and matched

each of these deformed segments including the DOE micro-structures to the planar substrate geometry.

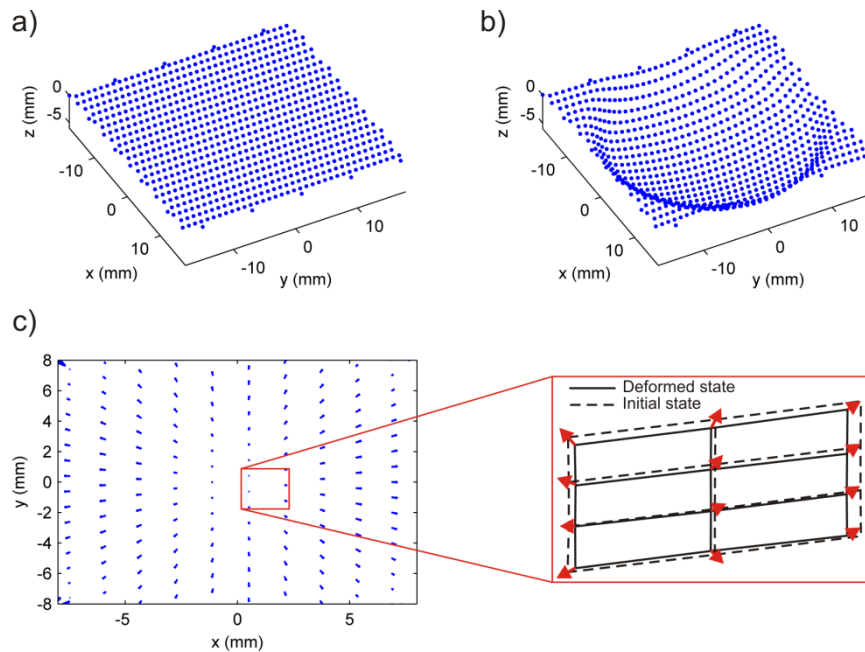


Figure 5.60: Macroscopic deformation of workpiece during deep drawing process simulated by means of FEM (IFUM, Leibniz University Hannover) – data points represent FEM nodes which are fixated on the surface of the workpiece: a) initial workpiece geometry; b) workpiece geometry after deep drawing; c) local material movement between initial and processed workpiece state, arrows indicate material movement; enlargement illustrates geometrical deformation of quadrangle segments between adjacent nodes due to deep drawing (according to [E 50]).

Hence, to design and fabricate DOEs, we performed following consecutive steps: First, we used the IFTA-like algorithm developed for freeform surfaces and determined the DOE or hologram structure on the surface. Then, we simulate the material flow during forming of the freeform from its final shape to a planar substrate and, hence, inverting the fabrication process virtually. The next steps include the fabrication of the diffractive microstructure by means of maskless lithography and, finally, performing the deep drawing or hot embossing process to obtain the final shape of the curved DOE or hologram integrated in the freeform surface.

5.3.3 Integrated Photonics

In integrated photonics, size and optical functionality of optical element to be designed determine the numerical method utilized as design tool. Features which exhibit sizes in the range of up to a few ten microns such as ring resonators or photonic crystals are commonly designed through finite-difference time-domain (FDTD) methods or finite element methods (FEM). Also diffractive elements such as grating couplers are designed using FEM and also RCWA [E 25].

If feature sizes are large compared to the wavelength of light, ray tracing methods are still state-of-the-art and are frequently used for the design of multimode waveguides and optical elements. Examples are micromirror couplers including micro-optics to enhance the coupled optical power between, e.g., light sources and waveguides. However, ray tracing is based on Monte-Carlo (MC) simulations which require up to several hundred thousand light rays to be traced through the optical system. In this work, we utilized an alternative approach to decrease the computation time compared to the classical ray tracing approach [E 11]. Here, instead of tracing rays from the source to the image, we trace rays from the image back into the optical, which is numerically more efficient if the majority of rays starting in object space do not reach the image space. The approach was implemented in MatlabTM and used to simulate the intensity distribution behind multimode waveguides. Results are exemplarily shown in Figure 5.61 for a straight and lensed fiber end facet.

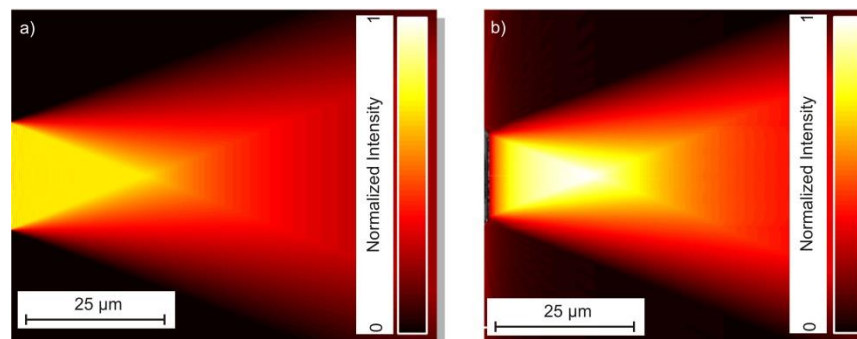


Figure 5.61: Simulated intensity distributions behind the end facet of a multimode optical fiber: a) planar end facet; b) curved end facet (from [E 11]).

If waveguide dimensions decrease down to the few micron range and only a few modes or only a single optical mode propagate inside the waveguide, alternative design methods are utilized which are often based on beam propagation methods (BPMs) as briefly described in Section 4.4.3. In this work, we utilized BPM for the design of straight and bend waveguides, Y-shaped beam splitters and also sensors such as Mach-Zehnder interferometers (MZI) as shown in Figure 5.62 [E 22].

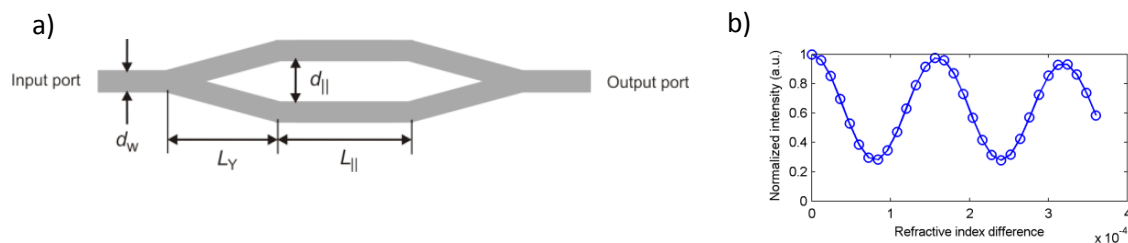


Figure 5.62: Mach-Zehnder interferometer: a) Sketch of the sensor design; b) simulated intensity at the output port of the interferometer as function of a refractive index difference between the two interferometer arms indicated by $L_{||}$ (from [E 23]).

5.4 Integration of Photonic Components

5.4.1 Overview

Fabrication of photonic devices requires the integration of various active as well as passive optical components into a single device or thin substrates in the case of PICs. Most importantly, suitable coupling structures are required which enhance the optical power transfer from one component to another. Geometrically simple examples are Y-shaped waveguide branches which serve as beam splitters [94]. Various fabrication techniques were utilized for fabrication of Y-splitters including laser direct writing [95]. Applications were even extended to optical splitters for surface plasmon polaritons [96]. Despite straight and bent waveguides, Y-shaped beam splitters represent basic components for a large variety of devices including Mach-Zehnder interferometers [14] and also optical switches in polymer materials which take advantage of thermo-optical effects [97].

Another major challenge in integrated photonics - even today - is an efficient coupling of light in and out of waveguides. In the multimode regime, micromirrors are frequently used where light coupling is achieved through a reflecting and 45° inclined surface integrated in the waveguide. Such micromirrors were created in polymers through, for instance, soft stamp NIL [98], UP-milling or novel lithographical techniques enabling 45° inclined flanks in photoresist [99]. Achieved coupling loss values are typically in the range of 1.6 to 1.88 dB which enable their application in interconnects such as printed circuit boards (PCBs) [98], [100]. Coupling efficiencies are often increased by combining micromirrors and microlenses [100].

However, if waveguides are operated in the singlemode regime, alternative coupling strategies are often pursued due to higher coupling efficiencies compared to micromirrors. As discussed in Section 4.1.3, evanescent field couplers are prominent examples for lateral coupling [22], [101] but similar concepts were also utilized as waveguide-based evanescent field sensors for label-free detection of substances based on absorption [102]. To couple light in vertical direction, grating couplers (see Section 4.1.3) were also created in polymer waveguides by embossing [103] even using reel-to-reel processes [76]. However, the latter results are limited to slab waveguides. Grating couplers were applied to launch light from a vertically positioned fiber into a horizontally oriented waveguide [104].

In addition to a suitable selection of coupling structures, positioning the optical components to be connected is crucial to achieve high coupling efficiencies. For instance, if fibers are to be connected to silicon-based photonic components, V-shaped self-alignment structures are frequently applied to force fibers into an aligned, pre-defined position. However, most of these approaches are based on butt-coupling [105]. Self-alignment structures have already been utilized in various application e.g. to connect VCSELs and photodiodes to waveguide arrays [106]. In recent years, optical integration has also demanded 3-D coupling structures and optical wire bonding was investigated by taking advantage of recent developments in 2-photon-polymerization [107]. These structure were used to create 3-D interconnects between silicon based photonic boards by determining the optimal optical

path between waveguides and writing these structures into UV-sensitive resin in an automated process [108].

In this work, we investigated the basic design and fabrication of fully polymer-based optical components such as Y-splitters, which form building blocks for more complex optical networks. A special emphasis was placed on coupling structures based on 45° angled micromirrors and focused diffraction gratings. In contrast to previous work, we explicitly rely on polymer materials and fabrication processes which are reel-to-reel capable. In addition, we introduced a method for creating optical interconnects between side-emitting light sources such as laser diodes (LDs) and embedded polymer waveguides. Our method automatically compensates for misalignment between both the light source and waveguide which is based on self-written waveguides (SWW) [109]. We demonstrate the performance of our coupling strategies by connecting LDs and photodiodes (PDs) to hot embossed waveguides. Also, we present results on fabrication of transmission lines using the investigated coupling structures. In this work, we developed both fully polymer based transmission lines as well as hybrid transmission lines including polymer waveguides and semiconductor based light sources and detectors.

The results presented in this section are based on publications [E 1], [E 3], [E 13], [E 15], [E 21], [E 25], [E 27], [E 31], [E 33].

5.4.2 Beam splitters

In this work, we fabricated beam splitters with splitting ratios of 1:2, 1:4 and 1:8 through a hot embossing process and subsequent doctor blading using PMMA as substrate and various polymers as core materials, as described in Section 5.2.2. The 1:4 and 1:8 splitters consist of consecutive 1:2 splitters designed as Y-shaped waveguide branches.

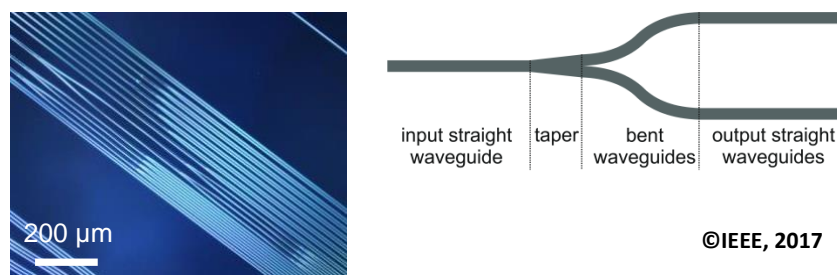


Figure 5.63: Microscope image of a hot embossing silicon stamp for fabrication of Y-splitters (left) and corresponding splitter design (right) (from [E 3]).

A microscope image of the silicon stamp utilized for hot embossing as well as the Y-shaped splitter design are shown in Figure 5.63. The Y-splitters consist of a straight waveguide followed by a taper region which is split into two bent waveguides. The fabricated splitters were characterized with respect to their optical losses and splitting ratios according to Section 5.1.

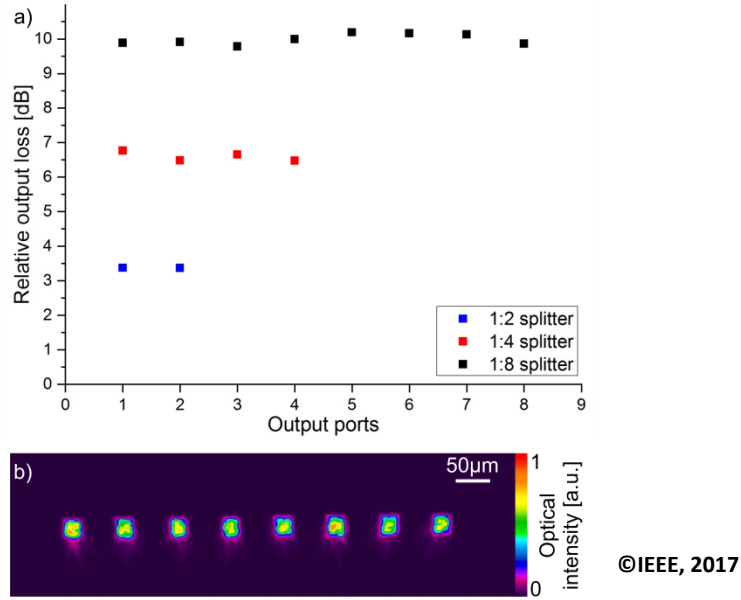


Figure 5.64: An example of characterization results of beam splitters fabricated using PMMA and NOA68 measured at 633 nm: (a) Relative output losses for different splitting ratios and (b) beam profile corresponding to a 1:8 splitter (from [E 3]).

Figure 5.64(a) exemplarily displays output loss measurements obtained at each exit port of the 1:2, 1:4 and 1:8 splitters which were obtained from end-facet intensity measurements (see Figure 5.64(b)) using an optical profiler (Thorlabs). Measurement results obtained at wavelengths of 633 nm and 850 nm are summarized in Table 5.5 using NOA 68 and Supraflex as core materials.

Table 5.5: Characterization results corresponding to 16 mm long beam splitters for the investigated core materials, wavelength and splitting ratios (from [E 3]).

Core material	λ [nm]	Splitting ratio	Excess loss per branching [dB]	Relative output loss [dB]
NOA 68	633	1:2	0.36	3.36 ± 0.01
		1:4	0.29	6.59 ± 0.12
		1:8	0.32	9.98 ± 0.14
	850	1:2	0.12	3.12 ± 0.03
		1:4	0.20	6.40 ± 0.05
		1:8	0.16	9.49 ± 0.30
Supraflex	633	1:2	0.13	3.13 ± 0.02
		1:4	0.21	6.42 ± 0.08
		1:8	0.15	9.47 ± 0.15
	850	1:2	0.20	3.20 ± 0.04
		1:4	0.11	6.23 ± 0.09
		1:8	0.11	9.34 ± 0.12

A detailed discussion of the results is given in [E 3]. In summary, we observed that splitting ratios of 3 dB, 6 dB and 9 dB were obtained. As can be seen in Table 5.5, optical losses per branching region

are as low as 0.11 dB due to an improved optical design of the splitter. The relative output losses given in Table 5.5 are compared to the intensity at the input port of the splitter and also include excess losses. Excess losses consist of additional propagation losses of the splitter compared to straight waveguides due to an increased waveguide length which results from required bend structures. The standard deviation given for the relative output losses relates to the intensity differences measured at each exit port and is, hence, an indicator for the splitting homogeneity which ranges between 0.01 dB and 0.30 dB. Therefore, the presented optical design and fabrication method is well-suited for manufacturing of optical splitters.

5.4.3 Optical Couplers

Micromirror Couplers

As micromirror-based splitters provide one of the highest coupling efficiencies for multimode applications, we integrated 45° angled micromirror splitters in multimode waveguides with rectangular cross sections of $25 \times 25 \mu\text{m}^2$. Since 45° mirror couplers were investigated by various groups, our main aim was to develop a cost effective method to create these coupling structures in thin polymer foils.

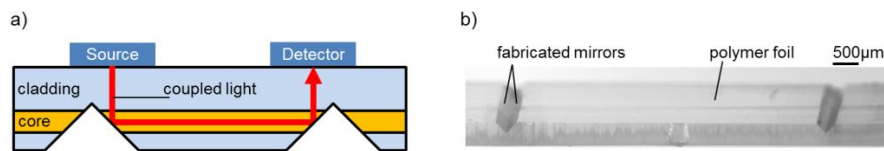


Figure 5.65: Light coupling through a micromirror structure: a) Sketch of the concept, b) Result of slotting fabrication process (from [E 25]).

The basic concept for integration of light sources and detectors is illustrated in Figure 5.65(a) [E 25]. A V-shaped groove is created inside the waveguide at the opposite side of the source or detector to be connected to the foil. This method especially lends itself to couple light from vertically emitting sources such as VCSELs into the waveguide. The 45° mirror reflects and redirects the vertically incident light beam into the polymer waveguide. Reflection either takes place due to TIR at the air-core boundary or the reflection coefficient of the mirror is enhanced by a few ten nanometer thin alloy layer which was coated onto the mirror surface by magnetron sputtering (see Section 4.2.1). Here, we utilized two different approaches to create such mirror couplers: first, we fabricated waveguides through hot embossing according to the method described in Section 5.2.2. The micromirror was created by a slotting process using a UP milling machine (Micromaster, Kugler), as shown in Figure 5.65(b). However, slotting requires expensive diamond tools and manufacturing equipment which greatly increases asset costs of such production lines. Therefore, we opted for a second process which only relies on hot embossing utilizing an additional alloy stamp which contains an optically smooth surface and a single ridge structure with triangular cross section. For this method, we employed the waveguide fabrication process illustrated in Figure 5.32 (Section

5.2.2) where a hot embossed trench is filled with liquid core monomer and thermally cured after applying an additional PMMA cover substrate. To create mirror grooves inside the polymer, the cover substrate was placed on the hot embossing mirror stamp before curing and pressed into the waveguide by applying an additional force using the force unit of the HEX03 hot embossing machine. The force was maintained during thermal curing resulting in a permanent mirror groove inside the waveguide. During the fabrication, the ridge was oriented perpendicular with respect to the waveguides to achieve light coupling into the waveguide. Using this technique, we created couplers with coupling losses of 4.2 dB.

Grating couplers

Grating couplers are widely used in integrated photonics especially for light coupling in SOI-based photonic devices. The aim of our work was to transfer grating couplers into thin polymer foils also developing fabrication techniques which are compatible to high-throughput and low-cost reel-to-reel processes.

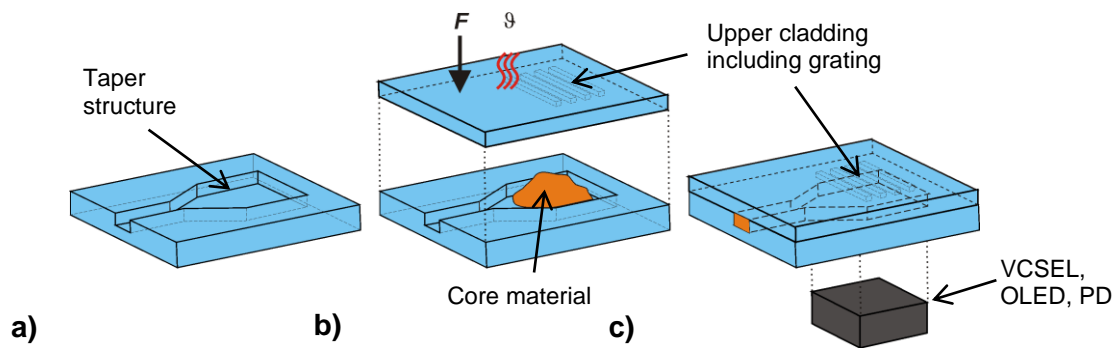


Figure 5.66: Process chain utilized for grating coupler fabrication: a) hot embossing of lower cladding; b) applying core material and covering substrate with upper cladding including hot embossed grating; c) mounting light source or detector through adhesive bonding (from [E 27]).

The fabrication process utilized in [E 25] and [E 27] for fabrication of grating couplers is schematically sketched in Figure 5.66. The coupler consists of a straight waveguide which converts into a taper region to increase the area which allows vertical light coupling. The taper is covered by a cladding with an incorporated grating coupler. Both the lower cladding containing the waveguide and taper and the upper cladding including the coupler grating were manufactured through hot embossing. To enhance the diffraction and, hence, the coupling efficiency of the coupler, the grating region was coated by a silver layer with a thickness of ten nanometers through magnetron sputtering. In future work, we also aim at using high refractive index polymers instead of silver layers to fabricate fully polymer based couplers. During a final process step, the core material was dispensed on the trenches of the lower cladding, the upper cladding was applied using a holding force to reduce the residual layer between the upper and lower cladding and cured by UV exposure subsequently.

Prior to fabrication, the optical layout of the coupler was optimized using the commercially available photonic design tool RSoft™ (Synopsis). Light propagation inside the waveguide and taper regions were simulated using BPM (see Section 4.4.3) while the grating coupler itself was optimized with respect to grating depth and period length using RCWA-based algorithms (see Section 4.4.2) as described in [E 27]. The grating period Λ determines the diffraction angle and matches the wave vector of the incident light to the propagation constant β_m of a certain waveguide mode of order m (see Section 4.1.1). The grating step height h is strongly related to the diffraction efficiency η of the grating and needs to be chosen carefully by means of optical simulations. In our example, numerical simulations yielded an optimal grating period $\Lambda = 560$ nm at a grating height of $h = 105$ nm. Further improvements were achieved in numerical simulations using blazed gratings. However, the fabrication of such gratings requires methods such as ion beam writing which was not accessible. However, to enhance the coupling efficiency, the grating was designed as focusing grating. Figure 5.67(a) shows an REM image of the hot embossed focusing grating in PMMA which serves as diffractive element as can be seen in Figure 5.67(b). A microscope image of the PMMA waveguide and taper trenches which were also created through hot embossing are shown in Figure 5.67(c).

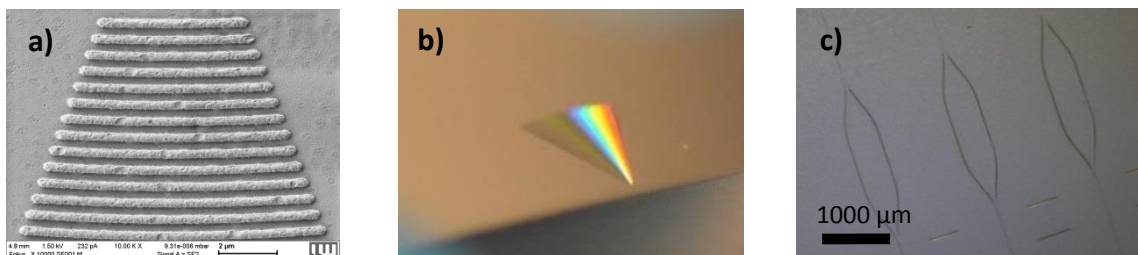


Figure 5.67: Single components used to fabricate grating couplers: a) REM image of a hot embossed focusing grating in PMMA; b) macroscopic image of focusing grating; c) hot embossed taper array (partially from [E 27]).

Measured coupling losses of the fabricated coupler are in the range of 6.2 dB using silver coatings [E 27]. However, the advantage of the presented fabrication method is that it is easily implemented as reel-to-reel process chain including two R2R hot embossing steps to fabricate the upper and lower cladding, dispensing the core material and a final lamination step including UV curing of the core material.

Self-written waveguides

So far, structures for coupling light vertically into the waveguide as well as their fabrication based on hot embossing were discussed. A drawback of these methods, in addition to their limitation to vertical coupling, is that positioning of the optical components to be connected to the waveguides is crucial. Even if pick-and-place automates are used in industrial fabrication, they are limited to position accuracies of a few ten microns which is not sufficient in most optical applications. To overcome such drawbacks, self-alignment structures such as V-shaped grooves for positioning of fibers were introduced. However, if side-emitting laser diodes (LDs) are to be connected to

waveguides, such self-alignment structures are not applicable. Here, we introduce a method to automatically compensate for positioning errors between waveguides and LDs in the range of a few ten microns which relies on self-written waveguides (SWW) as described in [E 33]. During the formation of SWW, light with a wavelength of 405 nm is launched from a fiber tip into liquid monomer. Due to light absorption at the fiber tip, the monomer starts to locally polymerize around the tip. This polymerization leads to a local increase of the refractive index of the cured polymer in comparison to the liquid monomer, which acts as a seed point and a straight waveguide starts to propagate into the monomer. Such straight SWW can be used as interconnects between two fibers, as shown in Figure 5.68(a). However, an accurate positioning of the fibers is still required to achieve a sufficiently high coupling efficiency.

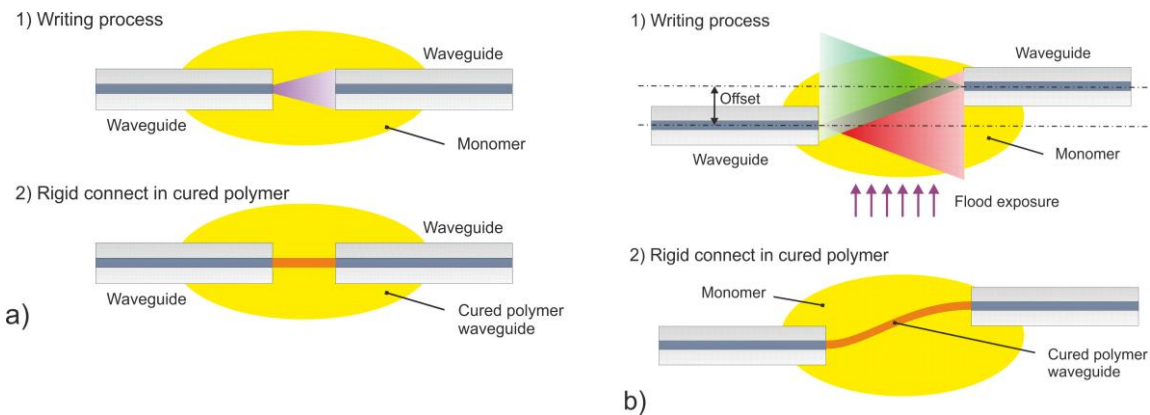


Figure 5.68: Scheme of the writing process of (a) SWW and (b) 2-wavelength-SWW (from [E 1]).

To create such straight SWW, we used lab-made polymers consisting of Syntholux (Synthopol, Buxtehude, Germany) and 1-Hydroxy-cyclohexyl-phenyl-ketone (Ciba Irgacure 184, BASF, Basel, Switzerland) with 2.1 wt.-% as UV-sensitive photo initiator. The polymer was provided by the group of Prof. Hanemann at Imtek, Albert-Ludwigs-University Freiburg. A detailed description is given in [E 13] and [E 1]. The fabricated SWWs were analyzed experimentally with respect to optical losses at various wavelengths, as summarized in Table 5.6.

Table 5.6: SWW Attenuation Measurement (from [E 15]).

Wavelength [nm]	Attenuation [dB/cm]
406	12.5
638	1.0
685	1.5
850	0.8

The fabrication of SWWs discussed so far has two major drawbacks which limit their application for interconnect manufacturing: First, SWW writing requires light sources in the UV ($\lambda = 405$ nm) and, secondly, SWWs propagate along straight lines into the monomer and, hence, accurate alignment is still mandatory to achieve low coupling losses. To overcome these drawbacks, we developed an

alternative approach for horizontal coupling which is also based on SWW as depicted in Figure 5.68(b). In contrast to our first approach, light in the VIS is launched from both components into the monomer. The process is illustrated in Figure 5.68(b) where two fibers which exhibit laterally misaligned optical axes are to be connected. From each fiber, two diverging light cones are launched into the monomer. The light intensity inside the overlapping area of both light cones is increased but polymerization is not started since wavelengths in the VIS are utilized. The polymerization is triggered by an external flood exposure using an additional light source were, in a first demonstration, a microscope LED ring illumination (SCHOTT, VisiLED ring light S80-55 BF) was employed. In this case, the intensity inside the overlapping area is sufficient to start writing of the SWW which is initialized from both fiber ends. As the SWW creates itself along the path of maximal intensity, it establishes a rigid optical interconnect between both fibers as long as the external light source is switched on. As we utilized different excitation wavelengths compared to common SWW fabrication processes which typically require UV light, we adapted the employed monomer resin. Here, we utilized a monomer mixture consisting of the UV-curing epoxy Syntholux (Synthopol, Buxtehude, Germany) and 3 wt.-% 2,3-butanedione (Sigma-Aldrich, Taufkirchen, Germany) which serves as UV-sensitive photo initiator.

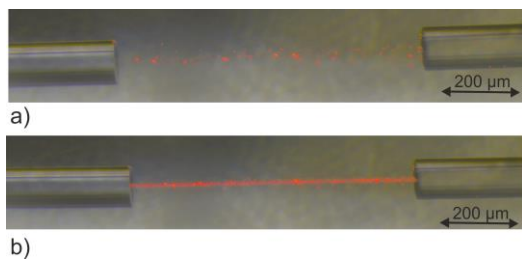


Figure 5.69: Microscope image of two-wavelength SWW: (a) before initiation and (b) after completion of the writing process (from [E 1]).

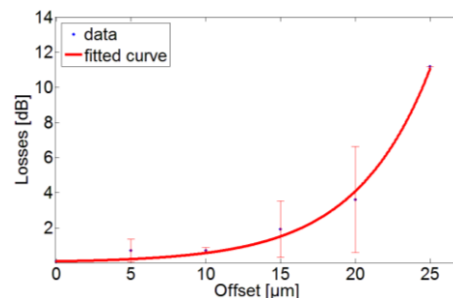


Figure 5.70: Loss measurements for different offsets d between the optical axes of two fibers (from [E 1]).

Figure 5.70 shows a microscope image of coherent radiation ($\lambda = 650 \text{ nm}$) being launched from two fiber tips into the liquid monomer resin (a) forming an SWW as soon as the external trigger light source is switched on (b). To investigate self-aligned SWW interconnects systematically, we created interconnects for various offsets between the optical axes of the two fibers and measured the optical losses. Measurement results are presented in Figure 5.70 and reveal that losses are as low as 3 dB for offsets of up to $20 \mu\text{m}$. Since such position accuracies are easily achieved by commonly used pick-and-place machines, our coupling structures are compatible with commonly used manufacturing processes. In addition, we also utilized SWWs to create interconnects between LDs and hot embossed waveguides, as shown in Figure 5.71 (for details see [E 1]). The hot embossed waveguides consist of a PMMA substrate and a NOA 68 core with rectangular cross section with dimensions of $25 \times 25 \mu\text{m}^2$ and were fabricated as described in Section 5.2.2. We used standard

bare LD chips (LD chip-650-P5, Roithner Lasertechnik, Austria) as light sources which were connected to a FR4 circuit board through eutectic bonding (provided by Yixiau Wang, Institute of Transport and Automation Technology, Leibniz University Hannover, Germany). The position between the LD and the waveguide was carried out on a mechanical five axis positioning stage which provides a position accuracy less than that of standard pick-and-place automates. The established interconnects using SWW automatically compensated for misalignment significantly enhancing coupling losses. Images of an SWW interconnect are shown in Figure 5.71.

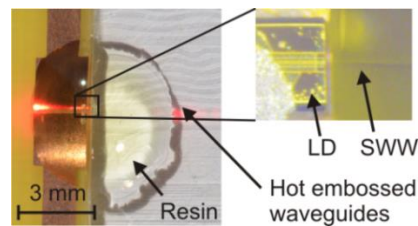


Figure 5.71: Image of the SWW interconnect between an LD and a hot embossed waveguide (from [E 1]).

5.4.4 Optical Transfer Line

Commonly, PICs include optical transfer lines consisting of waveguides, light sources and detectors. Crucial optical elements are coupling structures to transfer light from light sources to waveguides and eventually to photodetectors (PDs). Especially when utilizing high throughput manufacturing techniques, coupling structures need to be created in a cost efficient and fast manner. In this work, we utilized the previously described methods to fabricate two different transfer lines. The first line is based on fully polymer-based waveguides while light sources and detectors are based on semiconductor materials. The second line is completely based on polymer components taking advantage of organic light emitting diodes (OLEDs) and organic photodetectors (OPDs) such as the ones described in [110], [111].

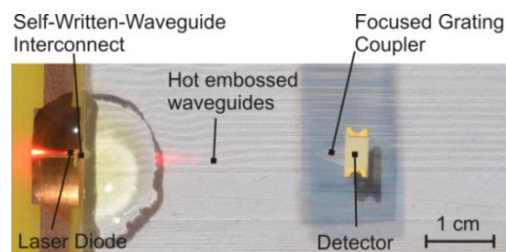


Figure 5.72: Image of transmission line using a SWW interconnect and semiconductor based detector (HOT 2016, unpublished).

A photograph of the hybrid semiconductor-polymer-based transition line is shown in Figure 5.72. Light source and coupling structure are the LD and SWW interconnect as described in Section 5.4.3. For out-coupling of light, we utilized focusing grating couplers including taper structures also described in Section 5.4.3. As detector, we employed commercially available SMD photodiodes (SFH 2701, Osram, Germany) which were positioned manually on the taper region under a microscope

and fixated by adhesive bonding (Supraflex). Total losses of the whole transmission line including coupling losses of the SWW interconnect, grating coupler induced losses as well as waveguide losses were determined experimentally and amount to 7.9 dB. In addition to optical losses, the transmission line is limited by the cut-off frequency of the waveguide which is determined by signal distortion due to modal or material dispersion among others. To calculate the cut-off frequency, we recorded eye patterns as shown in Figure 5.73.

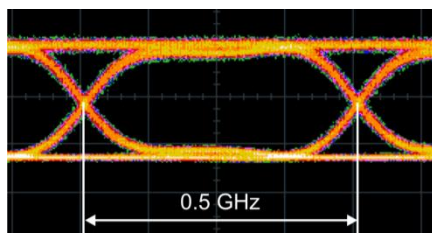


Figure 5.73: Eye pattern measured using hot embossed multimode waveguides (HOT 2016, unpublished).

From the eye pattern we can deduce that the cut-off frequency of the waveguides is approximately 0.25 GHz. The cut-off frequency was determined from the width of the X-shaped intersection of the rising and falling flanks, which is observable in Figure 5.73. According to Equation (4.13), the number of propagating modes inside the waveguide amounts to approximately 400 and, hence, the frequency limit is mainly due to modal dispersion.

In specific applications such as medical sensing, metal components are to be avoided. Therefore, we also aimed at the fabrication of fully polymer based transmission lines. These are also based on hot embossed waveguides integrated in a PMMA substrate. As described previously, as light source and detector OLEDs and OPD were integrated on the polymer substrate as shown in Figure 5.74. The integration of OLEDs and OPDs on our waveguide structures was carried out at the Institut für Hochfrequenztechnik (IHF) at Technical University Braunschweig.

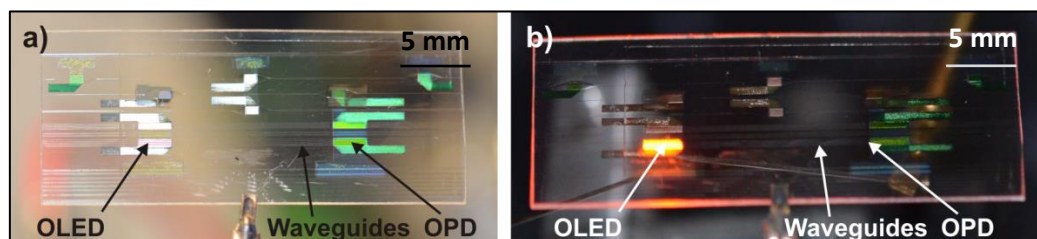


Figure 5.74: Photographs of the fully polymer based transition line: a) without electrical contacts; b) with connected and operated OLED (HOT 2016, unpublished).

Since OLEDs and OPDs are highly sensitive to environmental influences such as oxygen content of the surrounding atmosphere, they degrade rapidly and a comprehensive optical characterization was not feasible at the current stage. However, future work will focus on the fabrication of protection layers which will enable the use of the transmission line in air environment.

5.5 Integrated Polymer Sensor Devices

5.5.1 Overview

Polymers have become a widely used material class for sensing applications. Various sensor concepts were developed taking advantage of inherent polymer properties such as temperature sensitivity or elasticity. However, most sensor concepts were directly adapted from silicon photonics or telecommunication technology including, for example, fiber-Bragg-grating (FBG) sensors [112]. Applications for FBG sensors are broad and, thus, they have become a powerful tool in areas such as structural health monitoring (SHM) to measure temperature, strain and also humidity [E 9], [72]. Recent trends are also leading towards polymer sensors and also sensing elements integrated in thin polymer-based PLCs [113]. Such sensor foils were most often developed for the use in biomedical applications such as heart beat monitoring or artificial skin [113]. Strain sensors integrated in thin polymer foils based on Bragg gratings were also presented and were fabricated by means of NIL [69]. The grating was fabricated using ion beam writing and the resulting microstructure was replicated in PDMS subsequently. The PDMS copy was used as NIL stamp to create a waveguide trench with an integrated Bragg grating at the bottom of the waveguide. In [114], strain sensors based on Bragg gratings integrated in waveguides are reported which exhibit a sensitivity of $2.5 \text{ pm}/\mu\epsilon$. However, advantages of Bragg grating sensors are their simple structure and potential to be fabricated at a high-throughput level. However, they require cost-intensive equipment such as highly sensitive spectrometers for optical read-out. To counterbalance these drawbacks, arrayed-waveguide gratings (AWG) were developed which rely on two multimode interference (MMI) couplers being connected by an array of singlemode waveguides of different but defined lengths. Interference between light which is launched into the free propagation zone of the second MMI leads to an optical signal as several singlemode waveguides serving as optical read-outs. Due to the interference, the intensity distribution between these waveguides directly relates to the spectrum of light being incident on the first MMI. Such spectrometers were also developed for a center wavelength of 850 nm and fabricated on thin polymer films inOrmocere hybrid polymers [13]. Also, spectrometers were created utilizing hot embossing. Examples of such devices are based on a diffractive structure which is operated in reflection and splits light into its spectral components [34]. To avoid cost-intensive equipment such as spectrometers, alternative concepts for strain sensors were developed including ring resonators. Here, the coupling efficiency between a ring resonator with a diameter of $100 \mu\text{m}$ to $500 \mu\text{m}$ and a straight singlemode waveguide is altered if strain is applied to the PDMS substrate of the sensor. Therefore, the intensity of the transmitted wave correlates to the strain value and sensitivities of $0.3 \cdot 10^{-3} \text{ nm}/\mu\epsilon$ were achieved. Also, ring resonators are prominent examples in biochemical sensing [115]. But also other interferometric methods such as Mach-Zehnder interferometers were utilized as sensors and even integrated in thin polymer foils to measure refractive indices [14]. Detection limits of $3 \cdot 10^{-3}$ were achieved when determining the refractive index difference between a liquid sample medium, which is applied to the sample arm compared to the reference arm. Integrated polymer-based sensor devices for

biochemical analysis also often include microfluidic structures. A comprehensive description of such devices is given in [61].

In this work, we present two waveguide based sensors which are designed to be integrated in thin polymer foils. The first approach focuses on the detection of large strains compared to those measured by, e.g., Bragg grating based sensors. In addition, our approach is in principle capable of measuring 2-D strains and discriminates pure strain from tilt. The other approach is based on Bragg sensors which are inscribed into hot embossed waveguides through ns-laser radiation.

The results presented in this section are partially based on publications [E 9], [E 10], [E 11], [E 14].

5.5.2 Deformation/Strain Sensing

We developed a deformation sensor for measuring displacements in the range a few hundred microns as well as tilts [E 14]. The sensor consists of two arrays of five adjacent and linear waveguides exhibiting the same cross sections and diameters which face each other as shown in Figure 5.75(a). There exists a spacing of size $s = l_0 + \Delta l$ between both waveguide arrays where l_0 and Δl determine the initial separation between both arrays and the separation change under deformation, respectively.

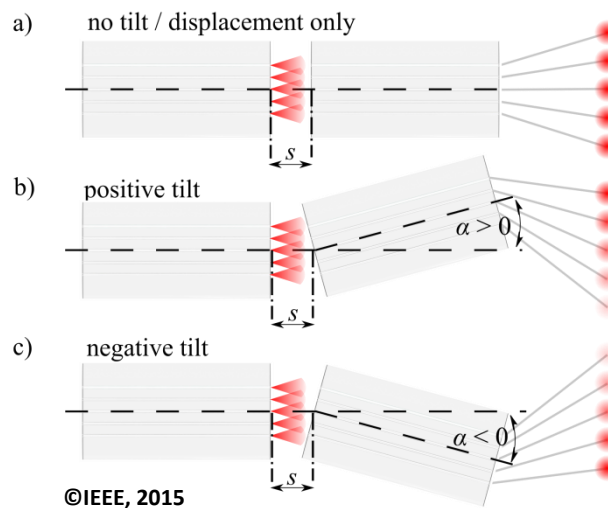


Figure 5.75: Principle of separation between tilt and displacement. Without tilt, the sensor signal shows uniform intensity in all five channels (a). With tilt in positive (b) or negative (c) direction, the five channels measure a sloped intensity distribution, as indicated by the different intensities of the red dots (from [E 14]).

As can be seen in Figure 5.75(a), the left array serves as emitter for light while the right array is the receiver unit. A great advantage of the sensor principle is its independence on the state of coherence or polarization of the light source. The spacing between the arrays forms a free propagation zone for light being launched into the spacing area. Due to the fixed NA of each waveguide, light forms a cone behind the emitter waveguide and, hence, the intensity which

couples into the opposing waveguide is dependent on the spacing s and the lateral position between both.

Figure 5.75 illustrates different deformation states which are distinguishable by the sensor: In the presence of a pure shift along the optical axis of the waveguides, the measured intensity at the exit ports of the five waveguides exhibits a uniform decrease or increase of the transmitted intensities (Figure 5.75(a)) depending on the direction and magnitude of motion. In case of a tilt α , as shown in Figure 5.75(b) and Figure 5.75(c), the intensity at the exit ports of the waveguides decreases continuously depending on the magnitude and direction of tilt. Note, a lateral shift perpendicular to the optical axes of the waveguides cannot be resolved and distinguished from a pure change in Δl . However, discrimination of such movements can be resolved by utilizing one launching fiber and two receiving fibers, which are capable of determining the direction of motion as also proposed in [116] for fiber based endoscopic sensors.

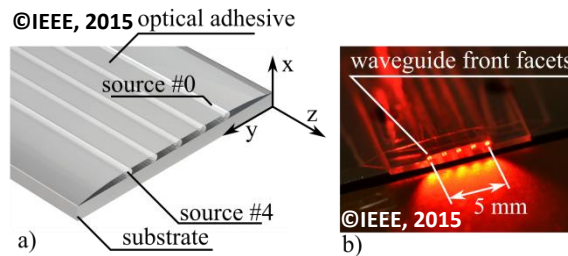


Figure 5.76: (a) Rendered image of the sensor, fibers are positioned on a flat substrate, covered by optical adhesive, (b) assembled emitter of the detector on a test setup (from [E 14]).

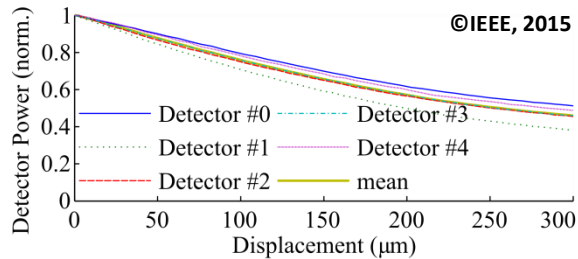


Figure 5.77: Measured normalized detector intensity with respect to displacement. Only a slight deviation of the detected coupled power from the average value is found (from [E 14]).

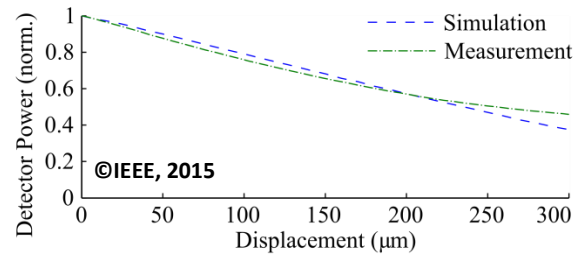


Figure 5.78: Comparison of simulated and measured detector power using the prototype. Both datasets are normalized to their maximum value (at $s = 0$ mm) - (from [E 14]).

The experimental realization of the sensor concept is shown in Figure 5.76. It was built from ESKA acrylic POF with a fiber diameter of $250 \mu\text{m}$ and a core diameter of $240 \mu\text{m}$. The fibers were fixated on a Plexiglas XT (Thyssen Krupp, Germany) PMMA substrate through adhesive bonding using NOA 68 (Norland, USA) optical adhesive. Five SMD LEDs (Kingbright KPHCM-2012SURCK) and five BPW34 photodiodes (Osram, Germany) serve as light sources and detectors, respectively. Prior to fabrication, the sensor design was simulated through ray tracing using the commercially available

optical design software ZEMAX™ and optimized with respect to geometry and refractive indices of the involved materials (see [E 14]).

The results of ray tracing simulations for a constant displacement Δl are exemplarily shown in Figure 5.77, which reveals that the intensity decreases constantly at all fiber exit ports (detector #0 to #4) as the displacement increases. As can be seen in Figure 5.78, the simulations agree well with the experimentally obtained results given for a single emitter-receiver fiber pair.

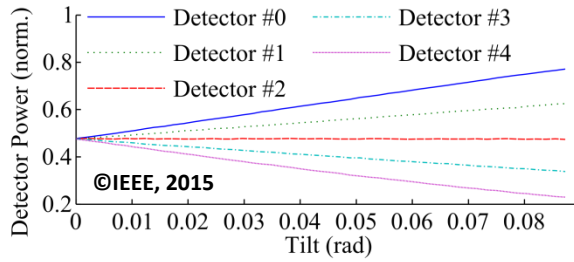


Figure 5.79: Simulated deviation of detector intensities from average value with respect to tilt angle. The displacement is held constant at $s = 0.2$ mm (from [E 14]).

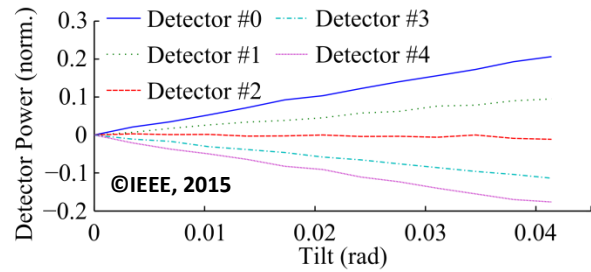


Figure 5.80: Measurement of the deviation of detector intensities from average with respect to tilt angle. The displacement is held constant at $s = 220$ μm (from [E 14]).

The simulated and experimentally observed sensor response for a tilt angle α is shown in Figure 5.79 and Figure 5.80, respectively. Both theory and experiment are in good agreement and show a linear evolution of the intensity at the exit ports as the tilt angle increases. However, the intensity gradient as well as the sign of the change in the detected power at each waveguide differ from each other and, hence, can directly be related to the tilt direction. In summary, the measurements in [E 14] yielded sensitivities of 8.19 mV/ μm and 72.04 mV/mrad for displacement and tilt, respectively.

5.5.3 Integrated Fiber Bragg Grating Sensors

If measurands such as temperature, displacements or strain are to be determined, an established approach in fiber optics is based on Bragg gratings which are incorporated inside the core of an optical fiber. This concept is directly transferable to waveguide-based integrated photonics. In analogy to fiber optics, we created Bragg gratings in hot embossed waveguides fabricated in PMMA substrates with a thickness of 375 μm using NOA 68 as core material (see Section 5.2.2).

The basic sensor concept is sketched in Figure 5.81. It consists of a waveguide with a refractive index n_{core} which is embedded in a polymer substrate with a refractive index n_{cladding} . In addition, the core region contains a grating region with periodically alternating refractive indices at a period Λ . The Bragg grating acts as a filter on the transmitted light spectrum with a Bragg wavelength

$$\lambda_B = 2 n_{\text{eff}} \Lambda \quad \text{and} \quad \Delta\lambda_B = \lambda_B \left(\alpha + \frac{1}{n} \frac{\partial n}{\partial T} \right) \Delta T. \quad (5.4)$$

Here, n_{eff} is the effective refractive index and $\Delta\lambda$ is the shift of the Bragg wavelength due to a temperature change ΔT . Note, in general Bragg sensors are sensitive to various environmental influences which alter n_{eff} or/and Λ . Here, we focus exemplarily on a Bragg shift $\Delta\lambda$ due to temperature effects, which are readily described by the thermal expansion coefficient α and the thermos-optic coefficient $\partial n / \partial T$.

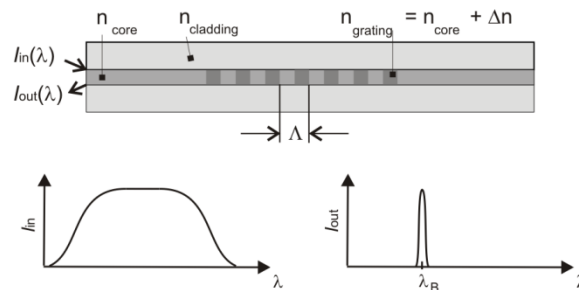


Figure 5.81: Sketch of a cross section of a waveguide-based Bragg grating sensor with a periodic refractive index modulation inside the core region and its influence on a broadband light spectrum in reflection mode.

For fabrication of the Bragg sensor, we utilized an Atlex FBG (ATL, Germany) krypton fluoride excimer laser operated at a wavelength of 254 nm to inscribe gratings into the hot embossed multimode waveguides described in Section 5.2.2. To achieve a grating period which is optimized for $\lambda_B \approx 550$ nm, we used a phase mask with a periodic phase grating (Ipsen Photonics, Denmark) with a grating period of 360 nm. The phase mask was in contact with the planar waveguide such that the core surface was facing the phase mask during grating fabrication. Subsequently, we exposed the sample to the excimer radiation for 60 seconds utilizing a pulse duration of 8 ns, a pulse energy of 5 mJ and a repetition rate of 50 Hz.

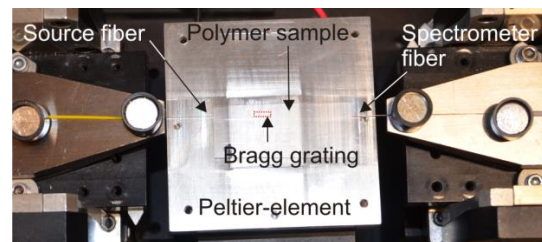


Figure 5.82: Experimental setup to determine the spectral response as function of temperature of the waveguide-based FBG (HOT 2016, unpublished).

After fabrication, the sensor was placed onto a Peltier element which was located between two alloy plates with a thickness of 5 mm as shown in Figure 5.82. Two multimode fibers with a core diameter of 50 μm were used to launch light from a LED white light source (MCWHF2, Thorlabs) into the sample and to collect the transmitted light, respectively. The transmitted light was then analyzed using a spectrometer (Avaspec-3648) as the temperature of the Peltier element was constantly increased. The temperature was monitored by an optical IR thermometer (IR 260-8S, Voltkraft). Measured transmission spectra for various temperatures are shown in Figure 5.83(a). To obtain the sensor response, we determined the Bragg wavelength λ_B from the characteristic

minima of the spectral dip for each temperature. The Bragg wavelength as function of temperature is shown in Figure 5.83(b) which exhibits a linear dependence.

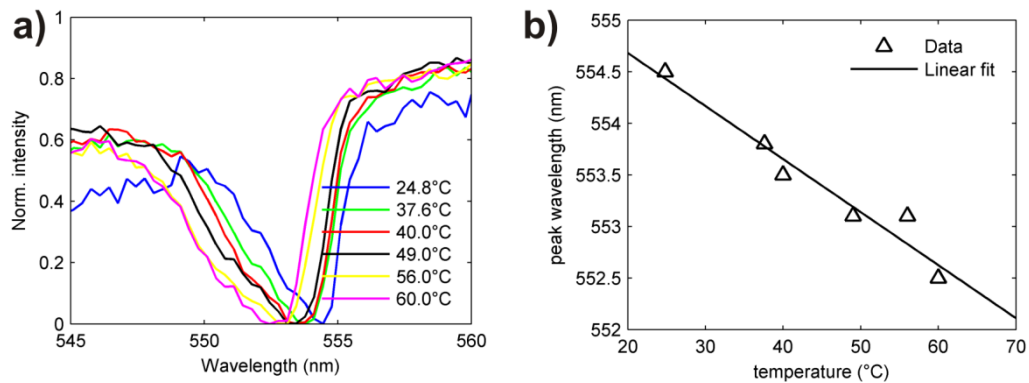


Figure 5.83: Temperature response of the FBG: a) Measured spectra for different temperatures; b) Shift of the spectral minimum as function of temperature (HOT 2016, unpublished).

The sensor sensitivity was determined from the gradient of a linear least-squares-fit to the measurement data and reads -51.4 pmK^{-1} . Thus, the sensitivity is of the same magnitude as for PMMA based fiber Bragg grating sensors which are reported in the literature.

6 Summary

Polymer based integrated photonics is emerging as a key technology for various applications in areas as broad as telecommunication, optical micro-processing and, in particular, optical sensing enabling highly sensitive measurements of thermal and mechanical properties as well as of concentration of biochemical analytes. Especially planar systems based on integrated waveguides are of interest as they provide a high potential to be fabricated by high throughput manufacturing techniques and may substitute electronic components in some areas. A great advantage of polymers-based compared to semiconductor-based integrated photonics is their low fabrication cost. However, polymer-based planar lightwave circuits (PLCs) require not only the fabrication of waveguides but also strategies to integrate various optical components into thin polymer PLCs such as light sources and detectors to enable full transmission lines or novel sensor concepts. In this work, we focused particularly on the development of potential reel-to-reel compatible fabrication technologies to create waveguides and coupling structures in thin PLCs with thicknesses down to 50 μm . In addition, we discuss the implication of these technologies on the fabrication of micro and diffractive optics as well as present the recent results. The contributions and results of this work can be summarized as follows:

- **Characterization of integrated photonics:**

First, we demonstrated methods for 2-D and 3-D characterization of integrated polymer photonics using confocal microscopy and optical coherence tomography. The emphasis was placed on novel calibration strategies which were developed based on numerical simulations of the imaging properties of both devices. By identifying optical artefacts, we set the theoretical basis to achieve an increase in measurement accuracy of up to several 100 nm in confocal microscopy. Also, calibration strategies and standards are introduced for the use of optical coherence tomography as volumetric measurement device. Secondly, we used optical coherence tomography to establish novel methods for refractive index n and scattering coefficient μ_s measurements. Measurement results were demonstrated on polymers but also biological tissue. We achieved an accuracy of ± 0.04 even in highly scattering biological tissue such as bone. Also, we present a phase retrieval algorithms to determine phase changes introduced by transparent polymer samples. Using this approach, we studied phase changes induced by fs-laser written grating structures in polymers.

- **Fabrication of polymer-based integrated photonics:**

We developed three different types of processes for waveguide fabrication: 1) A hot embossing process to structure polymer substrates followed by a doctor blading process to apply a core monomer; 2) A novel reactive lamination process utilizing a reactive lamination agent developed at the University of Freiburg, Germany, which enables the formation of a rigid bond between chemically incompatible materials used as core and cladding material, respectively; 3) A maskless lithography setup was developed and optimized to create

polymer-based photonic components and multi-level diffractive optical elements in polymers. The versatility of the approach was demonstrated by also creating holograms and diffractive optical elements in photoresists which were transferred to polymers but also sheet metals subsequently.

Polymer-based multimode waveguides were realized with propagation losses as low as 0.09 dB/cm and 0.79 dB/cm for wavelengths of 850 nm and 650 nm, respectively.

- **Optical Design:**

We introduced an optical simulation method to design diffractive optical elements integrated into freeform surfaces of macroscopic objects, as well as a corresponding process chains to fabricate these structures using soft-stamp hot embossing and deep drawing. For the design, we simulated material flow during fabrication and also took the influence of the workpiece deformation during the optical design into account. These approaches and methods lend themselves for the design and fabrication of complex integrated photonic elements based on diffractive optical components.

- **Design and fabrication of coupling structures for PLCs:**

Coupling structures were designed based on micromirror and grating couplers with the purpose to integrate light sources and detectors. In addition, we optimized and fabricated waveguide-based beam splitters to distribute light inside PLCs. Fabrication processes which are especially suited to create coupling structures based on hot embossing and which are easily transferable to reel-to-reel processes were investigated. In addition, we present a method to establish rigid optical links between embedded waveguides and laser diodes using self-written waveguides which automatically compensate for misalignment between optical components. To demonstrate the capability of the coupling structures and fabrication methods, we created two different transmission lines comprising of semiconductor-based and fully organic material-based light sources and photodetectors, respectively. The transmission lines consist of waveguides and coupling structures which were fabricated through the investigated methods. Total transmission losses were achieved which are as low as 7.9 dB.

- **Design and fabrication of deformation/strain and temperature sensors in PLCs:**

A novel concept of an arrayed waveguide-based displacement and tilt sensor was introduced and fabricated utilizing an adhesive bonding process. Following optimization based on optical simulation, we achieved sensor sensitivities of 8.19 mV/ μm and 72.04 mV/mrad for displacement and tilt, respectively. In addition, we fabricated Bragg grating based temperature sensors in hot embossed multimode waveguides by ns-laser pulses. The achieved sensitivity was as high as -51.4 pmK^{-1} .

7 Zusammenfassung

Polymerbasierte integrierte Photonik ist eine aufstrebende Schlüsseltechnologie, die sich in den letzten Jahren zunehmend in einer Vielzahl von Anwendungen etabliert, wie beispielsweise der Telekommunikation, der optischen Mikroprozessortechnologie, aber auch der optischen Sensorik und hier das Messen von Temperatur, mechanischen Größen, aber auch von biochemisch relevanten Analytkonzentrationen erlaubt. Insbesondere planare Systeme, die auf integrierten Wellenleitern basieren, spielen in diesem Kontext eine entscheidende Rolle, da sie potenziell durch durchsatzstarke Herstellungsverfahren produziert werden können und hierdurch in einigen Bereichen vollständig elektronische Systeme verdrängen könnten. Ein entscheidender Vorteil polymerbasierter photonischer Elemente gegenüber halbleiterbasierten Technologien sind deutlich geringere Herstellungskosten. Zur Herstellung komplexer, planarer und optischer Schaltkreise (PLCs – engl. für planar lightwave circuits) sind jedoch nicht nur die Herstellung von Wellenleitern sondern auch Strategien zur Integration von einer Vielzahl von optischen Komponenten in dünne Polymerfolien erforderlich. Beispiele solcher Komponenten sind Lichtquellen und Detektoren, die die Grundlage für optische Übertragungstrecken bis hin zu neuartigen Sensorkonzepten bilden.

Der Fokus dieser Arbeit liegt daher insbesondere auf der Erforschung und Entwicklung von Rolle-zu-Rolle fähigen Herstellungstechnologien, um Wellenleiter und Koppelstrukturen in dünnen Polymerfolien-PLCs mit Substratdicken zwischen 50 μm und 500 μm zu realisieren. Weiterhin werden Anwendungen der erforschten Technologien im Bereich diffraktiver optischer Elemente diskutiert und durch experimentelle Ergebnisse demonstriert. Die wesentlichen Ergebnisse dieser Arbeit lassen sich in folgenden Punkten zusammenfassen:

- **Charakterisierung integrierter Photonik**

Die konfokale Mikroskopie und Optische Kohärenztomographie (OCT) eignen sich für 2-D topographische und 3-D volumetrische Messungen integrierter Polymerphotonik. Der Beitrag dieser Arbeit liegt dabei insbesondere im Bereich der Entwicklung neuer Kalibrierstrategien für diese Messtechniken, die auf numerischen Simulationen der Abbildungseigenschaften beider Systeme beruhen. Durch die Identifikation von Messabweichungen aufgrund optischer Abbildungseigenschaften der Messsysteme wurde die Grundlage gelegt, die Messgenauigkeit der Systeme um mehrere 100 nm zu verbessern. Weiterhin konnten wir auf OCT basierende Methoden entwickeln, um Brechungsindexverteilungen n und Streuparameter μ_s zu bestimmen. Systematische Messreihen an polymeren und biologischen Proben haben gezeigt, dass sich der Brechungsindex selbst in stark streuendem Knochengewebe mit einer Genauigkeit von ± 0.04 bestimmen lässt. Zusätzlich wurde ein Phase Retrieval Algorithmus eingeführt, um mittel fs-Laserstrahlung in Polymeren erzeugte, periodische Phasenobjekte zu charakterisieren.

- **Herstellung von polymerbasierter integrierter Photonik**

Im Bereich Prozesstechnologie liegt der Fokus dieser Arbeit auf drei verschiedenen Verfahren zur Herstellung optischer Wellenleiter in dünnen Polymerfolien, die direkt auf Rolle-zu-Rolle Herstellungsverfahren übertragbar sind: 1) ein Heißprägeprozess zur Strukturierung von Polymersubstraten in Kombination mit einem Rakelprozess, um Wellenleiterkernmaterial aufzutragen; 2) ein neuartiger Reaktivlaminierprozess, um chemisch inkompatible Kern und Mantelmaterialien mit Hilfe eines Reaktivmittels (entwickelt am IMTEK, Albert-Ludwigs-Universität Freiburg) fest verbinden zu können; 3) Prozesse basierend auf maskenloser Lithographie, um integrierte photonische Komponenten und mehrstufige diffraktive optische Elemente in Polymer zu erzeugen. Zusätzlich wurde ein maskenloser Lithographieprozess demonstriert, mittels dessen zunächst diffraktive optische Elemente und computergenerierte Hologramme in Photoresist erzeugt und anschließend auf Freiformflächen aus Polymer oder Dünnschicht übertragen werden können.

Mit Hilfe der erforschten Verfahren sind Wellenleiter realisiert worden, die geringe Dämpfungswerte bis zu 0.09 dB/cm und 0.79 dB/cm bei Wellenlängen von 850 nm and 650 nm aufweisen.

- **Optische Simulation:**

Im Rahmen dieser Arbeit wurde ein Verfahren entwickelt, um diffraktive optische Elemente auf Freiformoberflächen zu berechnen und eine entsprechende Prozesskette erforscht, um diese durch thermische soft-stamp Heißprägeverfahren in Polymer oder mittels Tiefziehen auf Blechwerkstoffen herzustellen. Während des optischen Designs wird zudem die Verformung des Werkstücks oder weichen Stempelmaterials mit in die Simulation einbezogen. Hierdurch eignet sich das Verfahren sowohl für das Design und die Herstellung komplexer photonischer Strukturen als auch diffraktiver optischer Elemente auf Freiformflächen.

- **Design und Herstellung von Koppelstrukturen für PLCs:**

In dieser Arbeit wurden Koppelstrukturen, basierend auf Mikrosiegeln und diffraktiven Gitterstrukturen, zur Ankopplung verschiedenster Lichtquellen und Detektoren an polymerbasierte PLCs erforscht. Zudem konnten wellenleiterbasierte Strahlteiler zur Verteilung von Licht innerhalb von PLCs simulativ optimiert und hergestellt werden. Ein weiterer Fokus dieser Arbeit lag auf der Erforschung von Rolle-zu-Rolle fähigen Heißprägeprozessen für die Herstellung solcher

Koppelstrukturen. Darüber hinaus wurde ein Verfahren erforscht, um eine mechanisch feste, optische Kopplung zwischen Laserdioden und eingebetteten Wellenleitern herzustellen. Das Verfahren basiert dabei auf selbstschreibenden Wellenleitern und kompensiert automatisch Positionierungsungenauigkeiten zwischen den zu verbindenden optischen Komponenten. Um das Potenzial der erforschten Koppelstrukturen und Herstellungsverfahren zu demonstrieren, wurden zwei Übertragungsstrecken geschaffen,

die auf heißgeprägten Wellenleitern in Foliensubstraten mit Schichtdicken von $375\ \mu\text{m}$ aufsetzen. Für die erste Übertragungsstrecke kamen halbleiterbasierte Lichtquellen und Detektoren zum Einsatz. Die zweite Übertragungsstrecke verwendet vollständig polymerbasierte organische Lichtquellen und Detektoren. Dabei wurden Übertragungsverluste im Gesamtsystem von $7.9\ \text{dB}$ erreicht.

▪ **Design und Herstellung von Abstands-, Dehnungs- und Temperatursensoren in PLCs:**

Es wurde ein neuartiges Konzept eines optischen Abstands- bzw. Dehnungssensors, basierend auf Wellenleiterarrays, erforscht. Aufgrund der Wellenleiterkonfiguration ist der Sensor in der Lage, zwischen einer Abstandsänderung und einer relativen Verkippung zu unterscheiden. Der Sensor wurde mittels adhäsiven Bondverfahren hergestellt. Durch eine auf optischer Simulation basierende Optimierung wurde eine Sensitivität von $8.19\ \text{mV}/\mu\text{m}$ bei Abstandsänderungen $72.04\ \text{mV}/\text{mrad}$ für eine Verkippung sowohl theoretisch als auch experimentell erreicht. Weiterhin sind Temperatursensoren in heißgeprägten Wellenleitern realisiert worden, die auf Bragg-Gitter aufsetzen und mittels Laserpulsen mit Pulsdauern im Nanosekundenbereich im Wellenleiterkern erzeugt wurden. Die experimentell bestimmte Sensitivität des Sensors betrug $51.4\ \text{pmK}^{-1}$.

8 References

- [1] P. Dong, Y.-K. Chen, G.-H. Duan, and D. T. Neilson, Silicon photonic devices and integrated circuits, *Nanophotonics* **3**, 215–228 (2014).
- [2] X. C. Tong, *Advanced Materials for Integrated Optical Waveguides* (Springer, 2014).
- [3] V. R. Almeida, C. A. Barrios, R. R. Panepucci, and M. Lipson, All-optical control of light on a silicon chip, *Nature* **431**, 1081–1084 (2004).
- [4] R. D. L. Rue, H. Chong, M. Gnan, N. Johnson, I. Ntakis, P. Pottier, M. Sorel, A. M. Zain, H. Zhang, E. Camargo, C. Jin, M. Armenise, and C. Ciminelli, Photonic crystal and photonic wire nano-photonics based on silicon-on-insulator, *New J. Phys.* **8**, 256 (2006).
- [5] R. Pool, All-optical communication comes of age, 12 march 2010, spie newsroom. doi: 10.1117/2.2201003.01, .
- [6] D. Dai, J. Bauters, and J. E. Bowers, Passive technologies for future large-scale photonic integrated circuits on silicon: polarization handling, light non-reciprocity and loss reduction, *Light Sci. Appl.* **1**, e1– (2012).
- [7] C. Zhang, S. Zhang, J. D. Peters, and J. E. Bowers, 8 8 40 gbps fully integrated silicon photonic network on chip, *Optica* **3**, 785–786 (2016).
- [8] C. Sun, M. T. Wade, Y. Lee, J. S. Orcutt, L. Alloatti, M. S. Georgas, A. S. Waterman, J. M. Shainline, R. R. Avizienis, S. Lin, B. R. Moss, R. Kumar, F. Pavanello, A. H. Atabaki, H. M. Cook, A. J. Ou, J. C. Leu, Y.-H. Chen, K. Asanovi, R. J. Ram, M. A. Popovi, and V. M. Stojanovic, V., Single-chip microprocessor that communicates directly using light, *Nature* **528**, 534–538 (2015).
- [9] S. Bäumer, ed., *Handbook of Plastic Optics* (Wiley-VCH, 2005).
- [10] H. Ma, A. K.-Y. Jen, and L. R. Dalton, Polymer-based optical waveguides: Materials, processing, and devices, *Adv. Mater.* **14**, 1339–1365 (2002).
- [11] H. Hamid, M. Neeli, T. Fickenscher, S. G. O’Keefe, and D. V. Thiel, Simple low-cost fabrication method of a buried plastic optical waveguide for circuits in plastic interconnects, *Microw. Opt. Technol. Lett.* **55**, 1947–1950 (2013).
- [12] W. M. Pätzold, C. Reinhardt, A. Demircan, and U. Morgner, Cascaded-focus laser writing of low-loss waveguides in polymers, *Opt. Lett.* **41**, 1269–1272 (2016).
- [13] R. Orghici, K. Bethmann, U. Zywiets, C. Reinhardt, and W. Schade, All-polymer arrayed waveguide grating at 850nm: design, fabrication, and characterization, *Opt. Lett.* **41**, 3940–3943 (2016).
- [14] M. Hofmann, Y. Xiao, S. Sherman, U. Gleissner, T. Schmidt, and H. Zappe, Asymmetric mach-zehnder interferometers without an interaction window in polymer foils for refractive index sensing, *Appl. Opt.* **55**, 1124–1131 (2016).
- [15] S. Aikio, J. Hiltunen, J. Hiitola-Keinänen, M. Hiltunen, V. Kontturi, S. Siitonen, J. Puustinen, and P. Karioja, Disposable photonic integrated circuits for evanescent wave sensors by ultra-high volume roll-to-roll method, *Opt. Express* **24**, 2527–2541 (2016).
- [16] B. Saleh and M. Teich, *Fundamentals of Photonics* (Wiley, 2007), 2nd ed.
- [17] M. Born and E. Wolf, *Principles of Optics* (Cambridge University Press, Cambridge, 1999), 7th ed.
- [18] J. D. Jackson, *Klassische Elektrodynamik* (de Gruyter, 2006), 4th ed.
- [19] F. Mitschke, *Fiber Optics* (Springer, 2009).

- [20] K. Okamoto, *Fundamentals of optical waveguides* (Elsevier, 2006), 2nd ed.
- [21] S. A. Maier, *Plasmonics: fundamentals and applications* (Springer, 2007).
- [22] H. Zappe, *Fundamentals of Micro-optics* (Cambridge University Press, 2010).
- [23] M. Kuznetsov, Radiation losses in dielectric waveguide y-branch structures, *J. Lightwave Technol.* **3**, 674–677 (1985).
- [24] A. Yariv and P. Yeh, *Photonics* (Oxford University Press, 2007), 6th ed.
- [25] R. G. Hunsperger, *Integrated Optics* (Springer, 2009).
- [26] B. Wohlfeil, Integrated fiber grating couplers in silicon photonics, Ph.D. thesis, TU Berlin (2015).
- [27] D. M. Mattox, Chapter 1 - introduction, in *Handbook of Physical Vapor Deposition (PVD) Processing (Second Edition)*, D. M. Mattox, ed. (William Andrew Publishing, Boston, 2010), pp. 1 – 24, second edition ed.
- [28] F. Vand T. Zetterer, *Einführung in die Mikrosystemtechnik* (Vieweg, 2000).
- [29] N. N., memsnet.org, retrieved sep., 22nd 2016, .
- [30] F. Gao, S. Ylinen, M. Kainlauri, and M. Kapulainen, Smooth silicon sidewall etching for waveguide structures using a modified bosch process, *J. Micro/Nanolith. MEMS MOEMS.* **13**, 013010 (2014).
- [31] M. Worgull, *Hot Embossing - Theory and Technology of Microreplication* (William Andrew, 2009).
- [32] R. Srinivasan and B. Braren, Ultraviolet laser ablation of organic polymers, *Chem. Rev.* **89**, 1303–1316 (1989).
- [33] J. G. Lunney and R. Jordan, Pulsed laser ablation of metals, *Appl. Surf. Sci.* **127**, 941 – 946 (1998).
- [34] H. Herzig, ed., *Micro-optics: Elements, systems and applications* (Taylor&Trancis, 1997).
- [35] R. Hull, T. Chraska, Y. Liu, and D. Longo, Microcontact printing: new mastering and transfer techniques for high throughput, resolution and depth of focus, *Mater. Sci. Eng. C* (2002).
- [36] T. Baehr-Jones, A. Spott, R. Ilic, A. Spott, B. Penkov, W. Asher, and M. Hochberg, Silicon-on-sapphire integrated waveguides for the mid-infrared, *Opt. Express* **18**, 12127–12135 (2010).
- [37] N. Carlie, J. D. Musgraves, B. Zdyrko, I. Luzinov, J. Hu, V. Singh, A. Agarwal, L. C. Kimerling, A. Canciamilla, F. Morichetti, A. Melloni, and K. Richardson, Integrated chalcogenide waveguide resonators for mid-ir sensing: leveraging material properties to meet fabrication challenges, *Opt. Express* **18**, 26728–26743 (2010).
- [38] M. Kutz, ed., *Handbook of Materials Selection* (Wiley, 2002).
- [39] N. N., Epocore & epoclad serien, <http://www.microresist.de/de/produktwelt/negative-photoresiste/uv-lithographie/epocore-epoclad-serien>, retrieved on August 15, 2016.
- [40] N. N., Topas data sheet, http://www.topas.com/sites/default/files/TDS_8007S_04_e_1.pdf, I retrieved August 15, 2016.
- [41] M. Rahlves, Confocal microscope in 3d metrology, Ph.D. thesis, Leibniz University Hannover (2011).
- [42] J. E. Mark, ed., *Physical Properties of Polymers Handbook* (Springer, 2007).
- [43] L. Eldada and L. W. Shacklette, Advances in polymer integrated optics, *IEEE J. Sel. Top. Quantum Electron.* **6**, 54–68 (2000).

- [44] D. W. van Krevelen and K. te Nijenhuis, *Properties of Polymers: Their Correlation with Chemical Structure; Their Numerical Estimation and Prediction from Additive Group Contributions* (Elsevier, 2009).
- [45] N. N., Cytop data sheet, <http://www.agcce.com/cytop-technical-information/>, retrieved August 15, 2016.
- [46] V. V. Tuchin, Light scattering study of tissues, *Physics-Uspekhi* **40**, 495 (1997).
- [47] G. L. Pedrola, *Beam Propagation Method for Design of optical Waveguide Devices* (Wiley, 2015).
- [48] D. A. P. M. G. Moharam, E. B. Grann and T. K. Gaylord., Formulation for stable and efficient implementation of the rigorous coupled-wave analysis of binary gratings, *J. Opt. Soc. Am. A* **12**, 1068–1076 (1995).
- [49] M. G. Moharam, D. A. Pommet, E. B. Grann, and T. K. Gaylord, Stable implementation of the rigorous coupled-wave analysis for surface-relief gratings: enhanced transmittance matrix approach, *JOSA A* pp. 1077–1086 (1995).
- [50] E. Popov, M. Nevière, B. Gralak, and G. Tayeb, Staircase approximation validity for arbitrary-shaped gratings, *J. Opt. Soc. Am. A* **19**, 33–42 (2002).
- [51] A. V. Lavrinenko, J. Lægsgaard, N. Gregersen, F. Schmidt, and T. Søndergaard, *Numerical Methods in Photonics* (CRC Press, 2014).
- [52] T. Rylander, Ingelström, and A. Bondeson, *Computational Electromagnetics* (Springer, 2013).
- [53] J. Zhu, S. K. Ozdemir, Y.-F. Xiao, L. H. L. Li, D.-R. Chen, and L. Yang, On-chip single nanoparticle detection and sizing by mode splitting in an ultrahigh-q microresonator, *Nat. Photon.* (2009).
- [54] A. Layadi, A. Vonsovici, R. Orobtcouk, D. Pascal, and A. Koster, Low-loss optical waveguide on standard soi/simox substrate, *Optics Comm.* **146**, 31 – 33 (1998).
- [55] S. K. Pani, C. C. Wong, and K. Sudharsanam, Variation of sidewall roughness of polymeric waveguides during reactive ion etching, *Appl. Phys. Lett.* **85**, 1295–1297 (2004).
- [56] J. F. Aguilar and E. R. Méndez, On the limitations of the confocal scanning optical microscope as a profilometer, *Journal of Modern Optics* **42**, 1785–1794 (1995).
- [57] W. Xie, P. Lehmann, and J. Niehues, Lateral resolution and transfer characteristics of vertical scanning white-light interferometers, *Appl. Opt.* **51**, 1795–1803 (2012).
- [58] P. Lehmann, Vertical scanning white-light interference microscopy on curved microstructures, *Opt. Lett.* **35**, 1768–1770 (2010).
- [59] H.-C. Cheng and Y.-C. Liu, Simultaneous measurement of group refractive index and thickness of optical samples using optical coherence tomography, *Appl. Opt.* **49**, 790–797 (2010).
- [60] N. Gisin, J. P. Pellaux, P. Stamp, N. Hori, and M. Masuyama, Alternative configuration for refracted near-field measurements of refractive index on glass-integrated-optics waveguides, *Appl. Opt.* **31**, 7108–7112 (1992).
- [61] E. Iannone, *Labs on Chip - Principles, Design, and Technology* (CRC Press, 2015).
- [62] K. R. McIntosh, G. Lau, J. N. Cotsell, K. Hanton, D. L. Bätzner, F. Bettiol, and B. S. Richards, Increase in external quantum efficiency of encapsulated silicon solar cells from a luminescent down-shifting layer, *Prog. photovolt.* **17**, 191–197 (2009).
- [63] C.-C. Tsui, H.-C. Wei, W.-F. Chang, and G.-D. J. Su, Design and fabrication of a mid-wavelength infrared fresnel lens via liquid poly(methyl methacrylate), *J. Micromech. Microeng.* **22**, 045010 (2012).

- [64] E. A. Genina, A. N. Bashkatov, and V. Tuchin, Optical clearing of cranial bone, *Adv. Opt. Technol.* **2008**, ID 267867 (2008).
- [65] M. W. Farn, New iterative algorithm for the design of phase-only gratings, (1991).
- [66] I. Papakonstantinou, K. Wang, D. R. Selviah, and F. A. Fernández, Transition, radiation and propagation loss in polymer multimode waveguide bends, *Opt. Express* **15**, 669–679 (2007).
- [67] A. Chen and E. Murphy, *Broadband Optical Modulators: Science, Technology, and Applications* (CRC, 2012).
- [68] G. D. Emmerson, S. P. Watts, C. B. E. Gawith, V. Albanis, M. Ibsen, R. B. Williams, and P. G. R. Smith, Fabrication of directly uv-written channel waveguides with simultaneously defined integral bragg gratings, *Electron. Lett.* **38**, 1–2 (2002). Copyright - Copyright The Institution of Engineering & Technology Nov 21, 2002; Dokumentbestandteil - Graphs; Diagrams; ; Zuletzt aktualisiert - 2015-03-31; CODEN - ELLEAK.
- [69] S. Sherman and H. Zappe, Printable bragg gratings for polymer-based temperature sensors, *Procedia Technology* **15**, 702 – 709 (2014).
- [70] M. Hecke, W. Bacher, T. Hanemann, and H. Ulrich, Hot embossing and injection molding for micro-optical components, (1997).
- [71] L. Li, T. W. Raasch, I. Sieber, E. Beckert, R. Steinkopf, U. Gengenbach, and A. Y. Yi, Fabrication of microinjection-molded miniature freeform alvarez lenses, *Appl. Opt.* **53**, 4248–4255 (2014).
- [72] X. Zhang, K. Liu, X. Shan, and Y. Liu, Roll-to-roll embossing of optical linear fresnel lens polymer film for solar concentration, *Opt. Express* **22**, A1835–A1842 (2014).
- [73] P. Krippner, J. Mohr, C. Mueller, and C. van der Sel, Microspectrometer for the infrared range, (1996).
- [74] C.-G. Choi, Fabrication of optical waveguides in thermosetting polymers using hot embossing, *J. Micromech. Microeng.* **14**, 945 (2004).
- [75] K. B. Y., C.-G. Choi, and S.-P. Han, Fabrication of multimode polymeric waveguides by hot embossing lithography, *Jpn. J. Appl. Phys.* **43**, 3450 (2004).
- [76] R. Bruck, P. Muellner, N. Kataeva, A. Koeck, S. Trassl, V. Rinnerbauer, K. Schmidegg, and R. Hainberger, Flexible thin-film polymer waveguides fabricated in an industrial roll-to-roll process, *Appl. Opt.* **52**, 4510–4514 (2013).
- [77] J. Missinne, S. Kalathimekkad, B. V. Hoe, E. Bosman, J. Vanfleteren, and G. V. Steenberge, Stretchable optical waveguides, *Opt. Express* **22**, 4168–4179 (2014).
- [78] C.-Y. Chang and M.-H. Tsai, Development of a continuous roll-to-roll processing system for mass production of plastic optical film, *J. Micromech. Microeng.* **25**, 125014 (2015).
- [79] P. K. Dey and P. Ganguly, A technical report on fabrication of su-8 optical waveguides, *J. Opt.* **43**, 79–83 (2014).
- [80] W.-S. Kim, J.-H. Lee, S.-Y. Shin, B.-S. Bae, and Y.-C. Kim, Fabrication of ridge waveguides by uv embossing and stamping of sol-gel hybrid materials, *IEEE Photon. Technol. Lett.* **16**, 1888–1890 (2004).
- [81] H. Mizuno, O. Sugihara, T. Kaino, N. Okamoto, and M. Hosino, Low-loss polymeric optical waveguides with large cores fabricated by hot embossing, *Opt. Lett.* **28**, 2378–2380 (2003).
- [82] P. Calvert, Inkjet printing for materials and devices, *Chem. Mat.* **13**, 3299–3305 (2001).
- [83] T. Reitberger, G.-A. Hoffmann, T. Wolfer, L. Overmeyer, and J. Franke, Printing polymer optical waveguides on conditioned transparent flexible foils by using the aerosol jet technology, (2016).

- [84] T. Wolfer, P. Bollgruen, D. Mager, L. Overmeyer, and J. G. Korvink, Flexographic and inkjet printing of polymer optical waveguides for fully integrated sensor systems, *Procedia Technology* **15**, 521 – 529 (2014).
- [85] W. H. Wong, K. S. Chan, and E. Y. B. Pun, Ultraviolet direct printing of rare-earth-doped polymer waveguide amplifiers, *Appl. Phys. Lett.* **87**, 011103 (2005).
- [86] G. D. Emmerson, C. B. E. Gawith, R. B. Williams, B. Richard, and P. G. R. Smith, Simultaneous direct uv writing of channel waveguide and bragg grating structures, (2004).
- [87] M. Koerdt, Fabrication and characterization of waveguide and grating structures induced by ultraviolet radiation in polymers with a shortened writing process, (2009).
- [88] S. Nolte, M. Will, J. Burghoff, and A. Tuennermann, Femtosecond waveguide writing: a new avenue to three-dimensional integrated optics, *Appl. Phys. A* **77**, 109–111 (2003).
- [89] K. Zhong, Y. Gao, F. Li, N. Luo, and W. Zhang, Fabrication of continuous relief micro-optic elements using real-time maskless lithography technique based on {DMD}, *Opt. Laser Technol.* **56**, 367 – 371 (2014).
- [90] K. Zhong, Y. Gao, F. Li, Z. Zhang, and N. Luo, Fabrication of {PDMS} microlens array by digital maskless grayscale lithography and replica molding technique, *Optik* **125**, 2413 – 2416 (2014).
- [91] A.-K. Schuler, R. Rother, O. Prucker, C. Müller, H. Reinecke, and J. Rühle, A novel reactive lamination process for the generation of functional multilayer foils for optical applications, *Procedia Technology* **15**, 147 – 155 (2014).
- [92] O. Ripoll, V. Kettunen, and H. P. Herzig, Review of iterative fourier-transform algorithms for beam shaping applications, *Opt. Eng.* **43**, 2549–2556 (2004).
- [93] J. W. Goodman, *Introduction to Fourier Optics* (Roberts & Company Publishers, 2005), 3rd ed.
- [94] V. Prajzler, R. Maštera, J. Špírková, and V. Jerábek, Compact multimode polymer optical 12 y splitters with large core planar waveguide, *J. Opt.* **43**, 310–316 (2014).
- [95] E. Zraggen, I. M. Soganci, H. Folkert, A. L. Porta, R. Dangel, B. J. Offrein, S. A. Snow, J. K. Young, B. W. Swatowski, C. M. Amb, O. Scholder, R. Broennimann, U. Sennhauser, and G.-L. Bona, Laser direct writing of single-mode polysiloxane optical waveguides and devices, *J. Lightwave Technol.* **32**, 3036–3042 (2014).
- [96] S. Passinger, A. Seidel, C. Ohrt, C. Reinhardt, A. Stepanov, R. Kiyon, and B. N. Chichkov, Novel efficient design of y-splitter for surface plasmon polariton applications, *Opt. Express* **16**, 14369–14379 (2008).
- [97] M.-C. Oh, W.-S. Chu, J.-S. Shin, J.-W. K., K.-J. Kim, J.-K. Seo, H.-K. Lee, Y.-O. Noh, and H.-J. Lee, Polymeric optical waveguide devices exploiting special properties of polymer materials, *Optics Comm.* **362**, 3 – 12 (2016). *Polymer Photonics and Its Applications*.
- [98] G. Jiang, S. Baig, and M. R. Wang, Flexible polymer waveguides with integrated mirrors fabricated by soft lithography for optical interconnection, *J. Lightwave Technol.* **31**, 1835–1841 (2013).
- [99] F. Wang, F. L., and A. Adibi, 45 degree polymer micromirror integration for board-level three-dimensional optical interconnects, *Opt. Express* **17**, 10514–10521 (2009).
- [100] X. Lin, A. Hosseini, X. Dou, H. Subbaraman, and R. T. Chen, Low-cost board-to-board optical interconnects using molded polymer waveguide with 45 degree mirrors and inkjet-printed micro-lenses as proximity vertical coupler, *Opt. Express* **21**, 60–69 (2013).

- [101] Y. Liu and K. S. Chiang, Broad-band optical coupler based on evanescent-field coupling between three parallel long-period fiber gratings, *IEEE Photon. Technol. Lett.* **18**, 229–231 (2006).
- [102] A. Prabhakar and S. Mukherji, Microfabricated polymer chip with integrated u-bend waveguides for evanescent field absorption based detection, *Lab Chip* **10**, 748–754 (2010).
- [103] R. Waldhäusl, B. Schnabel, P. Dannberg, E.-B. Kley, A. Bräuer, and W. Karthe, Efficient coupling into polymer waveguides by gratings, *Appl. Opt.* **36**, 9383–9390 (1997).
- [104] F. V. Laere, G. Roelkens, J. Schrauwen, D. Taillaert, P. Dumon, W. Bogaerts, D. V. Thourhout, and R. Baets, Compact grating couplers between optical fibers and silicon-on-insulator photonic wire waveguides with 69% coupling efficiency, in *Optical Fiber Communication Conference and Exposition and The National Fiber Optic Engineers Conference*, (Optical Society of America, 2006), p. PDP15.
- [105] M. J. Wale and C. Edge, Self-aligned flip-chip assembly of protonic devices with electrical and optical connections, *IEEE Transactions on Components, Hybrids, and Manufacturing Technology* **13**, 780–786 (1990).
- [106] I. Papakonstantinou, D. R. Selviah, R. C. A. Pitwon, and D. Milward, Low-cost, precision, self-alignment technique for coupling laser and photodiode arrays to polymer waveguide arrays on multilayer pcbs, *IEEE Trans. Adv. Packag.* **31**, 502–511 (2008).
- [107] N. Lindenmann, G. Balthasar, D. Hillerkuss, R. Schmogrow, M. Jordan, J. Leuthold, W. Freude, and C. Koos, Photonic wire bonding: a novel concept for chip-scale interconnects, *Opt. Express* **20**, 17667–17677 (2012).
- [108] N. Lindenmann, G. Balthasar, M. Jordan, D. Hillerkuss, R. Schmogrow, W. Freude, J. Leuthold, and C. Koos, Low loss photonic wire bond interconnects enabling 5 tbit/s data transmission, in *Optical Fiber Communication Conference*, (Optical Society of America, 2012), p. OW4I.4.
- [109] T. Yamashita, M. Kagami, and H. Ito, Waveguide shape control and loss properties of light-induced self-written (lisw) optical waveguides, *J. Lightwave Technol.* **20**, 1556–1562 (2002).
- [110] S. Döring, T. Otto, M. Cehovski, O. Charfi, R. Caspary, W. Kowalsky, and T. Rabe, Highly sensitive wide range organic photodiode based on zinc phthalocyanine:c60, *physica status solidi (a)* **213**, 2387–2391 (2016).
- [111] K. Saxena, V. Jain, and D. S. Mehta, A review on the light extraction techniques in organic electroluminescent devices, *Opt. Mater.* **32**, 221 – 233 (2009).
- [112] K. Peters, Polymer optical fiber sensors—a review, *Smart Mater. Struct.* **20**, 013002 (2011).
- [113] C. Pang, C. Lee, and K.-Y. Suh, Recent advances in flexible sensors for wearable and implantable devices, *J. Appl. Polym. Sci.* **130**, 1429–1441 (2013).
- [114] F. Gu, H. Yu, W. Fang, and L. Tong, Nanoimprinted polymer micro/nanofiber bragg gratings for high-sensitivity strain sensing, *IEEE Photon. Technol. Lett.* **25**, 22–24 (2013).
- [115] C. A. Barrios, K. B. Gylfason, B. Sánchez, A. G., H. Sohlström, M. Holgado, and R. Casquel, Slot-waveguide biochemical sensor, *Opt. Lett.* **32**, 3080–3082 (2007).
- [116] P. Roriz, O. Frazão, A. B. Lobo-Ribeiro, J. L. Santos, and J. A. Simões, Review of fiber-optic pressure sensors for biomedical and biomechanical applications, *J. Biomed. Opt.* **18**, 050903–050903 (2013).

9 List of Own Publications

Peer-reviewed Journals

- [E 1] A. Günther, S. Schneider, M. Rezem, Y. Wang, U. Gleissner, T. Hanemann, L. Overmeyer, E. Reithmeier, **M. Rahlves**, B. Roth (2017): Automated Misalignment Compensating Interconnects Based on Self-Written Waveguides, *J. Lightwave Technol.* 35(13), 2678-2684, DOI: 10.1109/JLT.2017.2692305
- [E 2] A. Varkentin, M. Mazurenka¹, E. Blumenröther, M. Meinhardt-Wollweber, **M. Rahlves**, S. M. C. Broekaert, S. Schäd-Trcka, S. Emmert, U. Morgner, B. Roth (2017): Comparative study of presurgical skin infiltration depth measurements of melanocytic lesions with OCT and high frequency ultrasound, *J. Biophotonics* 10, 854-861, DOI: 10.1002/jbio.201600139
- [E 3] M. Rezem, A. Günther, B. Roth, E. Reithmeier, **M. Rahlves** (2017): Low-Cost Fabrication of All-Polymer Components for Integrated Photonics, *J. Lightwave Technol.* 35(2), 299-307, DOI: 10.1109/JLT.2016.2639740
- [E 4] A. Varkentin, M. Otte, M. Meinhardt-Wollweber, **M. Rahlves**, M. Mazurenka, U. Morgner, B. Roth (2016): Simple model to simulate OCT-depth signal in weakly and strongly scattering homogeneous media, *J. Opt.* 18, 125302, DOI:10.1088/2040-8978/18/12/125302
- [E 5] C. Kelb, W. Pätzold, U. Morgner, **M. Rahlves**, E. Reithmeier, B. Roth (2016): Characterization of femtosecond laser written gratings in PMMA using a phase-retrieval approach. *Mat. Opt. Express* 6(10), 3202-3209, DOI: 10.1364/OME.6.003202
- [E 6] M. Akin, M. Rezem, **M. Rahlves**, K. Cromwell, B. Roth, E. Reithmeier, M. Wurz, L. Rissing, H.-J. Maier (2016): Direct hot embossing of micro-elements by means of photostructurable polyimide, *J. Micro. Nanolithogr. MEMS MOEMS* 15(3), 034506, DOI:10.1117/1.JMM.15.3.034506
- [E 7] M. Rezem, A. Günther, **M. Rahlves**, B. Roth, E. Reithmeier (2016): Fabrication and Sensing Applications of Multilayer Polymer Optical Waveguides, *Procedia Technology* 26, 517 – 523, DOI: 10.1016/j.protcy.2016.08.064
- [E 8] **M. Rahlves** (2016): Flexible and low-cost production of waveguide based integrated photonic devices, *Procedia Technology* 26, 309 – 315, DOI: 10.1016/j.protcy.2016.08.040
- [E 9] K. Bremer, F. Weigand, M. Kuhne, M. Wollweber, R. Helbig, **M. Rahlves**, B. Roth (2016): Fibre optic sensors for the structural health monitoring of building structures, *Procedia Technology* 26, 524 – 529, DOI: 10.1016/j.protcy.2016.08.065
- [E 10] C. Kelb, R. Rother, A.-K. Schuler, M. Hinkelmann, **M. Rahlves**, O. Prucker, C. Mueller, J. Rühle, E. Reithmeier, and B. Roth (2016): Manufacturing of embedded multimode waveguides by reactive lamination of cyclic olefin polymer and polymethylmethacrylate, *Opt. Eng.* 55(3), 037103 (2016), DOI: 10.1117/1.OE.55.3.037103

- [E 11] **M. Rahlves**, C. Kelb, E. Reithmeier, B. Roth (2016): Methodology for the design, production, and test of plastic optical displacement sensors, *Adv. Opt. Techno.* 5(4), 325–334, DOI: 10.1515/aot-2016-0027
- [E 12] S. Schlangen, M. Ihme, **M. Rahlves**, and B. Roth (2016): Autofocusing system for spatial light modulator-based maskless lithography, *Applied Optics* 55(8), 1863-1870 (2016), DOI: 10.1364/AO.55.001863
- [E 13] U. Gleißner, B. Khatri, C. Megnin, S. Sherman, Y. Xiao, M. Hofmann, A. Günther, **M. Rahlves**, B. Roth, H. Zappe, T. Hanemann (2016): Optically and rheologically tailored polymers for applications in integrated optics, *Sensors and Actuators A: Physical* 241, 224–230, DOI: doi:10.1016/j.sna.2016.02.029
- [E 14] C. Kelb, **M. Rahlves**, E. Reithmeier, B. Roth (2015): Realization and performance of an all-polymer optical planar deformation sensor. *IEEE Sensors Journal* 15(12), 7029 - 7035 DOI: 10.1109/JSEN.2015.2472301
- [E 15] A. Günther, A. B. Petermann, U. Gleissner, T. Hanemann, E., Reithmeier, **M. Rahlves**, M. Meinhardt-Wollweber, U. Morgner, B. Roth (2015): Cladded self-written multimode step-index waveguides using a one-polymer approach, *Opt. Lett.* 40(8), 1830-1833, DOI: 10.1364/OL.40.001830
- [E 16] J. Díaz Díaz, J. Stritzel, **M. Rahlves**, O. Majdani, E. Reithmeier, T. Ortmaier, B. Roth (2015): One step geometrical calibration method for optical coherence tomography, *J. Opt.* 18, 015301, DOI: 10.1088/2040-8978/18/1/015301
- [E 17] J. Stritzel, **M. Rahlves**, B. Roth (2015): Refractive-index measurements and inverse correction using OCT, *Opt. Lett.* 40(23), 5558-5561, DOI: 10.1364/OL.40.005558
- [E 18] **M. Rahlves**, B. Roth, E. Reithmeier (2015): Systematic errors on curved microstructures caused by aberrations in confocal surface metrology, *Opt. Express* 23(8), 9640-9648, DOI: 10.1364/OE.23.009640
- [E 19] **M. Rahlves**, C. Kelb, M. Rezem, S. Schlangen, K. Boroz, D. Gödeke, M. Ihme, B. Roth (2015): Digital mirror devices and liquid crystal displays in maskless lithography for fabrication of polymer-based holographic structures, *J. Micro. Nanolithogr. MEMS MOEMS* 14 (4), 041302-1-8 DOI: 10.1117/1.JMM.14.4.041302
- [E 20] **M. Rahlves**, M. Rezem, K. Boroz, S. Schlangen, E. Reithmeier, B. Roth (2015): A flexible, fast, and low-cost production process for polymer based diffractive optics, *Opt. Express* 23(3), 3618-3622, DOI: 10.1364/OE.23.003614
- [E 21] M. Rezem, A. Günther, **M. Rahlves**, B. Roth, E. Reithmeier (2014): Hot embossing of polymer optical waveguides for sensing applications, *Procedia Technology* 15, 514-520, DOI: 10.1016/j.protcy.2014.09.011
- [E 22] K. Haskamp, **M. Rahlves**, M. Kästner, E. Reithmeier (2012): Numerical Simulation of a Shadow Projection System by Interpolating Diffraction Images, *TM Technisches Messen* 79, 60 – 68, DOI: 10.1524/teme.2012.0166

Conference Proceedings

- [E 23] **M. Rahlves** (2016): Fabrication of polymer based integrated photonic devices by maskless lithography, *Proc. SPIE 9745 (Photonics West 2016, OPTO, San Francisco, USA): Organic Photonic Materials and Devices XVIII, 97450D (24 February 2016)*, DOI: 10.1117/12.2213211
- [E 24] **M. Rahlves**, A. Varkentin, J. Stritzel, E. Blumenröther, M. Mazurenka, M. Wollweber, B. Roth (2016): Towards multimodal detection of melanoma thickness based on optical coherence tomography and optoacoustics, *Proc. SPIE 9701 (Photonics West 2016, BIOS, San Francisco, USA), Multimodal Biomedical Imaging XI, 97010F (7 March 2016)*, DOI: 10.1117/12.2213132
- [E 25] M. Rezem, C. Kelb, A. Günther, **M. Rahlves**, E. Reithmeier, and B. Roth (2016): Low-cost fabrication of optical waveguides, interconnects and sensing structures on all-polymer based thin foils, *Proceedings SPIE 9751 (Photonics West 2016, OPTO, San Francisco, USA): Smart Photonic and Optoelectronic Integrated Circuits XVIII, 975112 (3 March, 2016)*, DOI: 10.1117/12.2213182
- [E 26] M. Rezem, A. Günther, **M. Rahlves**, B. Roth, and E. Reithmeier (2016): Low-cost fabrication of all-polymer planar optical waveguides, *International Conference on Applied Optics and Photonics 2016 (German Society of Applied Optics DGAO and International Commission for Optics ICO) and 117th Annual Meeting of the German Society of Applied Optics DGAO, Hannover, Germany*
- [E 27] A. Günther, M. Rezem, **M. Rahlves**, E. Reithmeier, B. Roth (2016): Optical Coupling Structures for Integrated Polymer Photonics, *International Conference on Applied Optics and Photonics 2016 (German Society of Applied Optics DGAO and International Commission for Optics ICO) and 117th Annual Meeting of the German Society of Applied Optics DGAO, Hannover, Germany*
- [E 28] O. Melchert, E. Blumenroether, **M. Rahlves**, M. Wollweber, B. Roth (2016): Detection and simulation of optoacoustic signals generated in layered tissues, *International Conference on Applied Optics and Photonics 2016 (German Society of Applied Optics DGAO and International Commission for Optics ICO) and 117th Annual Meeting of the German Society of Applied Optics DGAO, Hannover, Germany*
- [E 29] J. Stritzel, J. Díaz Díaz, **M. Rahlves**, O. Majdani, T. Ortmaier, E. Reithmeier, B. Roth (2015): Korrektur geometrischer Verzeichnungen zur Kalibrierung von optischen Kohärenztomographiesystemen, *Springer-Verlag, Bildverarbeitung für die Medizin 2015: S. 233-238*
- [E 30] **M. Rahlves**, M. Rezem, C. Kelb, K. Boroz, D. Gödeke, S. Schlangen, E. Reithmeier, B. Roth (2015): Lab-level and low-cost fabrication technique for polymer based micro-optical elements and holographic structures, *Proc. SPIE Vol. 9508 (Holography: Advances and Modern Trends IV)*
- [E 31] M. Rezem, A. Günther, A. B. Petermann, C. Kelb, **M. Rahlves**, M. Wollweber, B. Roth (2015): Production and characterization of all-polymer based optical waveguides and interconnects, *Proceedings of the DGAO, 116th Annual Meeting of the DGAO, 26-29 May, Brno, Czech Republic*

- [E 32] M. Mazurenka, A. Varkentin, E. Blumenroether, J. Stritzel, M. Otte, **M. Rahlves**, M. Meinhardt-Wollweber, B. Roth (2015): Towards all-optical melanoma depth determination, The European Conference on Lasers and Electro-Optics (CLEO Munich), Paper# CL_3_1
- [E 33] A. Günther, A. B. Petermann, M. Rezem, **M. Rahlves**, M. Wollweber, B. Roth (2015): Production processes and characterization of all-polymer based optical waveguides and interconnects, The European Conference on Lasers and Electro-Optics (Cleo Munich), Paper# CE_8_3
- [E 34] B.-A. Behrens, R. Krimm, J. Jocker, E. Reithmeier, B. Roth, M. Rahlves (2013): Method to Emboss Holograms into the Surface of Sheet Metals, Key Engineering Materials, Vol. 549, Sheet Metal 2013, pp. 125-132, DOI: 10.4028/www.scientific.net/KEM.549.125
- [E 35] M. Akin, M. Rezem, **M. Rahlves**, B. Roth, E. Reithmeier, and L. Rissing (2014): Direct hot embossing of micro-elements by means of UV-structurable polyimide, 40th International Conference on Micro and Nano Engineering MNE 2014, Lausanne, Switzerland, DOI: 10.13140/2.1.1919.1367
- [E 36] J. Díaz Díaz, M. Rahlves, O. Majdani, E. Reithmeier, T. Ortmaier (2013): A one step vs. a multi step geometric calibration of an optical coherence tomography, Proceedings of the Society of Photo-Optical Instrumentation Engineers Photonics West 2013 (SPIE Photonics West 2013)
- [E 37] M. Rahlves, J. Díaz Díaz, J. Thommes, O. Majdani, B. Roth, T. Ortmaier, E. Reithmeier (2013): Towards refractive index corrected optical coherence tomography as a navigation tool for bone surgery, The European Conference on Lasers and Electro-Optics (Cleo Munich), Paper# CL_P_2
- [E 38] B.-A. Behrens, J. Jocker, E. Reithmeier, A. Leis, **M. Rahlves** (2012): Werkzeuge zum direkten Prägen von Hologrammen in Blechwerkstoffe – holografische Elemente als Sicherheitsmerkmal und Designelemente, Tagungsband zum 32. EFB-Kolloquium Blechverarbeitung am 14.-15.02.2012 in Bad Boll, S.77-96
- [E 39] J. Díaz Díaz, M. Rahlves, O. Majdani, E. Reithmeier, T. Ortmaier (2012): Towards a one step geometric calibration of an optical coherence tomography, Proceedings of the Society of Photo-Optical Instrumentation Engineers/Chinese Optical Society Photonics Asia 2012 (SPIE/COS Photonics Asia 2012)
- [E 40] J. Díaz Díaz, M. Rahlves, T.S. Rau, O. Majdani, E. Reithmeier, T. Ortmaier (2012): Suitability of Optical Coherence Tomography for an Intra-Operative Navigation System by Estimation of the Fiducial Localization Error, Proceedings of the 26th International Congress on Computer Assisted Radiology and Surgery (CARS 2012)
- [E 41] S. Mirzaei, **M. Rahlves**, F. Fahlbusch, E. Reithmeier, E. (2009): Application of an Optomechanical Image Derotator for Measuring Vibration and Deformation of Rotating Objects, Proceedings Optimes
- [E 42] **M. Rahlves**, S. Mirzaei, T. Fahlbusch, E. Reithmeier (2009): In-plane and out-of-plane deformation and vibration measurement using an optomechanical image derotator, Proc. SPIE 'Optical Inspection and Metrology for Non-Optics Industries' (Optics and Photonics) 7432

- [E 43] T. Dziomba, M. Shaleev, **M. Rahlves**, J. Seewig, R. Krüger-Sehm (2008): Self-assembled Ge/Si islands as novel nano-roughness standards for SFM, Proceeding of the XII International Colloquium on Surfaces
- [E 44] **M. Rahlves**, M. Seifert, T. Fahlbusch, J. Frühauf, E. Reithmeier (2007): Bewertung von Weißlichtinterferometermessungen mit einer Kantenteststruktur, 108th Proceedings of the annual meeting of the German Society of Applied Optics (DGaO)
- [E 45] G. Bartl, G. Gülker, K. D. Hinsch, **M. Rahlves** (2006): Performance criteria in low coherence speckle interferometry (LCSI), Proceedings SPIE 'Speckles, from Grains to Flowers' (Speckle 06) 6341
- [E 46] **M. Rahlves**, A. Gräper, A. Kraft, E. Reithmeier (2006): Entwicklung multifunktionaler Kalibriernormale für bildverarbeitende 3D-Mikroskope, 107th Proceedings of the annual meeting of the German Society of Applied Optics (DGaO)

Books

- [E 47] B.-A. Behrens, J. Jocker, E. Reithmeier, **M. Rahlves** (2012): Werkzeuge zum direkten Prägen von Hologrammen in Blechwerkstoffe, EFB-Forschungsbericht Nr. 346 ISBN: 978-3-86776-384-4
- [E 48] **M. Rahlves** (2011): Calibration of confocal microscopes, PhD thesis, Leibniz University, Hannover, PZH-Verlag, ISBN: 978-3-943-10424-0
- [E 49] **M. Rahlves**, J. Seewig (Eds., 2009): Optisches Messen technischer Oberflächen in der Praxis, Beuth Verlag, ISBN: 978-3-410-17133-1
- [E 50] B.-A. Behrens, B. Roth, J. Jocker, L. Altan, **M. Rahlves** (2016): Verfahren zum Prägen von Hologrammen auf Blechteile mit gekrümmter Oberfläche. EFB-Forschungsbericht, ISBN: 978-3-86776-493-3

Hannoversches Zentrum für optische Technologien



Optical Technologies.